A transistor based sensing platform and a microfluidic chip for a scaled-up simulation of controlled drug release

Politecnico di Torino

Doctoral Thesis

A transistor based sensing platform and a microfluidic chip for a scaled-up simulation of controlled drug release

Author:
Alessio Verna

Supervisor:
Prof. Fabrizio Pirri
Co-Supervisor:
Prof. Matteo Cocuzza

A thesis submitted for the degree of
Doctor of Philosophy in Physics

XXVII cycle: 2012-2014
Scientific Disciplinary Sector: FIS/03

"Though I am always in a haste, I am never in a hurry, because I never undertake more work than I can go through with perfect calmness of spirit."

John Wesley the Methodist, The Methodist Book Concern

"I always knew I was a star. And now the rest of the world seems to agree with me."

Farrokh Bulsara (Freddie Mercury)

POLITECNICO DI TORINO

Abstract

Department of Applied Science and Technology

Doctor of Philosophy in Physics

A transistor based sensing platform and a microfluidic chip for a scaled-up simulation of controlled drug release

by Alessio Verna

The framework of my thesis are Biomedical (or Biological) Microelectromechanical Systems (BioMEMSs). Two fields in which this discipline is involved are sensors and fluidics. Functionalized organic materials are under investigation to be the means for target biological sensing, and sensors are evolving to be integrated in fluidics platforms in order to produce in the future new small portable diagnostic devices. On the other hand one of the challenges of micro and nanofluidic technology is the fabrication of drug release devices, in order to control the amount of drug present in an organism. In this thesis these two arguments are considered. First we will discuss the implementation of a process oriented to the fabrication of an hybrid Organic Field Effect Transistor (OFET) with sensing capabilities from the semiconductive layer. In the second part we will show the fabrication process of a silicon based structure for the scaled-up characterization of drugs in nanochannels for controlled drug release. The characterization will consider charged microspheres playing the role of drugs to be tracked with a microscope. We will highlight also the possibility of implementing the transistor related technology in nanofluidic systems for the electronic controlled drug release.

Acknowledgements

This thesis work is the result of three years of 'hard work' in three structures: χ-Lab and Techfab at Chivasso - Italy and the Italian Institute of Techology (IIT) at Torino - Italy.

My work has been oriented to *fabrication processes* which means to master both of the processes and the technical equipment needed for the processes. For this reason in this thesis a big amount of fabrication details relating technological processes are present.

My work is structured as follows: first I will describe the technologies (the hardware) and the processed to which I will refer to in the following chapters. The skilled reader can skip this part. The main part of the thesis covers two subjects: the fabrication and characterization of a transistor device and a drug delivery simulation platform. Finally in the appendices some theory will be provided for both devices in order to better understand the results.

People who had a key role in developing this work are: Denis Perrone, Simone Marasso, Alessio Tommasi, Domenico Mombello, Chiara Ottone and Stefano Gentili at $\chi-$Lab.
Giancarlo Canavese, Alessandro Chiolerio, Valentina Cauda, Sergio Bocchini, Marco Laurenti, Marco Didonato, Marco Fontana, Ignazio Roppolo and Marzia Quaglio at IIT.
Laura Boschis, Niccoló Ciprianetti, Elena Gulí, and Cosimo Spagnolo at Techfab.
Alessandro Nesca and Giuseppe Mina at Microla.
Andrea Richaud for his summer internship activity at IIT.
I also thank my supervisors: Matteo Cocuzza and Fabrizio Pirri.

Contents

List of Figures

Abbreviations

BOE	**B**uffered **O**xide **E**tchant
DI (water)	**D**e-**I**onized (water)
DRIE	**D**eep **R**eactive **I**on **E**tching
FET	**F**ield **E**ffect **T**ransistor
OEP	**O**cta **E**thyl **P**orphyrin
OFET	**O**rganic **F**ield **E**ffect **T**ransistor
OTFT	**O**rganic **T**hin **F**ilm **T**ransistor
RTA	**R**apid **T**hermal **A**nnealing
RTP	**R**apid **T**hermal **P**rocess
TFT	**T**hin **F**ilm **T**ransistor
TGA	**T**hermal **G**ravimetric **A**nalysis
TPP	**T**etra**p**henyl**p**orphyrin
SEM	**S**canning **E**lectron **M**icroscope
XPS	**X**-Ray **P**hotoelectron **S**pectroscopy
XRD	**X**-**R**ay **D**iffraction

Dedicated to Hussein Jafer

Chapter 1

Overview on MEMS fabrication technologies

We will describe in this chapter the micromachining techniques we mostly used in this thesis work for the devices fabrication shown in the next chapters. Since not all the MEMS related techniques are discussed here, the interested reader can refer to [1] for a complete description.

1.1 Cleanroom environment

The fabrication of devices with features of the micrometric scale needs a laboratory with a controlled environment. Just some dust can be at same size of the device. In fact, for manufacture of structures in micro- or even sub-micrometer regions the surroundings of the manufacturing area must be scrupulously controlled. This includes the room temperature, the air humidity and above all the particle density in the air and in the media being used. If one contaminant particle of 0.5 μm settles on a critical part of an integrated circuit, it can already cause considerable damage if not lead to failure of the circuit. Semiconductor technology, as well as microstructure technology and clean room techniques are therefore concepts that are inseparable with each other.

Figure 1.1 shows the general concept of a clean room. An atmosphere with a low number of particles is of utmost importance and hence there is a constant exchange of "contaminated" air with recovered air free of particles. High quality clean rooms are operated in laminar flow. Air turbulence increases the retention period of particles in the laboratory surroundings. The actual clean room is a shell-type construction surrounded by a second enclosure, the "grey room", in which the airflow is freshly

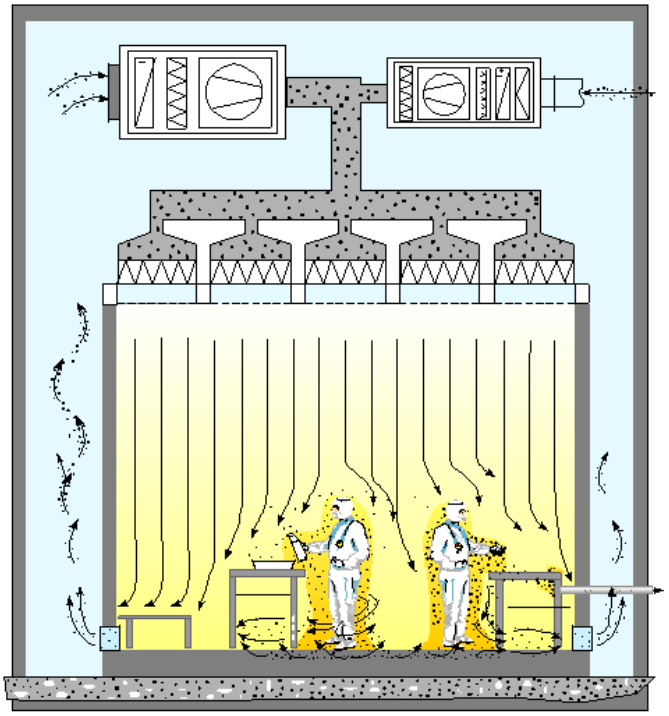

FIGURE 1.1: Air Flow principle for unidirectional (laminar) flow Cleanrooms

prepared with respect to temperature and air humidity. Once addicted, the fresh air it is pushed through the filter ceiling into the clean room. The air which flows laminarly at right angles to floor of the clean room is forced through a perforated flooring and transported through air channels again to the processing room above the filter cover. The air effluents of certain chemical processes are drawn directly from the process stage and separately disposed of. The circulating air is mixed with fresh air, humidified, temperature controlled and fed back into the pressurized room above the filter ceiling. Depending on the pore size of the filter, the air turnover and other parameters of the manufacturing environment, an atmosphere is obtained which is categorized into quality classes based on the amount of suspended particles. The class of the cleanrooms used for this thesis work are *class 100* and *class 1000*. The numbers denote, refer to FED-STD-209E, the particles of size 0.5 μm or larger permitted per cubic foot of air.

1.2 Thin film deposition techniques

Thin films are the essential basis for the fabrication of integrated circuits as well as microsystems components in both the mass fabrication of products or in single samples for research applications. Thin films are either the carrier of the desired functions (sensors, actuators, electrical parameters), or serve an auxiliary purpose (e. g. isolation and protection layers, removable sacrificial layers). Depending on the area of application

the thickness of these films ranges from a few nanometers to some micrometers. The requirements which are placed on the films vary considerably, however the quality of films with respect to purity, absence of foreign matters, homogeneity of the internal structure, and adhesion to the substrate are always desirable properties.

1.2.1 Thermal evaporation

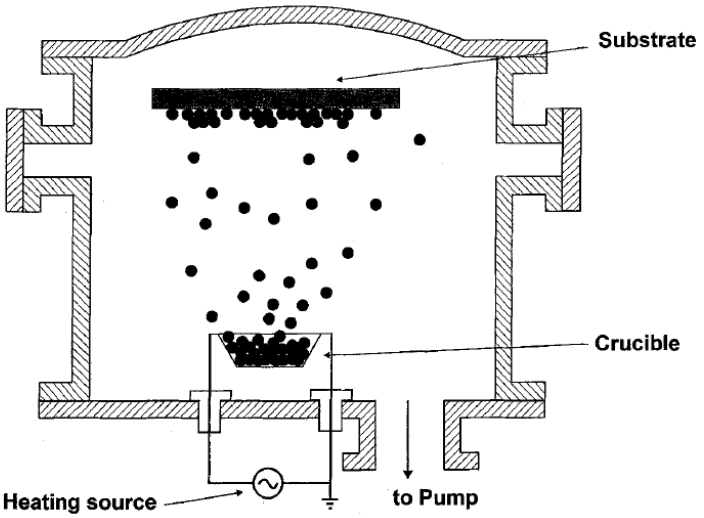

FIGURE 1.2: The evaporation process. The crucible is heated, and the atoms move without collision (for the high vacuum condition) to the substrate and condense forming a film. The average energy of the atoms is in the order of 0.2 eV.

In evaporation, the material, which is to be deposited onto a substrate, is heated in a crucible above melting temperature (Fig. 1.2). Due to the thermal energy and the low binding force in a liquid some of the atoms can leave the melt by evaporation and travel to the substrate, where they condense and form a film. Unwanted deposits on the substrate surface can be removed by heating (desorption of the adatoms) prior to deposition. This process takes place in a vacuum chamber under a vacuum of 10^{-4} to 10^{-7} mbar. In this range the mean free path of the particles exceeds that of the inside dimensions of the chamber and the probability of unwanted collisions with other gas particles decreases to almost zero.

The choice of the evaporation source is influenced by the kind of material to be evaporated.

For metal (and some metal oxides) thin film deposition the **electron beam** vaporization (e-beam) is the most frequently used. An electron beam is directed to the crucible material and vaporizes it. In order to protect the hot cathode from bombardment by ionized source atoms, the cathode is placed sideways of or underneath the source, and the electron beam is bend and guided into the crucible by a permanent magnetic field.

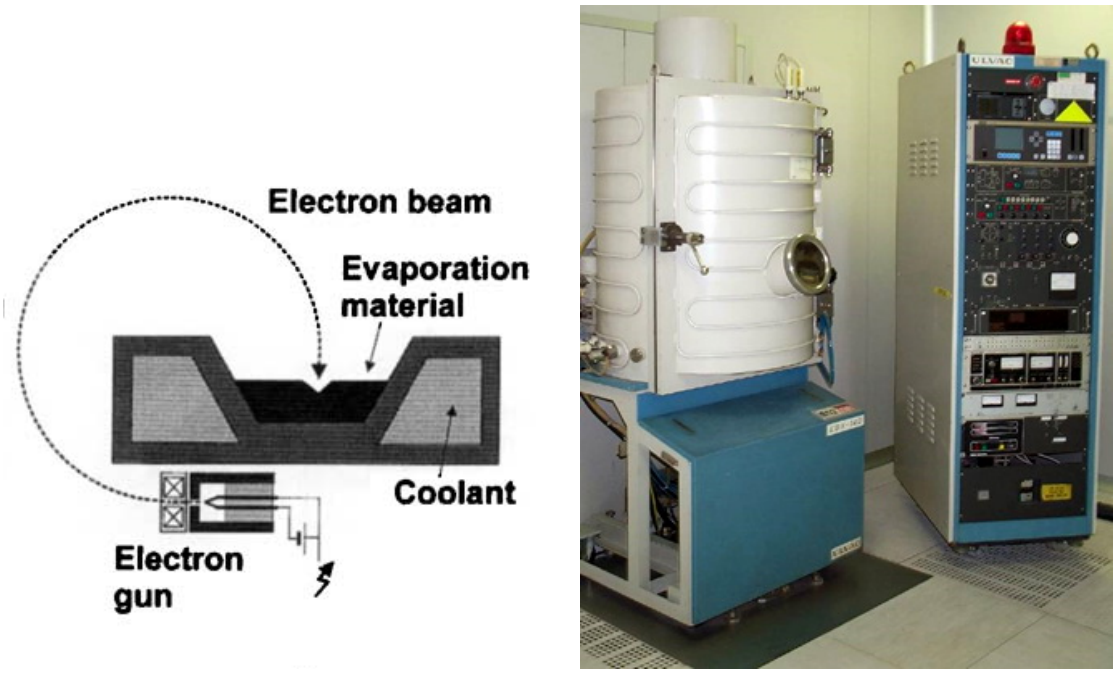

(A) E-beam source scheme (B) Ulvac EBX 14D evaporation system

FIGURE 1.3: Electron beam evaporation. Electron gun scheme and evaporator chamber.

For organic thin films, or more generally for materials in which a well-defined kinetic energy is needed, a effusion cell or **Knudsen cell** (Fig. 1.4) evaporation source is requested. Typical process in which these cells are used is for organic molecules evaporation, since they allow to evaporate at a very precise temperature.
A Knudsen cell is a heated cavity with an orifice that is small enough so as not to disturb the equilibrium vapor pressure inside the cavity. The effusion rate from the orifice is only dependent on the vapor pressure of the evaporant and not on its amount. If the evaporation takes place in a vacuum chamber the mean free path becomes very large compared with the dimensions of the chamber [2].
The crucible is typically made from quartz or pyrolytic boron nitride and has thermocouples mounted on the backside to measure temperature. The heat is supplied to the crucible by resistively heated wire. Obviously the thermal mass of Knudsen cells is large, so rapid changes in temperature (and hence in the deposition rate) are not possible.

Small-molecule and oligomer organic semiconductors are typically deposited by vacuum evaporation. This technique is usually not applicable for polymers, because polymers tend to decompose by cracking at high temperatures. The main advantages of vacuum evaporation are the easy control of the thickness, the purity of the deposited film and the ability to realize highly ordered films by monitoring the deposition rate and the

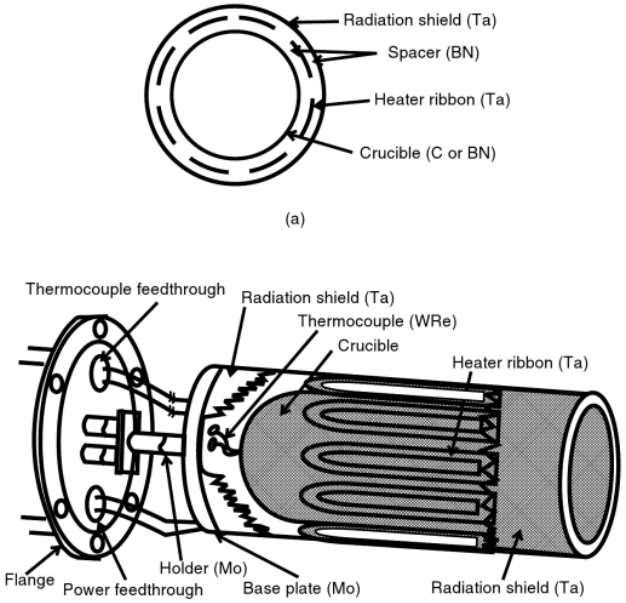

FIGURE 1.4: Knudsen cell

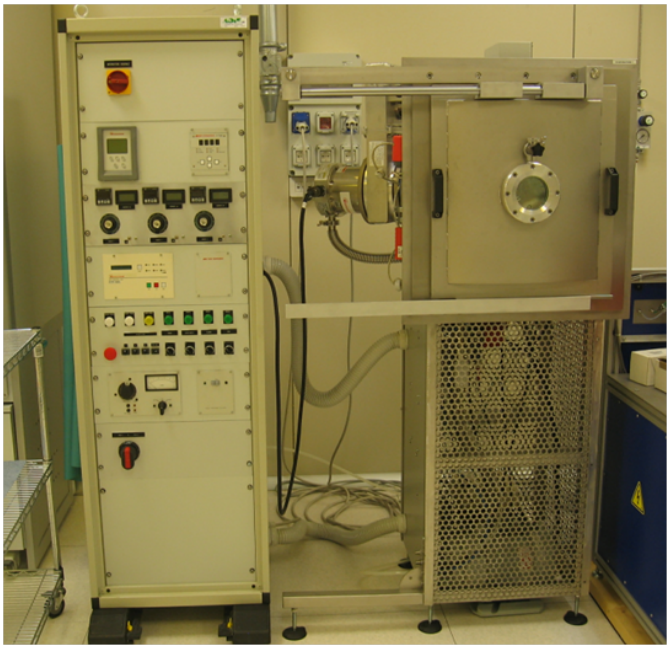

FIGURE 1.5: Edwards thermal evaporation system

substrate temperature [3, 4]. Patterned films can be realized by evaporation through photolithography or using a shadow mask.

1.2.2 Sputtering

A target (the source) and a substrate are placed opposite to each other in a chamber, which is filled with Argon gas at 10^{-3} - 10^{-4} mbar. The target and substrate are separated at a distance of a few centimeters (Fig. 1.6). When an electric field is applied between the target and substrate electrode, then the ever present few charged particles in the neutral gas are accelerated towards the cathode and anode respectively. The charged particles are due to cosmic radiation and natural radioactivity of the surrounding material. The accelerated electrons, when hitting neutral Ar atoms on their way to the anode, can generate new ions and electrons. These electrons in turn can again generate new pairs of ions and electrons and so on. The ions on the other hand will generate secondary electrons when hitting the cathode. This avalanche of electrons maintains a **plasma**. Collision of electrons with neutral particles can cause one of the three effects: ionization, dissociation, excitation. Dissociation is used in certain processes to generate radicals, which are neutral particles with free bonds. These radicals are chemically very reactive and are utilized for composite layers and for etching. Atoms which arc being hit by electrons may get into an excited state. The absorbed energy is released again by emitting a photon. De-excitation and production of photons of characteristic wavelength is the reason for the glow of a particular color of the plasma.
In self-maintained discharges the ions arc generated by accelerated electrons within the electric field are due to the secondary electron emission at the cathode. The discharges are dependent on the electric field and the gas pressure.

Even if the evaporation is a well controlled process and is used to produce very pure films, it has the disadvantage of a relatively low adhesion due to the low energy of the condensing atoms. Sputtering gives better results for applications which require a **strong adhesion to the substrate**. The argon ions which are generated in the discharge are accelerated onto the target and because of their high kinetic energy kick out neutral atoms and molecular fragments from the target surface, which fly towards the substrate at high velocity and hit the surface. In contrast to thermal processes, the sputtered atoms have 10-100 times the amount of kinetic energy (Fig. 1.6). The adhesion of the film which forms on the substrate is hence high in comparison to evaporated films. Another advantage of the sputtering process is the fact that the target material does not have to be heated. Consequently, refractory materials such as tantalum or tungsten or ceramics, can also be sputtered.

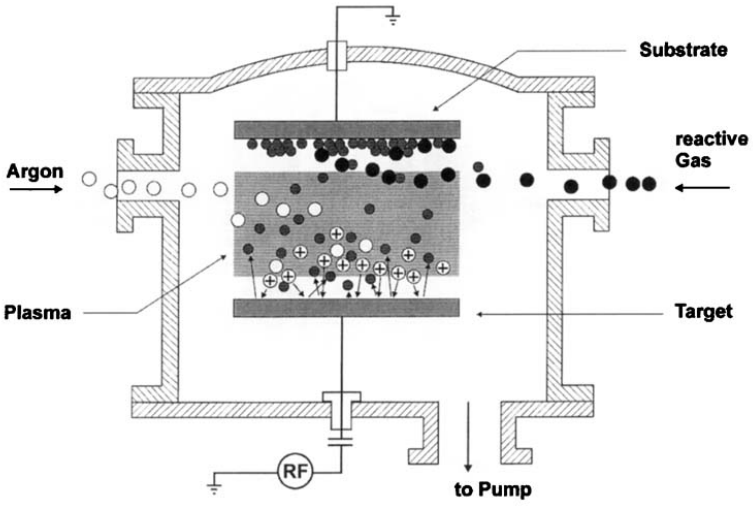

FIGURE 1.6: The sputtering process. Neutral noble gas atoms (usually Argon) are ionized by collision with energetic electrons in the plasma. These ions are accelerated toward the target. By impact with the target neutral atoms are released from the surface. These neutral atoms condense on the substrate forming a film. The average energy of the atoms approaching the substrate is in the order of 10 to 100 eV. By adding a reactive gas to the chamber compound films such as Al_2O_3, or TiN can be fabricated.

FIGURE 1.7: Kurt J. Lesker PVD75 - RF Magnetron Sputtering.

1.2.3 Solution-Processed Deposition

Various techniques are available for processing soluble polymer semiconductor films from the liquid phase; these include **spin-coating, casting, printing, and soluble precursor conversion**. One of the most simple and effective ways to realize a nice polymer

film is by spin-coating. When the technique is well handled, it allows the production of very homogeneous films with precise control of their thickness over relatively large areas. Control parameters of a spin-coating process include spin-coating speed, ramping rate, choice of solvent for the polymer solution, drying temperature, drying time, and so on; these parameters need to be optimized to achieve a film of desired thickness and uniformity. A limitation of the spin-coating technique is the lack of the possibility of patterning [4].

1.3 Optical photolithography

The wafer is first covered with a thin layer of a photosensitive polymer. This is done by **spin-coating**. For this, the wafer is first mounted onto a rotatable chuck and fixed by vacuum. Next to the center of the substrate to be coated (generally a round silicon wafer) with polymer, a drop of liquid coating is applied and the wafer is brought into rotation with a high peripheral velocity. Due to centrifugal force the coating is spread very evenly across the wafer surface, and a very homogeneous layer can be produced. By increasing the speed of rotation the layer thickness decreases. This process of spin-coating is used in the application of resist layers on the substrate for optical lithography and electron beam lithography as well, although the resist composition is different in both cases. In microelectronics, the final thickness after drying and pre-baking is only fractions of a micrometer, whereas in MEMS depending on the application, the thickness may amount of up to 100 μm.

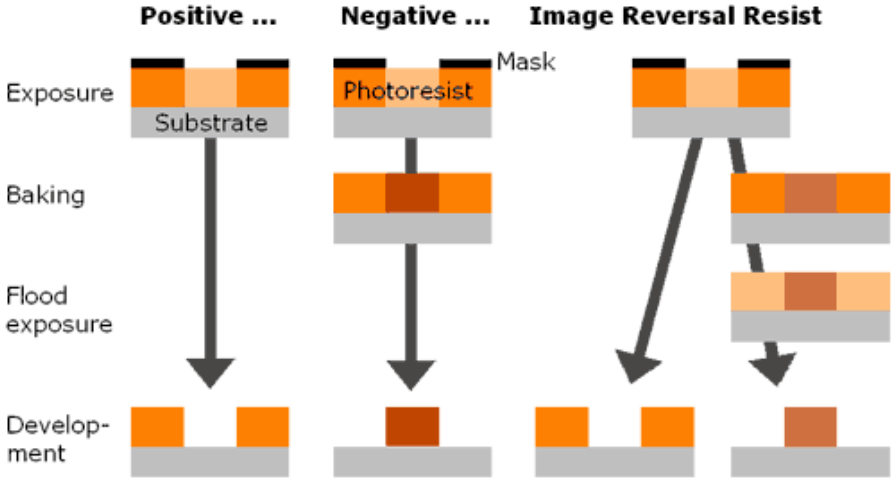

FIGURE 1.8: Scheme showing different kinds of photoresist

After the above processing the desired pattern is imaged (usually with UV light with a controlled energy) onto the resist layer. During the lithographic process the resist

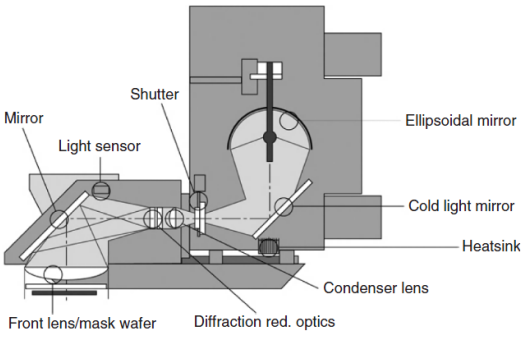

(A) Exposure/mask aligner tool: lamp–mirror–shutter–filter–lens system, and mask and wafer.

(B) Neutronix Quintel NXQ4006 double side mask aligner.

FIGURE 1.9: Mask aligner working scheme and equipment.

changes its chemical properties, so that irradiated and non-irradiated regions have different solubility in a particular solvent or developer. Which region is soluble depends on the tone of photoresist. For positive resist, in the subsequent development, the exposed areas are dissolved, whereas the non-exposed areas remain untouched. The pattern of the mask is now transferred into a chemical resistant stencil on the surface of the wafer. After the subsequent processes, such as etching, evaporation, or modification processes the resist is removed, leaving either an additive or subtractive pattern, or a pattern of a modified surface on the wafer.

As we said, depending upon whether the exposed or non-exposed region is dissolved, it is possible to differentiate between positive or negative resists. With a positive resist the polymer is changed such that the exposed regions can be dissolved, whilst the non-exposed regions remain unchanged. With a negative resist, the polymer becomes insoluble in the developer after exposition. Exposing of a positive resist, chain scission processes are induced in the long polymer chains so that the molecular weight of resists decreases greatly.

Optical lithography is most important in the production of microelectronic circuits and also in microtechnology. For many years optical lithography was considered to come to an end at pattern resolution of under 0.5 μm. Nevertheless due to intensive development this limit could be reduced to below 0.2 μm [1].
In photolithography the pattern is produced by imaging a mask into the photosensitive resist. Mercury vapor lamps are conventionally used as illumination sources, which have strong emission lines at 435 nm (G-line), 405 nm (H-line) and 365 nm (I-line).
The masks which are used in optical lithography consist of glass or quartz plates with a thickness of about 1.5 to 3 mm. A sputtered chromium layer serves as the absorber and has a thickness of usually 100 nm, which is sufficient for complete opacity.

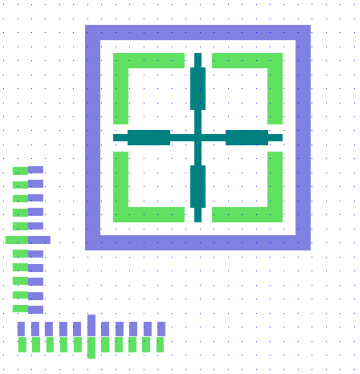

FIGURE 1.10: Lithographic markers for three steps process.Vernier pattern helps to fine adjust the alignment.

1.3.1 Markers

Sequential lithography pattern have to be precisely adjusted to each other. Often even the first lithography pattern in the process sequence has to be centered to the virgin wafer and aligned with respect to the crystallographic orientation (i.e. with respect to the flats at the wafer circumference).

Certain spaces in standardized mask design are provided for this kind of adjustment pattern. In Fig. 1.10 such an adjustment pattern is shown which facilitates the adjustment of the mask to the geometry of the wafer.

1.3.2 Double side lithography

MEMS micromachining often involves the fabrication of **structures on both sides of a wafer**. For this purpose double-sided lithography is necessary. First the front side is processed: the resist is applied on top, the wafer is aligned and exposed, developed, rinsed and dried. Then, depending on device structure, etching (or some other kind of fabrication) of the front side is done.

Back-side lithography involves the application of photoresist on the back-side, which means that the front side of the wafer is placed in vacuum contact with the spin-coater chuck and thus must be protected. Photoresist is often used but it cannot be used for patterning after being vacuum chucked.

The alignment mechanism in double-sided lithography relies on image processing. An image of the mask alignment marks is stored, and the wafer is then inserted between the mask and the alignment microscope, so the alignment marks on the wafer are aligned

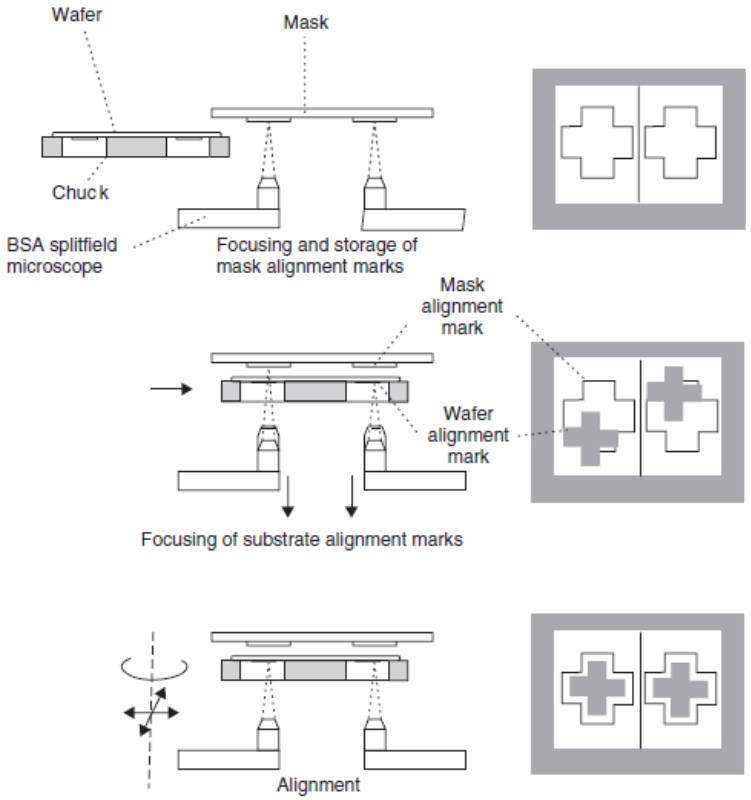

FIGURE 1.11: Double side alignment scheme: (A) the image of mask alignment mark is stored; (B) the alignment marks on the back side of the wafer are brought on focus; (C) the position of the wafer is adjusted by translation and rotation to align the marks to the stored image. From [5]

with the stored mask alignment marks (Figure 1.11). Alignment accuracy is about 1 μ m at best, and usually a few microns.

1.3.3 Computer Aided Design (CAD)

In order to produce a mask, the information has to be exposed pixel by pixel into the resist layer of the mask. This is done with a **pattern generator**, which in our case is a *laser writer* (see next section). The pattern generator requires information about which sections of the mask should be exposed. In order to generate this information, a so-called CAD-system is used, with which the design can be carried out in an interactive mode with the designer at the computer terminal. The aim of the CAD-layout is to specify light transmitting and absorbing areas of a mask.

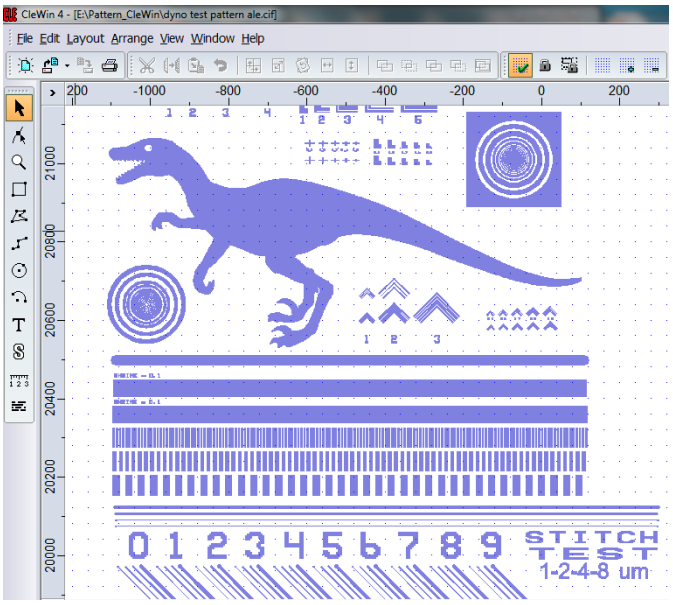

FIGURE 1.12: Example of CAD test pattern

1.4 Laser lithography

The laser lithography technique is a kind of maskless lithography. In maskless lithography the radiation that is used to expose a photosensitive emulsion (or photoresist) is not projected from, or transmitted through, a photomask; instead, most commonly, the radiation is focused to a **narrow beam**. The beam is then used to directly write the image into the photoresist.

In this class of devices a laser beam of suitable wave length (able to expose most photoresist) is focused by a microscope lens on a substrate. The substrate is mounted on a XY stage which allows precise movement of the substrate in order to achieve the best resolution during the scan process 1.13. The details of this kind of apparatus are described in [6].

The fields in which this technique is suitable are the production of lithographic masks, as we stated before, or the direct exposition of few samples in order to test a technological process without the need of mask fabrication (Figure 1.13). By direct writing on samples it is possible also to reach a higher resolution than normal photolithography (up to 0.5 μ m).

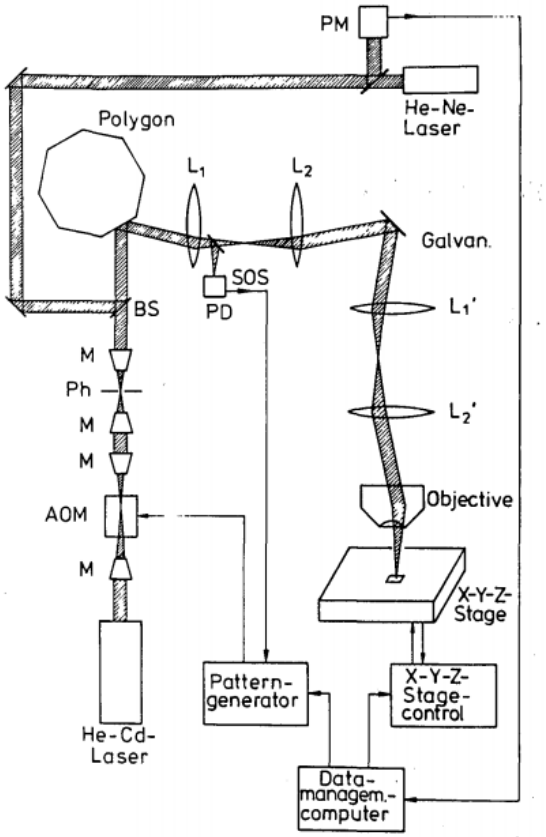

(A) Optomechanical concept of the laser-scanning system: (M) microscope objective; (AOM) acoustooptic modulator; (Ph) pinhole; (BS) beam splitter; (PD) photodetector; (PM) photomultiplier; (SOS) start-of-scan signal; (L_1, L_1', L_2,L_2') scanning optic. From [6].

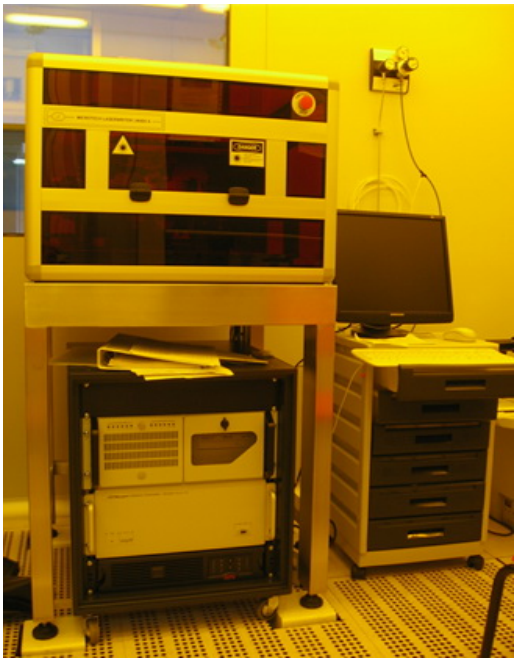

(B) Microtech Laserwriter

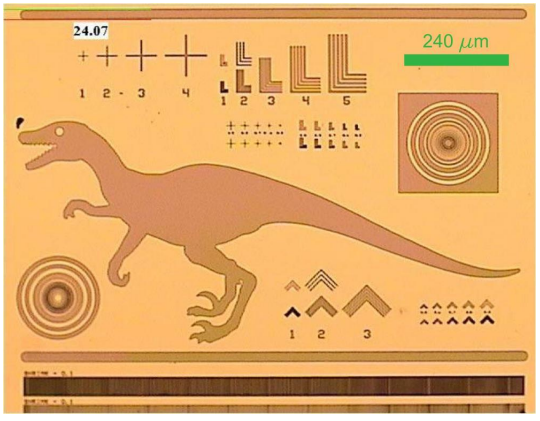

(C) Example of laser patterned photoresist: calibration of image reversal photoresist.

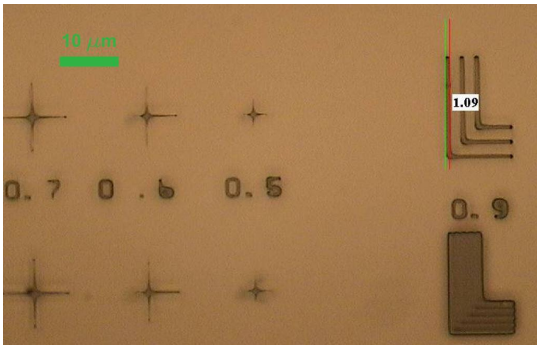

(D) Particular of (C) showing submicrometric patterns

FIGURE 1.13: Laser-scanning system working scheme, equipment and lithographed patterns.

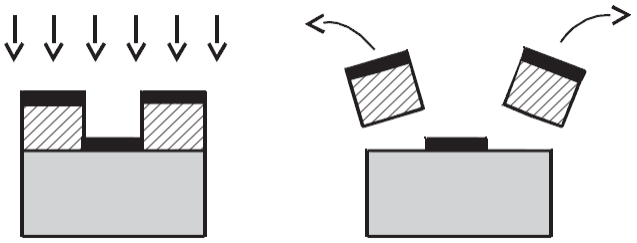

FIGURE 1.14: Lift-off process: left, metal deposition on resist pattern; right, resist dissolution and metal lift-off.

1.5 Patterning techniques

1.5.1 Etching

In this case the pattern transfer process consists of two steps: lithographic resist patterning and the subsequent etching of the underlying material. Resist protects the areas where the material needs to remain, and open areas are etched. More details on these class of processes are given in the next section.

1.5.2 Lift-off

Lift-off is metallization with sacrificial resist: after lithography, metal deposition is done on the resist pattern, followed by resist dissolution in solvent and lift-off, with all the metal that is not in contact with substrate being removed (Figure 1.14).
Solvent used include *acetone*, *dimethylsulfoxide* (DMSO) or *N-Methyl-2-pyrrolidone* (NMP). NMP is a powerful lift-off medium due to its physical properties: NMP yields a low vapor pressure, strongly solves organic impurities as well as resists, keeps solved particles in solution, and can be heated up to 80°C due to its high boiling point. DMSO can be regarded as a non toxic alternative to NMP.
Lift-off metallization should have poor step coverage, and therefore the method of choice is evaporation, even though sputtering can be used too. The deposition process has, however, photoresist-imposed limitations: it must take place under about 150°C temperature because of resist thermal stability. To avoid deposition on the sidewalls, special techniques have been devised to make lift-off easier. One way is to use negative resists or image reversal resists which typically have negative sidewall angles (Figure 1.8).

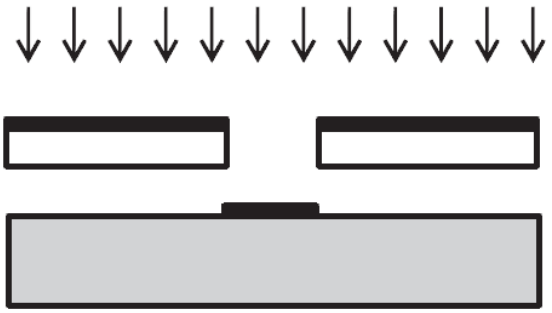

FIGURE 1.15: Deposition with a shadow mask

1.5.3 Shadow mask

Shadow masks (also known as stencil masks) are mechanical aperture plates. Shadow mask patterning is basically lift-off with a mechanical mask instead of a resist mask. The shadow mask is aligned with and temporarily attached to a substrate, and this stack is then positioned in the deposition system (Figure 1.15). Basically any deposition technique can be used, but line-of-sight methods like evaporation lead to the smallest penumbra under the mask. The smaller gap between the stencil and the wafer minimizes unwanted deposition, too.
Some materials are so sensitive that their deposition has to be the very last process step, for example (bio)chemical sensor films. The application of photoresist on these films is not possible, and solvent dissolution cannot be used, ruling out lift-off. And the shadow mask saves a lot of process steps: resist spinning, baking, exposure, development, rinsing and drying are eliminated. If the shadow mask and wafer can be aligned with each other in a mask aligner or a bond aligner, micrometer alignment accuracy is possible; often, however, shadow masks are only used for non-critical applications where manual alignment is enough.

Patterning by depositing vaporized materials through shadow masks was one of the earliest and simplest routes for making OLEDs and OTFTs. In this process, metals or low molecular weight organic molecules are evaporated from a source in a physical vapor deposition system and travel through openings in masks placed near the surface of the substrate. The deposition typically occurs under high vacuum (from 10^8 to 10^6 torr) such that the mean free path of the evaporated species exceeds the distance between the source and the substrate [7]. When this condition is satisfied, the evaporated material travels in a directional manner through the gaps in the mask and onto the substrate [8]. This technique is additive at the substrate level, which enables sequential deposition of multiple layers of different materials. The shadow mask technique is attractive for OTFT fabrication because it can guarantee a simple, robust, and low cost source/drain

contact definition process without damage to underlying organic materials if present. A shadow mask can also provide a constructive tool to deposit patterned low-molecular weight organic films, to define the active semiconductor of the OTFT [4].

1.6 Wet etching

1.6.1 Thin film wet etching

The oldest form of etching is immersion of the patterned substrate in a suitable liquid chemical that attacks the exposed region of the substrate, and leaves the protected regions alone. The rate of etching and the shape of the resulting etched feature depend on many things: the type of substrate, the specific chemistry of the etchant, the choice of masking layer (and the tightness of its adhesion to the substrate), the temperature (which controls reaction rates), and whether or not the solution is well stirred (which affects the rate of arrival of fresh reactants at the surface). Depending on the temperature and mixing conditions, the etching reaction can be either reaction-rate controlled, dominated by temperature, or mass-transfer limited, determined by the supply of reactants or the rate of removal of reaction products.

Most wet etching is isotropic, in that the rate of material removal does not depend on the orientation of the substrate. However, when etching single-crystal substrates with certain etchants, orientation-dependent etching can occur. Figure 1.16 illustrates the use of isotropic wet etching through the openings in a masking layer to pattern a thin film on a substrate. Note the undercut of the mask feature. This is because of the isotropic etch behavior; if there is a sufficient supply of reactants, lateral etching occurs at about the same rate as vertical etching. Adhesion of the mask to the thin film is also important. If this adhesion is weak, enhanced etching can actually occur at the film-mask interface, exaggerating the sloping of the sidewall. Not shown in the figure is the fact that the sidewall, in addition to having a slope, is actually somewhat curved. Such tapered sidewalls can be an advantage when attempting to cover the etched feature with an additional film.

Table 1.1 illustrates the variety of materials that can be etched with wet etchants.

One of the most important and widely used etching process is the etching of SiO_2 with BOE 7:1. BOE stands for Bufferd Oxide Etchant, a solution composed by *Ammonium fluoride* (34,8%) and **Hydrofluoric acid** (6,5 %). The etching of SiO_2 films undergoes the following reaction [9]:

$$SiO_2 + 6HF \rightarrow H_2SiF_6 + 2H_2O$$

TABLE 1.1: Wet etchants for photoresist masked etching (mostly room temperature)

SiO_2	$NH_4F : HF$ (7:1) Called BOE, for buffered oxide etchant
Poly-Si	$HF : HNO_3 : H_2O$ (6:10:40)
Al, Cu	$H_3PO_4 : HNO_3 : H_2O$ (80:4:16) at 70°C
Mo	$H_3PO_4 : HNO_3 : H_2O$ (80:4:16)
W, TiW	$H_2O_2 : H_2O$ (1:1)
Cr	$Ce(NH_4)NO_3 : HNO_3 : H_2O$ (1:1:1)
Ni	$HNO_3 : CH_3COOH : H_2SO_4$ (5:5:2)
Ti	$HF : H_2O_2$ (1:1)
Au	$KI : I_2 : H_2O$
Pt, Au	$HNO_3 : HCl$ (1:3), "aqua regia," H_2O dilution may be used
Ag	$NH_3 : H_2O_2$ (1:1)

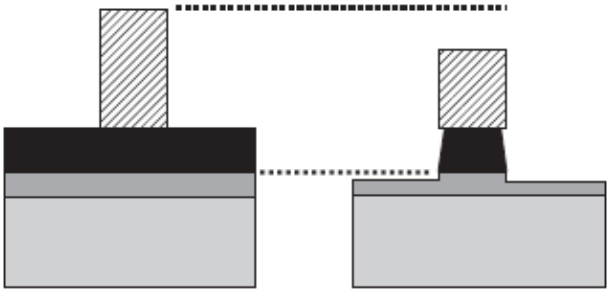

FIGURE 1.16: Etching with photoresist mask: thin film has been etched, with some etching of the underlying material and resist, too. There is some undercutting and the profile is not perfectly vertical.

If etched with a buffered HF (containing NH_4F), two species are present:

$$HF \rightarrow H^+ + F^- HF + F^- \rightarrow HF_2^-$$

Unbuffered HF etchants by comparison dissociate less readily and produce slower etch rates, and, additionally, they are powerful resist penetrants and failure due to pinholing and delamination are more likely than with buffered oxide etches.

The selectivity of the etchant for the desired material, compared to other materials that may be present, is important. For example, HF etches silicon dioxide, but also etches silicon nitride slowly. If nitride is the masking material, one must be concerned with how long it must remain exposed to the etchant. This is not a problem when simply patterning a thin film beneath the mask, but in sacrificial processes, collectively referred to as surface micromachining, in which long etch times may be required to remove all of the oxide beneath structural elements, the etch selectivity of protective layers is important.

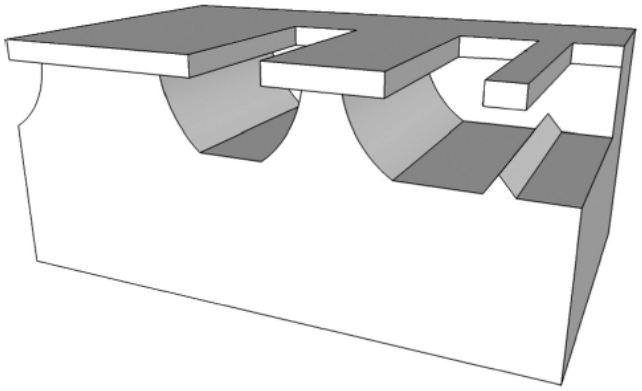

FIGURE 1.17: Undercutting in isotropic etching: wide lines are narrowed but narrow lines are completely undercut and released

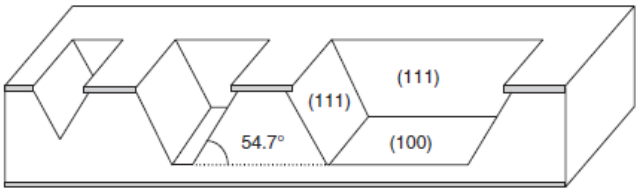

FIGURE 1.18: Anisotropic wet-etched profiles in $< 100 >$ wafer. The sloped sidewalls are the slow etching (111) planes; the horizontal planes are (100). Etching will terminate if the slow etching (111) planes meet

1.6.2 Silicon wet etching

The isotropic etching front proceeds as a spherical wave from all points open to the etchant. Because the etch front proceeds under the mask (resulting in undercut), isotropic etching cannot be used to make fine features (Figure 1.17). In fully isotropic etching lateral extent (undercutting) is identical to vertical etched depth.

Silicon isotropic wet etching is often done in $HF : HNO_3 : CH_3COOH$ (sometimes water is used instead of *acetic acid*). Depending on the ratio of *nitric acid* to *hydrofluoric acid*, the etch rate can be modified from a few hundred nanometers per minute to tens of micrometers per minute.

Anisotropic etching results in a profile following crystal orientation of silicon (Fig. 1.18), which is suitable for fine structure fabrication. Anisotropic wet etching take place because the different silicon crystal planes have different etch rates. *Potassium hydroxide* (KOH) is the prototypical anisotropic wet etchant for silicon. In KOH silicon (100) crystal planes are etched 200 times faster than (111) planes. KOH etching at about 80°C cannot be done with photoresist mask. Instead, resist is used to etch silicon dioxide or

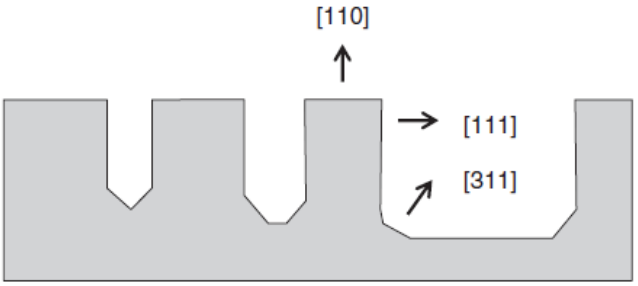

FIGURE 1.19: Etching of < 110 > silicon: slow etching (111) planes form vertical sidewalls.

silicon nitride, and after resist stripping silicon etching is done in KOH with oxide or nitride mask. Initially the shape is determined by the fast etching crystal planes (100) and (110) but in the end etching terminates when only slow etching (111) planes are present. When the slow etching (111) planes meet, etching will terminate. The etched depth is determined by the mask opening and the angle between the (111) and (100) planes, 54.7°. This angle is very characteristic of silicon MEMS structures. Note that it is important that the structures are aligned to the crystal planes (indicated by the wafer flat).

1.7 Deep Reactive Ion Etching (DRIE)

Reactive ion etching (RIE) and the closely related process of **deep reactive ion etching (DRIE)** are the most commonly used dry etching methods in the field of microfabrication. Here, general reactive ion etching mechanisms are discussed, and both the Bosch and the Cryo processes are introduced and compared with each other.
Both Bosch and Cryo processes typically utilize reactors which are equipped with two plasma sources: an *inductively coupled plasma* (ICP) source for high density plasma generation and a *capacitively coupled plasma* (CCP) source for controlling the ion energies.

1.7.1 Mechanism of etching

Plasma etching is performed in a vacuum chamber by **reactive gases** excited by **RF fields**. Both excited and ionized species are important for plasma etching. Excited reactive molecules and ionic species are accelerated by the RF field and impart energy directionally to the surface. Plasma etching is thus a combination of chemical (reactive) and physical (bombardment) processes. In a plasma discharge a number of different

FIGURE 1.20: DRIE Oxford Plasmalab 100 System

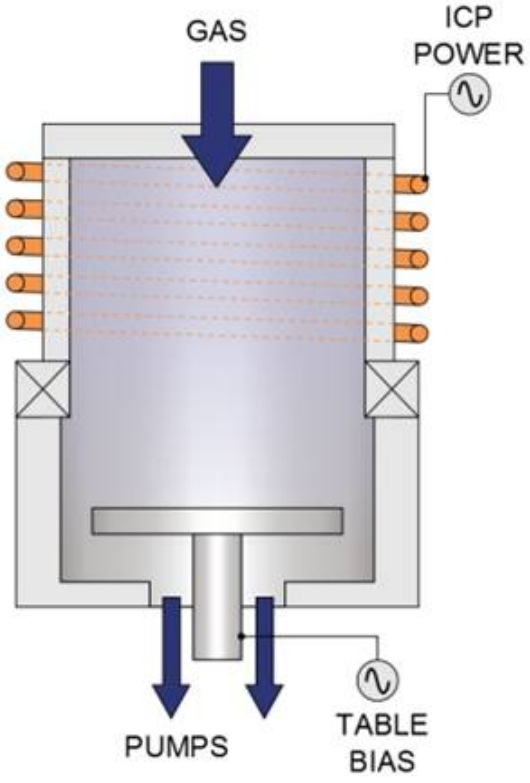

(A)

(B)

FIGURE 1.21: DRIE process chamber.

mechanisms are operative. The discharge generates both ions and excited neutrals, and both are important for etching.
Plasma etching is based on reaction product volatility. Silicon is easily etched by *halogens*: the *fluorides* (SiF_4), *chlorides* ($SiCl_4$) and *bromides* ($SiBr_4$) of silicon are volatile at room temperature at millitorr pressures. For this reason the gas most utilized to etch silicon is SF_6. No ion bombardment is needed for etching because the reactions are thermodynamically favored and the role of ion bombardment is used just to induce directionality. Fluorine is chosen for MEMS DRIE because of its high etch rate (SF_6 etches silicon an order of magnitude higher than Cl_2 or HBr) [5].

1.7.2 Bosch deep reactive ion etching process

The Bosch process is the most widely used DRIE technique. The processing of masked silicon wafer starts with a short **etching step** that utilizes a SF_6 based plasma. After this etching step, a thin fluorocarbon film is deposited on the wafer. The fluorocarbon film passivates the surface and prevents etching. Octofluoro cyclobutane (C_4F_8) is commonly used in the **passivation step**. It generates $(CF_2)_n$ radicals and results in a Teflon-like soft polymer film. At the beginning of the next short etching step, the fluorocarbon film is removed from horizontal surfaces. The SF_6 etching step is not anisotropic, but the plasma etches preferentially the horizontal surfaces due to directional ion bombardment, while the vertical sidewalls remain protected. The repetition of etching and passivation cycles results in almost vertical sidewalls [10].
The drawback of the process is the scalloping of the sidewalls due to the alternating etching and passivation steps (see figure 1.22). The sidewall roughness can be reduced by shortening the duration of the etching and passivation steps or by post processing [11].

1.7.3 Cryogenic deep reactive ion etching process

The cryogenic DRIE process does not have separate etching and passivation steps, as they both occur simultaneously. The etching is performed by a SF_6/O_2 plasma. At cryogenic temperatures (around -120° C) a passivating SiO_xF_y layer forms on top of the silicon surface [13, 14], which again is sputtered away from horizontal surfaces by directional ion bombardment. When the temperature is fixed, the thickness of the passivation layer is mainly determined by the O_2 flow rate. Too low oxygen flow results in the failing of the passivation layer and isotropic etching profiles, whereas too high oxygen content in the plasma leads to over passivation, a reduction to the silicon etch rate and the creation of black silicon. Changing the SF_6/O_2 ratio is the most convenient

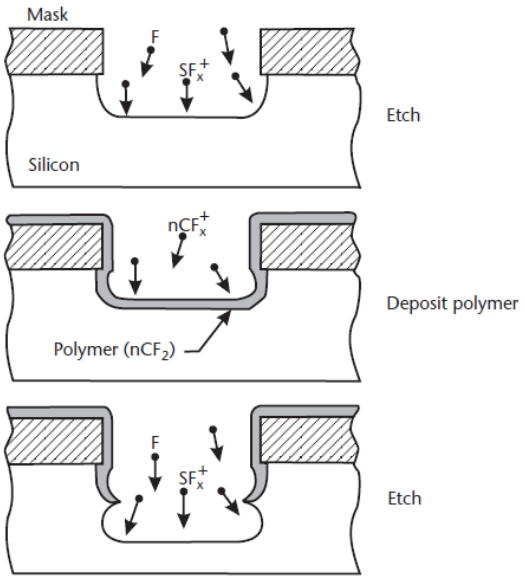

(A) Profile of a DRIE trench using the Bosch process [12]. The process cycles between an etch step using SF_6 gas and a polymer deposition step using C_4F_8. The polymer protects the sidewalls from etching by the reactive fluorine radicals. The scalloping effect of the etch is exaggerated.

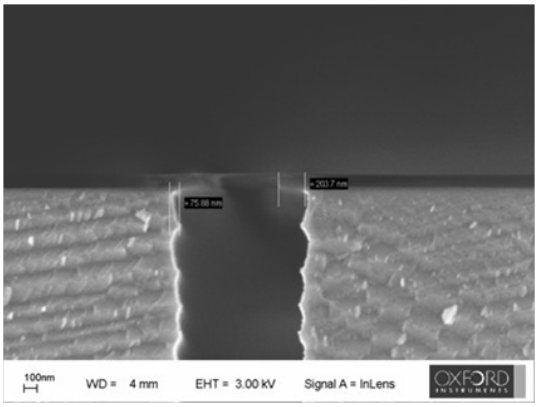

(B) SEM Image of typical etching profile

FIGURE 1.22: The Bosch process.

way to optimize passivation layer thickness and, ultimately, the sidewall angles. The etch rate of silicon is mainly dependent on SF_6 flow rate and the power of the ICP source. Higher SF_6 flow and ICP power increase the quantity of free fluorine radicals that result in the higher etch rate of silicon. The etch rate of the masking material is mainly dependent on the ion energies that are determined by CCP source. The ions have to have sufficient energy to remove the passivation layer from horizontal surfaces, but when a certain threshold is reached, an increase in CCP power only increases the etch rate of masking material and undercutting. The effect that the process parameters have on the conditions of the process and, ultimately, on the etch rate, selectivity and anisotropy of the process are summarized in Figure 1.23. The sidewall quality of structures etched using cryogenic DRIE is superior to Bosch process. Scanning electron microscope (SEM) images of cryo-etched structures are shown in Figure 1.24.

The substrate temperature plays a key role in cryo processes. The possibility of controlling the substrate temperature accurately at very low temperatures is crucial. In Bosch processes, the temperature control is also important, but the temperatures used are considerably higher.

The Bosch process uses etching and passivation steps that last only a few seconds. Therefore extremely high speed mass flow controllers, with sub-second settling times

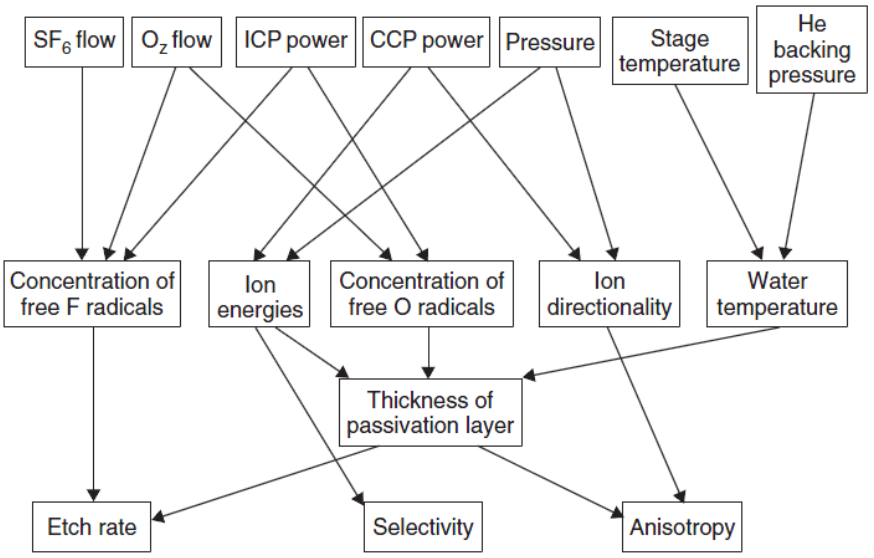

FIGURE 1.23: Guidelines for adjusting cryogenic DRIE process. Seven parameters that can be directly controlled using the equipment are shown at the top row. Their influences on process conditions and, ultimately, on the silicon etch rate, selectivity and anisotropy are indicated by the arrows. From [15].

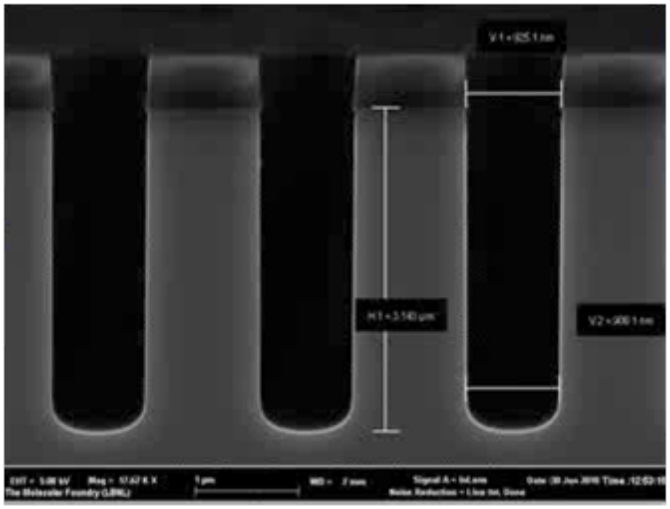

FIGURE 1.24: SEM image of structures etched using anisotropic cryogenic DRIE process.

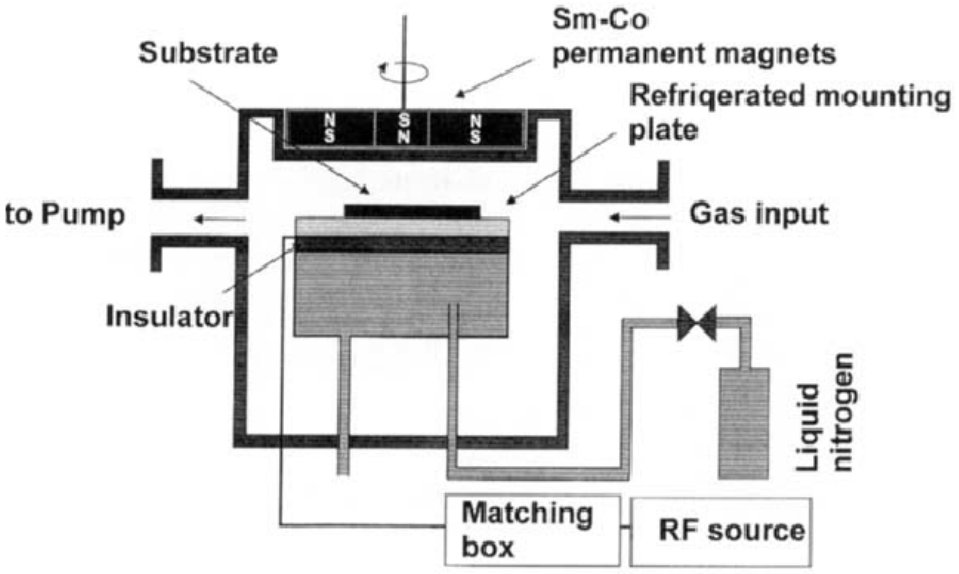

FIGURE 1.25: Cryo etching set-up. The substrate is cooled with liquid nitrogen. The magnetic field is to increase the ion yield in the plasma

are required. In the Bosch process it is also important to have an adequate ratio between ions and radicals. A relative ion concentration that is too high degrades the sidewall profiles. Generally, high etch rates are always achieved at the expense of undercutting and profile control and the etchable area must be small. Cryo processes typically have higher selectivity than Bosch processes, because ions that are at a lower energy are already enough to sputter the thin passivation layer.
Even though DRIE techniques are typically utilized to create sidewalls that are as vertical as possible, DRIE can be used to produce tilted sidewalls as well. By controlling the amount of passivation during the process, both positively and negatively tapered sidewalls are attainable [10]. If passivation is not used, DRIE is capable of producing completely isotropic etch profiles. Crystallographic dependent etching is also possible with cryogenic etching, when extremely low temperatures and low ion energies are used [16].

1.8 Rapid Thermal Processing/Rapid Thermal Annealing

Thermal treatments constitute a major fraction of front end processes. Thermal oxidation, diffusion and implant annealing all call for temperatures around $1000°C$. Batch furnaces, horizontal and vertical, with loads of up to 200 wafers are traditional workhorses of thermal processing. More recently single wafer rapid thermal processors (RTP) have come on the scene. These new developments enable very high temperature ramp rates

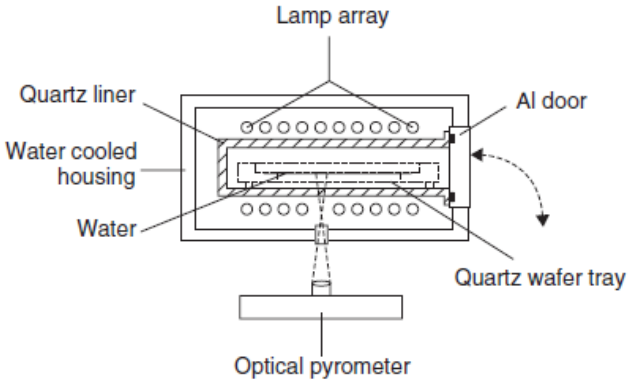

FIGURE 1.26: Tungsten-lamp heated RTP system, warm-wall system. From [5].

and combinations of very high process temperatures with very short process times, on the order of milliseconds and seconds instead of hours as in traditional furnaces.

Rapid heating is realized by three alternative methods: switching on powerful lamps, rapidly transferring the wafer(s) into a hot zone (Figure 1.27), or, for millisecond anneal, using lasers (either CO_2 or solid state lasers).

Tungsten halogen lamps deliver a kilowatt or two and a bank of lamps is needed, while a single xenon arc lamp can deliver tens of kilowatts. Ramp rates on the order of $50 - 300°C/s$ are used in RTP, a factor of 1000 higher than in horizontal furnaces. Arc lamp output is in the visible and near infrared; the tungsten lamp spectrum extends to 4 μm. This leads to some differences in processes because high-energy photons can contribute to, for example, oxidation.

Typically RTA systems are equipped with different mass flow controller for different gasses to be flushed in the inside of the chamber during the heating process. In this way different atmospheres can be exploited for different process requirements.

1.9 Anodic Bonding

Anodic bonding, also known as field-assisted bonding, is a simple process to join together a silicon wafer and a sodium-containing glass substrate (e.g., Corning Pyrex). It is used in the manufacturing of a variety of sensors, including pressure sensors, because it provides a rigid support to the silicon that mechanically isolates it from packaging stress. It is also used in microfluidic to bond etched silicon and glass thus obtaining microchannels and chambers. The bonding is performed at a temperature between 200° and 500° C in vacuum, air, or in an inert gas environment. The application of 500 to

FIGURE 1.27: Solaris 100 Rapid Thermal Processor.

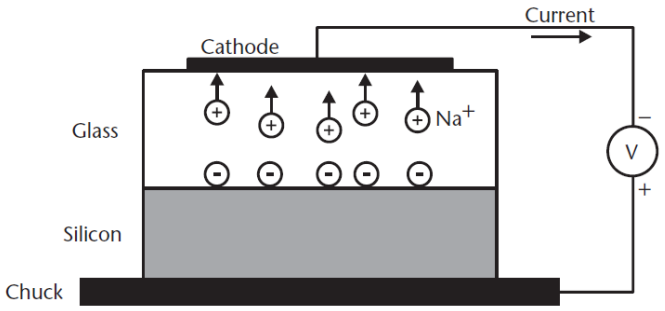

FIGURE 1.28: Illustration of anodic bonding between glass and silicon. Mobile sodium ions in the glass migrate to the cathode, leaving behind fixed negative charges. A large electric field at the silicon-glass interface holds the two substrates together and facilitates the chemical bonding of glass to silicon.

1500 V across the two substrates, with the glass held at the negative potential, causes mobile positive ions (mostly Na^+) in the glass to migrate away from the silicon-glass interface toward the cathode, leaving behind fixed negative charges in the glass (see Figure 1.28). The bonding is complete when the ion current (measured externally as an electron current) vanishes, indicating that all mobile ions have reached the cathode. The electrostatic attraction between the fixed negative charge in the glass and positive mirror charge induced in the silicon holds the two substrates together and facilitates the chemical bonding of glass to silicon. Silicon dioxide on the silicon surface should be removed before bonding, as a thin (100 nm) layer is sufficient to disturb the current flow and the bond. The coefficient of thermal expansion of the glass substrate is preferably matched to that of silicon in order to minimize thermal stresses.

Chapter 2

Preliminary studies on OTFTs for bio-sensing application

This part of my work is focused on the realization and study of *bottom-gate bottom-contact* **Organic Thin-Film Transistors (OTFTs)** using various organic semiconductors including porphyrins to form the active layer. The purposes are to evaluate the best choices upon materials and processes in a technological framework to provide both a silicon based structure to be useful for the study of many organic semiconductors, and, on the other hand, new characterizations of semicondutive behaviour of various compounds. The final goal of this work will be the implementation of these results for the fabrication of chemical sensors exploiting the three contacts nature of the transistor.

In the first part of this chapter will be discussed the fabrication process of a bottom-gate bottom-contact OTFT substrate. This device has been chosen in order to produce a versatile silicon substrate that can be used for the deposition and electrical characterization of a large number of organic compounds which are not compatible with standard lithographic processes. The device basically include a first metallization for the gate electrode, which has to be electrically isolated by a thin film of dielectric material, and source and drain electrodes patterned over the insulating layer. A organic semiconductive layer will be then deposited over the previously fabricated device.

In the second part we will discuss the semiconductors deposition techniques and characterization. The semiconductor of choice are mainly **porphyrins** but we will show preliminary results also on **squarains** and **PEDOT:PSS**.

Porphyrins analyzed are OEP, Zn[OEP], EptOTPP, Zn[EptOTPP] and Ni[ButOTPP]. Relatively to porphyrins we will include evaluation on sublimation behavior, scanning

electron microscopy (SEM) characterization which will give information about the surface morphology of semiconductors and X-ray Diffraction (XRD) for crystallization analysis. Finally electrical characterization will give information on device behavior and performance.

2.0.1 OTFT- based bio-sensors

OTFTs offer a great deal of promise for applications in chemical and biological sensing. For a broad range of sensing applications (e.g., medical diagnostics, food monitoring, detection of chemical, biological warfare agents, etc.), there is a demand for small, portable, and inexpensive sensors. OTFTs have many advantages over other types of sensors that may allow them to meet this need. Organic semiconductors can be deposited using low-temperature processes on a variety of substrates, including mechanically flexible ones. As a result, low-cost fabrication techniques can be used to produce OTFTs. Miniaturization of these devices is straightforward, so **portability**, **small sample volumes**, and arrays with many elements are achievable. In addition, they provide a response (current change) that is easy to measure with simple instrumentation. With these advantages, it is feasible that single-use, disposable sensors could be realized using OTFTs. Of course, it is also important in many applications for sensors to be able to **detect low concentrations** of specific analytes with high sensitivity and high selectivity. Here, too, OTFTs offer distinct advantages. Because OTFTs are based on organic semiconductors, precise organic synthesis can be used to fine-tune their chemical and physical properties. Both molecular structure and morphology can be adjusted to enhance sensitivity and selectivity. Furthermore, it is possible to **covalently integrate recognition elements** directly to the organic semiconductor to provide highly specific interactions with chosen analytes. Detection limits and sensitivity also benefit from the signal amplification that is inherent in transistor devices, allowing transistor-based sensors to outperform chemiresistors as well as amperometric and potentiometric sensors [17].

In general, OTFTs utilize a thin film of organic semiconducting material as the active layer of the transistor. Two electrodes (*source* and *drain*) in contact with the organic semiconductor are used to apply a source-drain voltage and measure the source-drain current that flows through the organic semiconductor, while a third electrode (*gate*) is used to modulate the magnitude of the source-drain current. The gate can be used to switch the transistor “on” (high source-drain current) and “off” (negligible source-drain current).

Depending on the organic semiconducting material used as the active layer, the mobile charge carriers can either be electrons (n-type material) or holes (p-type material).

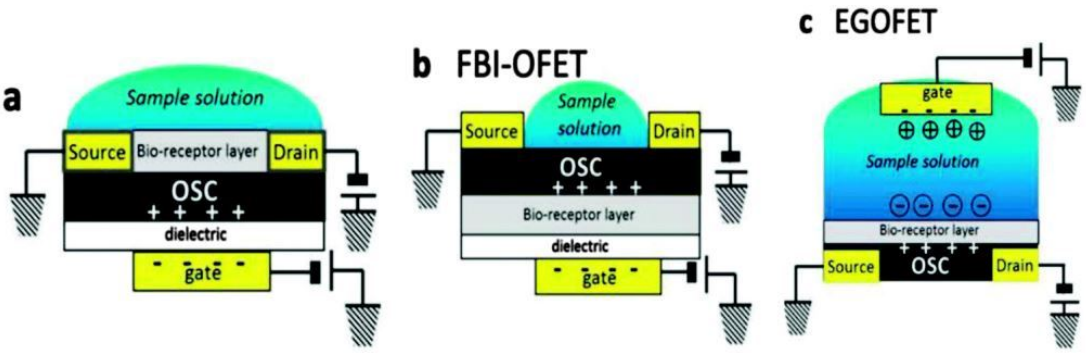

FIGURE 2.1: Typical architectures employed in OFET biosensors: **a.** bi-layer structure (dielectric–semiconductor) with receptors anchored at the semiconductor surface and exposed to the aqueous sample containing the analyte; **b.** functional bio-interlayer structure (FBI) with the receptor in the semiconductor channel, at the interface of semiconductor/dielectric; **c.** organic electrochemical transistor (OECT) and EGOFET (electrolyte gated OFET), both having similar geometries but subtle different operation principles. The bio-receptor layer is placed on top of the semiconductor channel. From [18].

OTFTs can be roughly classified into two primary categories: organic field-effect transistors (OFETs) and organic electrochemical transistors (OECTs) and EGOFET (electrolyte gated OFET). In OFETs (Figure 2.1 a, b), the source-drain current is modulated by field-effect doping, where the charge carrier density in the organic semiconductor is controlled by the gate electrode via an electric field applied across an insulating layer (gate dielectric). In OECTs and EGOFET (Figure 2.1 c) the source-drain current is modulated by electrochemical doping or de-doping, where the change in conductivity of the organic semiconductor is mediated by ions from an adjacent electrolyte. OECTs exhibit much lower operating voltages than OFETs, but due to the movement of ions involved in OECTs, their switching times are considerably slower (on the scale of seconds or longer) than those for OFETs (on the scale of milliseconds or shorter).

In the early stages of research, researchers tried first to adapt the electronic device structures to the world of biological media governed by both electronic and ionic motion. One such successful demonstration was accomplished by Zhenan Bao's research group that used water stable OFETs for sensing applications [19]. Employing a cross-linked polymer gate dielectric (*polyvinyl phenol*), and using either *pentacene* or *5,5-bis-(7-dodecyl-9H-fluoren-2-yl)-2,2-bithiophene* (DDFTTF) for the p-channel semiconductor, the fabricated devices displayed remarkable stability to operation in aqueous media without encapsulation, exceeding 104 cycles. Moreover the semiconductors showed sensitivity as low as parts per billion to various alcoholic analytes based on the sensing mechanism working in a similar manner to vapor detection: the small analyte or ions of interest diffuse at the dielectric/semiconductor interface and influence the charge transport in the

semiconductor channel. Nevertheless, bare (non-functionalized) OFETs have no specificity to the analyte, their responses being governed by weak and nonspecific van der Waals interaction. Selectivity of field effect transistors can be achieved by incorporating receptor molecules at different positions in the device structure and relying on these receptors to selectively bind to analytes of interest and consequently modify/alter the electric signal of the device. By doing so, the direct, label-free detection (bio-recognition) of analyte of interest will offer the alternative of miniaturization and fast processing of recorded data. Typical geometries derived from the classic OFETs to be employed for detection and signal transduction in the biological world (OFET bio-sensors) are shown in Figure 2.1 [20]. Both porphyrins and squarains we used in our preliminary study have the possibility to be functionalized ([21, 22]) so they represent a good strarting point for technological process integration.

2.1 Basic theory of operation of a OTFT

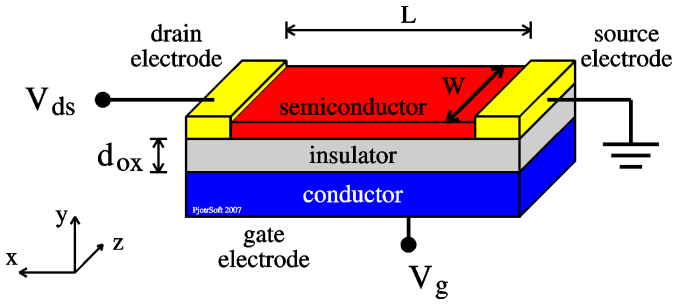

FIGURE 2.2: Cross-section of a thin-film FET showing the nomenclature used in this part.

A TFT is basically a resistor with two electrodes. The important device dimensions are its length L and width W (the thickness is not an important parameter). Nearby is placed a third electrode called the *gate*, resulting in a three-terminal device. Ideally, there is never current flowing from the gate to the resistor, and the only function of the gate is to modulate the charge density in the resistor. Once a substantial amount of free charge is induced in the resistor, it is said that a *channel* is formed. With a large density of free charge, the resistor becomes conductive and large external currents can be observed for relatively small biases applied. Although the device is still fully symmetric, the electrodes of the resistor are often called *source* and *drain* to denote their functionaiity in an electronic circuit. The source (often connected to ground) is that electrode that is emitting the majority carriers. For instance, in a TFT with a p-type (hole) channel, the source is at a relative positive bias. Holes are emitted from this source, travel through the resistor, and sink into the drain on the other side. The output

current I_{DS}, is a function of both drain-source voltage V_{DS} and gate-source voltage V_{GS}. There exists therefore two type of scans: either the gate is kept constant and the drain is varied, resulting in so-called *output curves*, or simply *I-V curves*, or the drain is kept constant and the gate varied resulting in *transfer curves*.

The active layer of a TFT can be made as thin as possible; as long as a continuous coverage of the insulating layer exists, the TFT works. Thus, a TFT can be made of a single monolayer and any additional layers deposited on top acts as passive buffers only for mechanically and chemically stabilizing the layer accommodating the current [23, 24].

The conduction mechanism in OTFT (and in all organic devices) is still an open question. Whether it is hopping conduction or band conduction it is not possible to distinguish between the two by simple measurements. Often the mobility is used as reference. High mobility indicates band conduction and low mobility points at hopping conduction with $10^{-6} - 10^{-4}\ cm^2/Vs$ being some sort of division line. However mobilities in a very large range ($10^{-8} - 1000\ cm^2/Vs$) can be explained without change in conduction mechanism [25]. The only distinction that can be made is *conductive states* and *non-conductive states* [26]. See Appendix A for a detailed description.

2.2 OTFT configurations

A number of OTFT structures can be obtained by varying the relative placement of the gate and source/drain electrodes with respect to the semiconductor layer. The resulting devices are described as *top-contact*, *bottom-contact*, *top-gate*, *bottom-gate*, or *dual-gate structures*. Each design possesses distinctive strengths and weaknesses in terms of operating mode and ease of fabrication. Thus, each structure may find unique usage in specific applications/configurations.

Depending on the arrangement of the source and drain contacts relative to the semiconductor layer, two configurations are possible, as depicted in Figure 2.4: a top-contact (or staggered) OTFT and a bottom-contact (or co-planar) OTFT. For top-contact OTFTs, the source and drain electrodes are placed on top of the semiconductor layer. For bottom-contact OTFTs, the organic semiconductor is deposited onto the gate dielectric and the prefabricated source and drain electrodes. The top-contact structure can have a performance advantage over bottom-contact devices in terms of lower contact resistance. On the other hand, the bottom-contact structure enjoys simpler and more robust processing schemes over top-contact structures. Research has shown that this small contact area tends to generate large contact resistance in bottom-contact OTFTs [27].

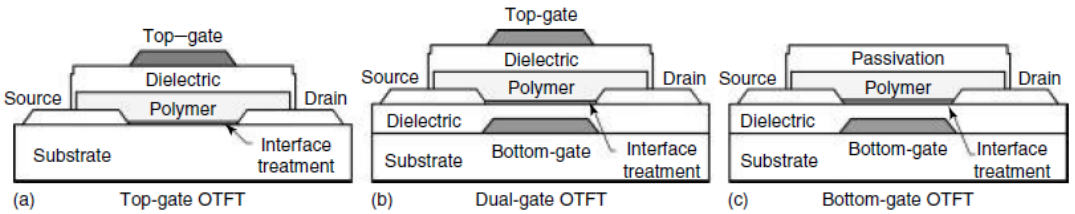

FIGURE 2.3: Cross-section of (a) top-gate, (b) dual-gate, and (c) bottom-gate OTFTs. Devices shown are in bottom-contact configuration.

A feature of top-gate OTFTs is that the gate dielectric can provide encapsulation and protection of the organic semiconductor layer. Encapsulation is suitable because most organic materials are chemically sensitive to environmental influence. However, the top-gate design poses some process integration challenges. First, the gate dielectric and gate electrode have to be deposited and structured on top of the organic semiconductor, and this process must preserve the organic material. Secondly, vertical interconnects and vias between the conductive layers have to be built through the organic semiconductor; this necessitates developing a compatible patterning/etching process for the organic layer.

From a processing perspective, the bottom-contact design is preferable over the top-contact structure. This is because the deposition of the organic semiconductor constitutes the last fabrication step in bottom-contact OTFTs (assuming no encapsulation), and is not limited or affected by other processing steps. Thus, there is greater flexibility in selecting a patterning/deposition method for the various device layers. If an inorganic dielectric is used, the source/drain contacts can be patterned by a photolithography technique to deliver higher resolution features. On the other hand, the top-contact design is susceptible to physical damage of the organic layer from subsequent processing of source/drain contacts, or from metal–semiconductor reactions (which may influence the contact resistance). With the top-contact architecture, contacts are often deposited through shadow masks, with substantial loss of resolution. Moreover, the metal–organic interaction during metal deposition may lead to deterioration of device performance. For the results reported in this work, fabrication processes are geared toward bottom-contact structures to ensure minimum process-induced disruption to the organic semiconductor layer.

2.3 Process Flow

In this thesis work we fabricated two similar structures: a structure with *highly doped silicon* acting both as substrate and gate electrode, and another structure with a *metallic*

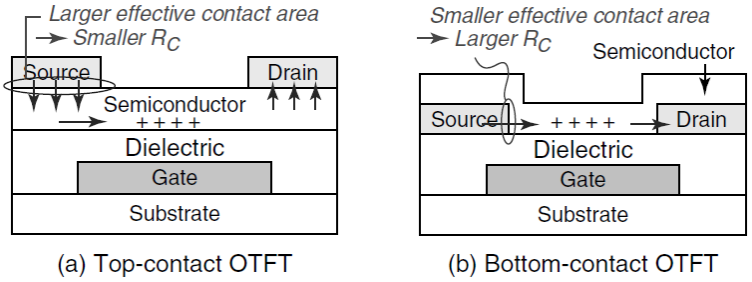

FIGURE 2.4: Cross-section of two bottom-gate OTFT configurations: (a) top-contact and (b) bottom-contact.

gate over a silicon/silicon dioxide or silicon/silicon nitride substrate. The first process has been done using just one lithographic mask and the second using three masks.

Masks have been fabricated using a laser writing technique on chromium coated soda lime glass (also coated with iron oxide to prevent light scattering). The process for fabricating photolithographic masks is the following.

- Exposition of coated soda lime glasses.
- Developing of the mask using suitable developer.
- Etching of the iron oxide/chrome thin film usign a Ce based solution: a mixture of *perchloric acid* $HClO_4$ and *ceric ammonium nitrate* $(NH_4)_2[Ce(NO_3)_6]$

The reaction undegoing during Cr etch is:

$$3Ce(NH_4)_2(NO_3)_6 + Cr \rightarrow 3Cr(NO_3)_3 + 3Ce(NH_4)_2(NO_3)_5$$

Chromium nitrate steadily produced during etching forms a dark film on the chromium surface and - due to its aqueous solubility - is dissolved in the etchant.

2.3.1 Basic One-Mask Processing Scheme for Bottom-Gate OTFT

The fabrication sequence of a bottom-gate bottom-contact OTFT on highly doped Si substrate as gate, employing a single patterning step (i.e., one-mask process), is depicted in Figure 2.9. The source/drain contacts are defined by photolithography and patterned by wet etching of a metallic thin film previously deposited on the substrate . Although this common-gate configuration may not deliver devices with the best overall performance (e.g., overlap capacitance will limit speed) and may not be highly compatible for circuit integration (e.g., lack of individually addressable gates), this design provides

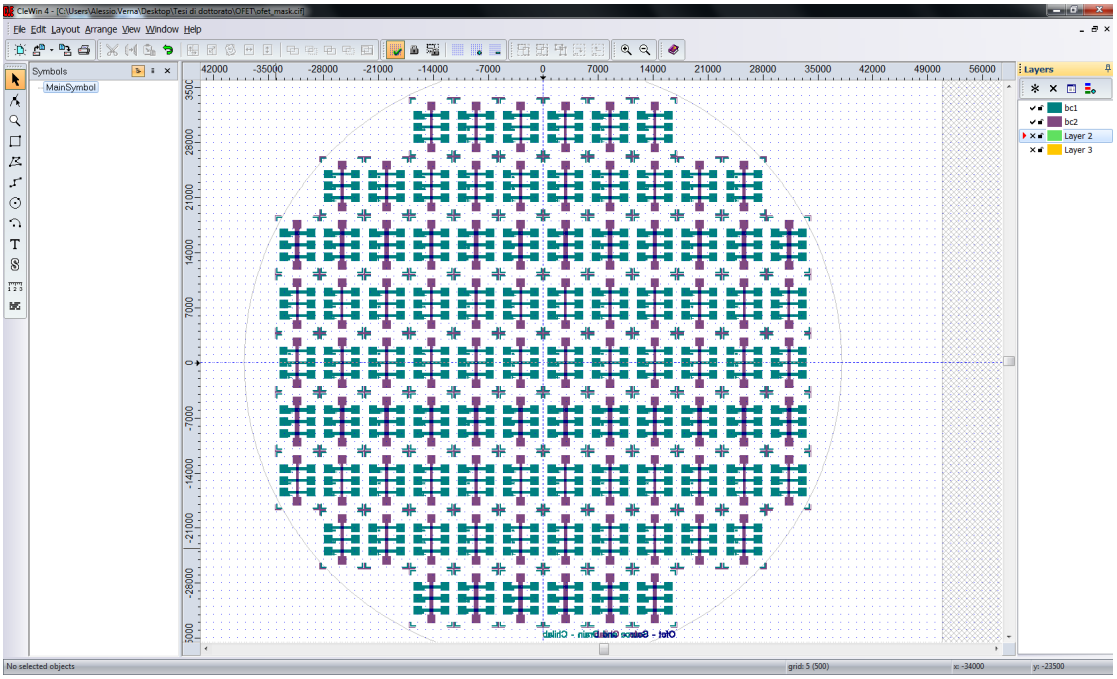

FIGURE 2.5: CAD for masks realization. Entire mask is shown.

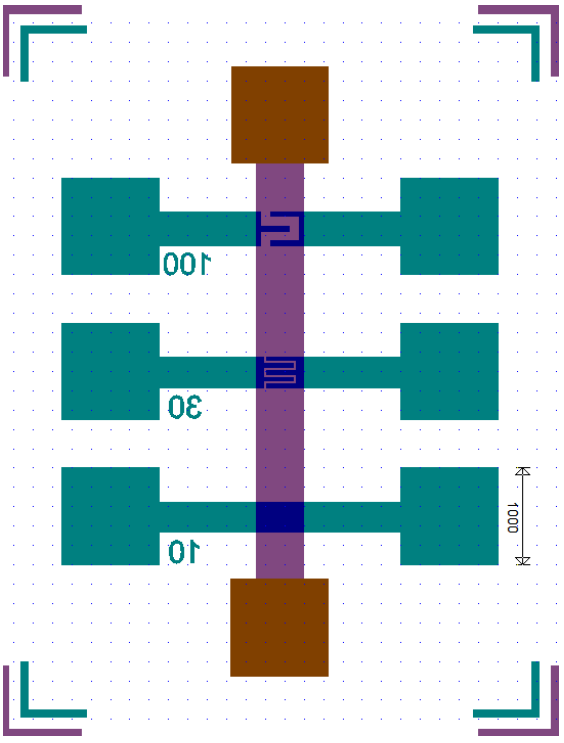

FIGURE 2.6: CAD of OTFT single device. Source and drain electrodes have been designed with 3 different channel length: 10 μm, 30 μm and 100 μm.

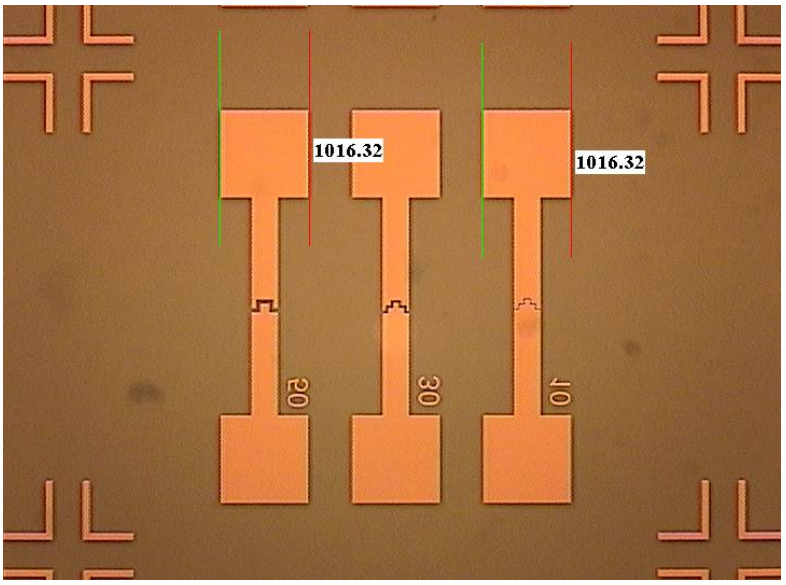

FIGURE 2.7: Optical microscope image of the lithographic mask for source and drain contacts definition.

the simplest method to evaluate material systems and interfaces. Furthermore, it has the least number of processing variables and the lowest possibility of process-induced damage, thus one can focus strictly on evaluation and/or characterization studies of new material systems. This configuration and fabrication scheme serves as the basic platform for the dielectric and interface investigations in this work.

We used n++ silicon substrate with a thermal oxide 190 nm thick. A metallic thin film (usually *silver*) was deposited on the surface by e-beam evaporation. The electric contacts were then defined by with etching using Fujifilm HPR 504 photoresist. We then removed the silicon oxide from the back of the wafer reaching the gate electrode (the doped silicon bulk) using a BOE 7:1 solution.

2.3.2 Fully-patterned bottom-gate bottom-contact OTFT Scheme

Figure 2.10 shows the processing scheme for a photolithographically-defined fully-patterned bottom-gate bottom-contact OTFT, developed in this research. First, the bottom-gate metal is deposited and patterned (mask 1), followed by deposition of the gate dielectric across the wafer. A second metal layer is deposited on the dielectric surface, and is subsequently patterned by photolithography to define the source/drain contacts (mask 2). The last step (mask 3) concerns forming a via in the dielectric to reach gate contact pad.

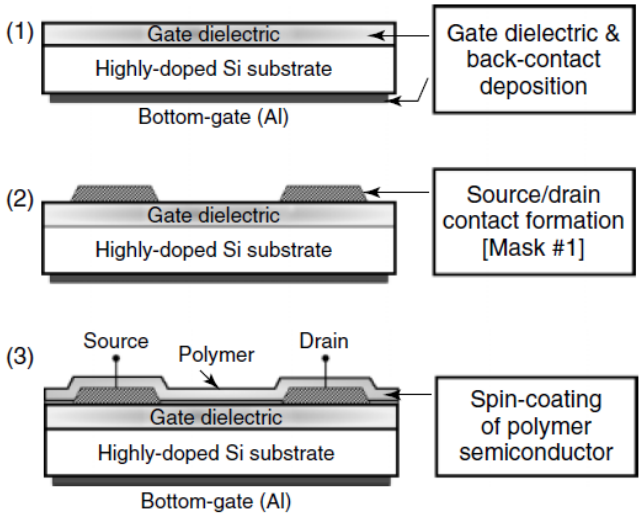

FIGURE 2.8: Fabrication sequence of bottom-gate bottom-contact OTFT on highly-doped Si substrate with a one-mask patterning step to define the source/drain contacts.

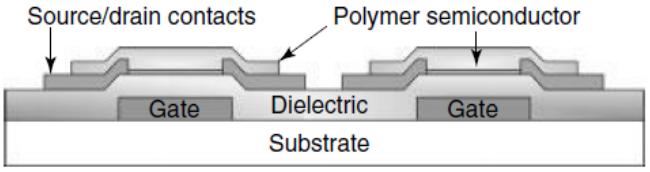

FIGURE 2.9: Illustration of individually addressable gates on the same substrate, which is a basic requirement to enable circuit implementation.

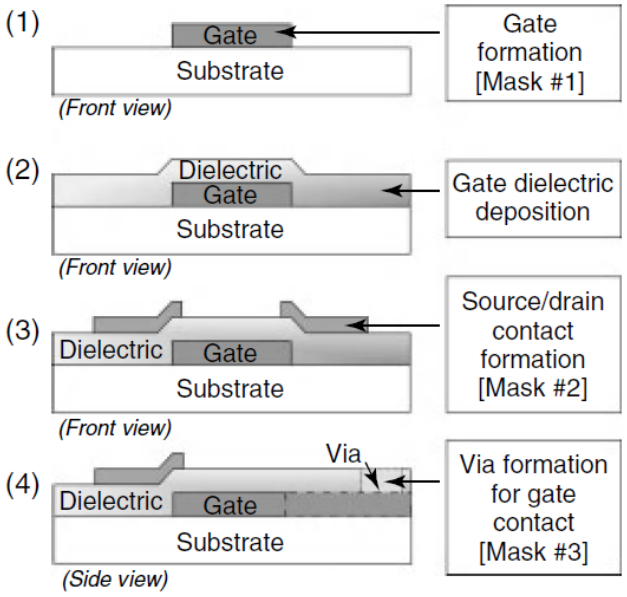

FIGURE 2.10: Fabrication sequence of bottom-gate bottom-contact OTFT by a three-mask photolithography process.

2.4 Material selection and fabrication details

2.4.1 Gate and gate dielectric

The gate dielectric is one of the most critical materials for organic transistor performance. It has an important function in establishing field-effect operation in TFTs. A general specification for the gate dielectric of TFTs is summarized as follows: the dielectric material has to withstand strong electric fields without breakdown, must have good insulating properties and low rate of charge trapping at lower electric fields and it should form a high quality interface with the semiconductor layer [28]. In addition, the dielectric films should possess low trapping density at the surface, low surface roughness, low impurity concentration, and compatibility with organic semiconductors.

A high-k dielectric (e.g., Al_2O_3, Ta_2O_5, TiO_2) is a good candidate for the gate dielectric in OTFTs because its high-k value can increase the intrinsic gate capacitance ($C_i = k\epsilon_0\frac{A}{d}$) of a transistor, which in turn increases the current output. Thus, high-k dielectrics can partially compensate for the relatively low mobility (μ) of the organic semiconductors, and can enable device operation at lower drive voltages. However, a key shortcoming of high-k materials is their higher degree of disorder and surface roughness, which can create traps, reduce mobility, and lead to localization of carriers at the dielectric/semiconductor interface [28].

From a process oriented point of view the bottleneck of the realization of a patterned metal-insulator-metal structure is to produce a good insulating layer. The dielectric performances of the insulator not only depend on the material of choice, but depend on the following factors:

- Smoothness of the underlying metal layer
- Compactness of the oxide (crystal dimensions and holes in the structure)
- Thickness of the oxide

Due to these eventual problems the choice of the suitable oxide depending on the fabrication capabilities may be difficult. We present here two approaches. The first using **alumina** (Al_2O_3) and the second using **tantalum oxide** (Ta_2O_5). For both approaches, as will be highlighted, thermal treatments are necessary. For this reason also the metal for gate electrode must be chosen carefully. The metal must be a good conductor, in order to be good performing as gate electrode even if very thin (less than the desired oxide layer) and it must preserve his uniformity also after temperature annealing up to 800°. Problems in high temperature could be island formation, cracking or diffusion of

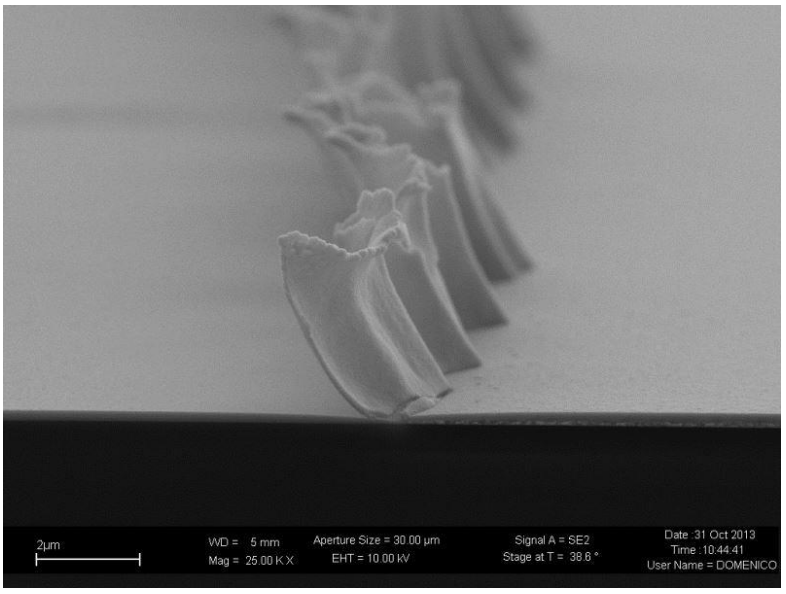

FIGURE 2.11: Metal ribbon formed by adhesion of metal on the photoresist mask.

the metal in the adhesion layer. Also for what concerns the gate metal we tried two different solutions: a sputtered platinum thin film over sputtered tantalum adhesion layer and a sputtered molybdenum layer. The system used was a RF magnetron sputtering Kurt J. Lesker PVD75.
The patterning technique of the gate also affects the performance of the structure. The surface of the metal must be as smooth as possible and defect-free because any bumps or residual metal can carry to a short circuit of the three layers device. **Tantalum/-platinum** thin films cannot be easily patterned via wet etching, only aqua regia (nitric and chloridric acid) can be employed, but this etching is fast and not easily controllable, resulting in a rough edge morphology of the pattern, which negatively affects the performance of the device. Thus we employed a lift-off process to pattern the tantalum/-platinum layer. But also for this technique problems may occur: due to the fact that sputtering deposition tends to be multidirectional, if a too thick photoresist is chosen, deposited material can adhere to vertical side walls of the resist forming characteristic ribbons (see figure 2.11) resulting in an impossible electrical isolation of the gate.

Due to the difficulties in fabricating good performing devices with tantalum/platinum gate electrode we chose sputtered **molybdenum** which is easily patterned by wet etching using a E6 metal etchant: 80 volumes of Phosphoric Acid (at 85% wt), 5 volumes of Acetic Acid (Glacial), 5 volumes of Nitric Acid (at 60% wt) and 10 volumes of DI water (16:1:1:2 ratio).

We deposited then **alumina** by e-beam evaporation using a ULVAC EBX-14D system at high vacuum condition (10^{-7} torr) with 10kV beam acceleration voltage. As shown in

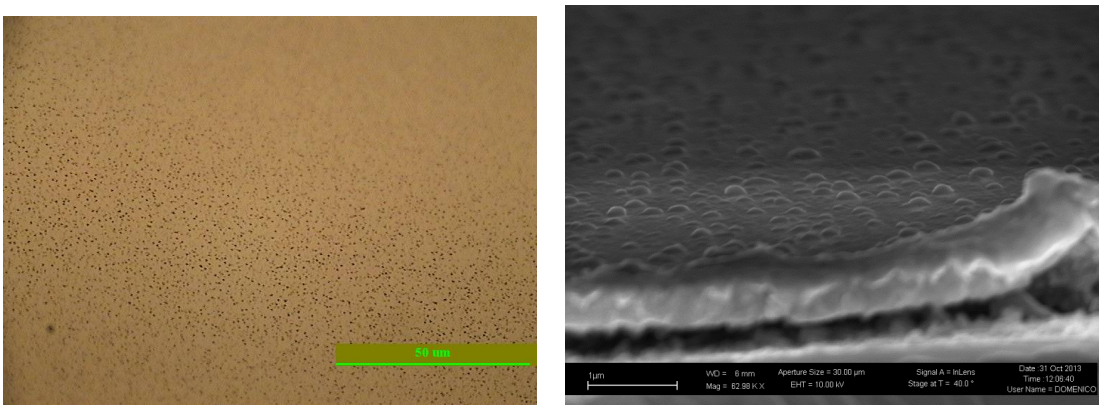

(A) (B)

FIGURE 2.12: Optical and SEM a image of alumina layer: bumps over the surface are observed.

figures 2.12 resulting thin film present good surface coverage and acceptable uniformity but sub-micrometrics bumps are present on the surface due to dynamics of thin film formation which probably are affected by the temperature of the substrate and kinetic energy of alumina molecules. Evaporation is a simple and cost effective technique to produce alumina thin film but the process must be carefully calibrated. In fact electron beam current must be kept quite low (in our case 60 mA) because when the energy of the beam exceed a threshold value aluminium and oxigen atoms tend to separate leading to two detrimental consequences: vacuum condition gets worse reaching auto shut-off of the beam in the evaporation system and the melting material looses stoichiometry becoming black and so not suitable for following depositions. To improve compactness of the alumina layer we subjected the samples to a rapid thermal annealing of 1 minute at 800° C with atmospheric gas (no gass flow) with a 50° C/s increasing temperature rate. The annealing was necessary to obtain an insulating film, because metal deposited over not annealed, or lower temperature annealed samples, was able to percolate in the alumina film short circuiting the device. Rapid thermal annealing (RTA) was performed using a RTP Solaris 100 equipped with 13 quartz halogen lamps on top and bottom of the wafer.

For what concerns **tantalum oxide** the approach we used has been different: we employed the thermal oxidation of tantalum metal [29] in controlled atmosphere. We deposited a tantalum thin film (approx 60 nm) over the gate electrodes using a RF magnetron sputtering followed by a thermal oxidation. We performed the annealing at $600°C$ for 15 minutes with a $10°C/s$ increasing temperature rate in oxidizing atmosphere. We chose pure oxigen atmosphere and a oxigen/nitrogen (50% - 50%) blend atmosphere both with a total flux of 2 sccm. We noticed that the thickness of the oxidized film

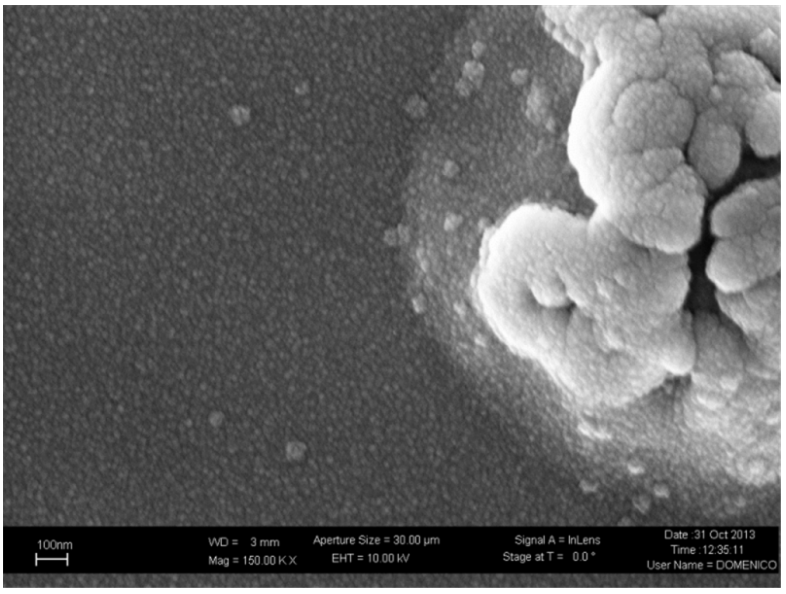

FIGURE 2.13: SEM image of tantalum oxide layer morphology: the insulating layer uniformly covers the underlaying layer even on pre-existing defects.

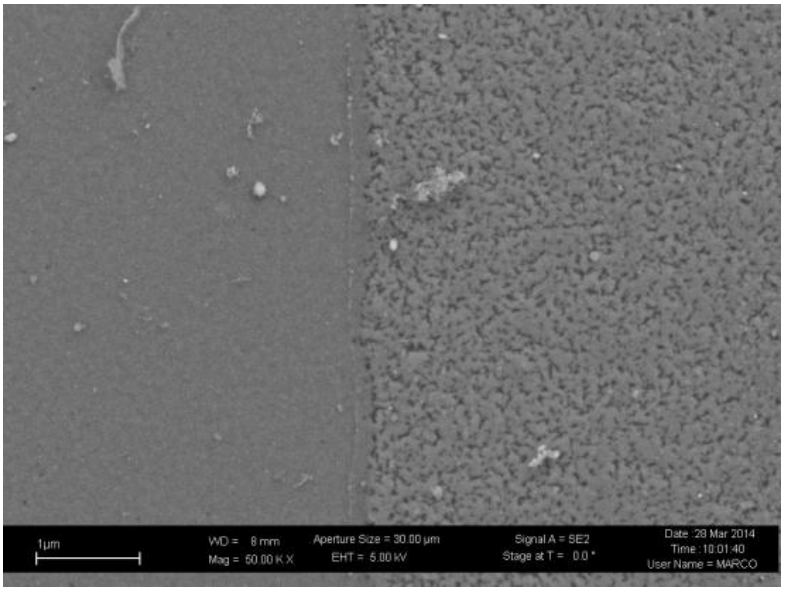

FIGURE 2.14: SEM image of tantalum oxide layer morphology growth on different surfaces: tantalum oxide cristals on metal (right) and silicon nitride (left) are different.

rises of 40% - 50% with respect to the metallic film, due to the oxidation process. With simple naked eye inspection the film produced in this manner appear very transparent with no noticeable macroscopic defects.

To analyze the stoichiometry of the fabricated samples we used X-Ray Photoelectron Spectroscopy (XPS). XPS is a surface sensitive chemical analysis technique that can be used to analyze the surface chemistry of a material. It is a quantitative spectroscopic

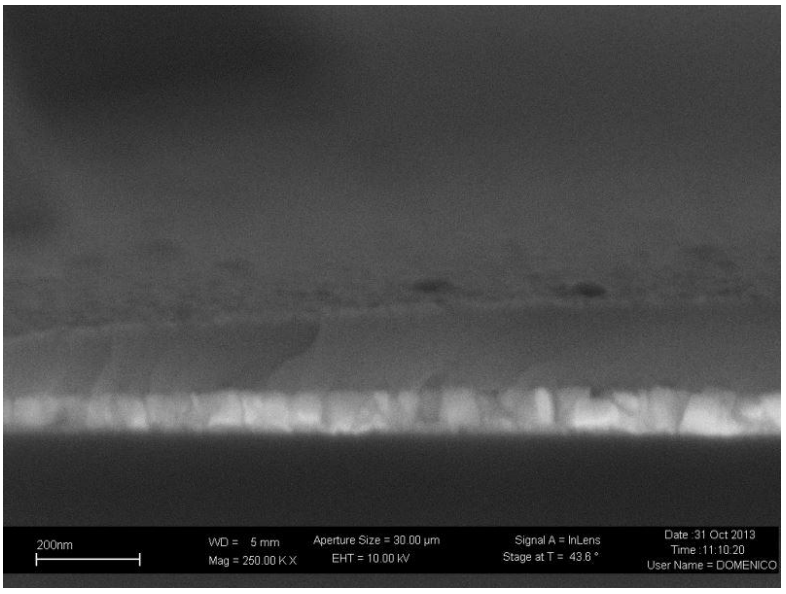

FIGURE 2.15: SEM image of a tantalum oxide layer over the metallic gate in cross section.

technique that measures the elemental composition, empirical formula, chemical state, and electronic state of the elements that exist within a material's surface. In this chapter, XPS is used to study the surface chemical composition (i.e., elemental concentration) of as evaporated Al_2O_3 and Ta_2O_5 thin films with varying annealing conditions. Both surface spectrum (Figures 2.16 and 2.18) and depth profiles are provided.

The depth profile of oxides samples was analyzed by in situ XPS ion beam sputtering with argon (Ar). The results are reported in figure 2.17 and where the changes in elemental concentrations of oxygen (O), tantalum (Ta), aluminium (Al) and nitrogen (N) on the samples were analyzed as a function of depth (or etch time) by interleaving XPS analysis and argon ion sputtering.
XPS measurements were obtained using a PHI 5000 Versa Probe X-ray photo electron spectrometer.

Both spectra and depth profile show good stoichiometry of the oxides, but, in the case of Ta_2O_5 annealed with O_2/N_2 atmosphere, still a presence of nitrogen can be detected in the thin film, thus we discarded this process.

2.4.2 Metal contacts

The choice of material for source/drain contacts is quite stringent; conscientious energetic matching between contact and semiconductor is important to establish efficient charge injection in OTFTs. Ohmic contact is desirable, which requires the work function

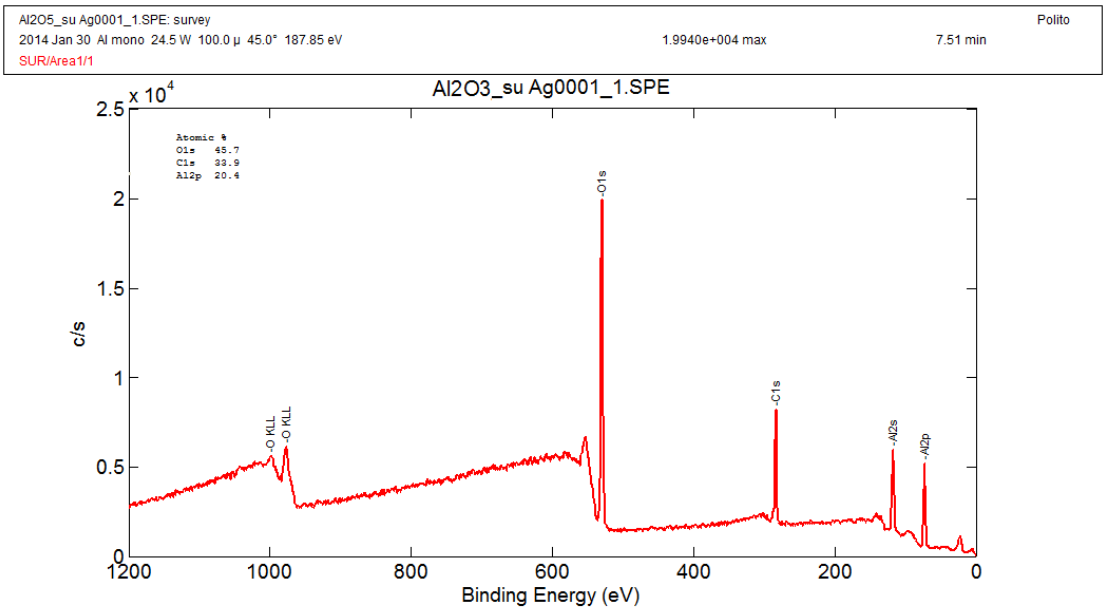

FIGURE 2.16: XPS spectrum of Al_2O_3.

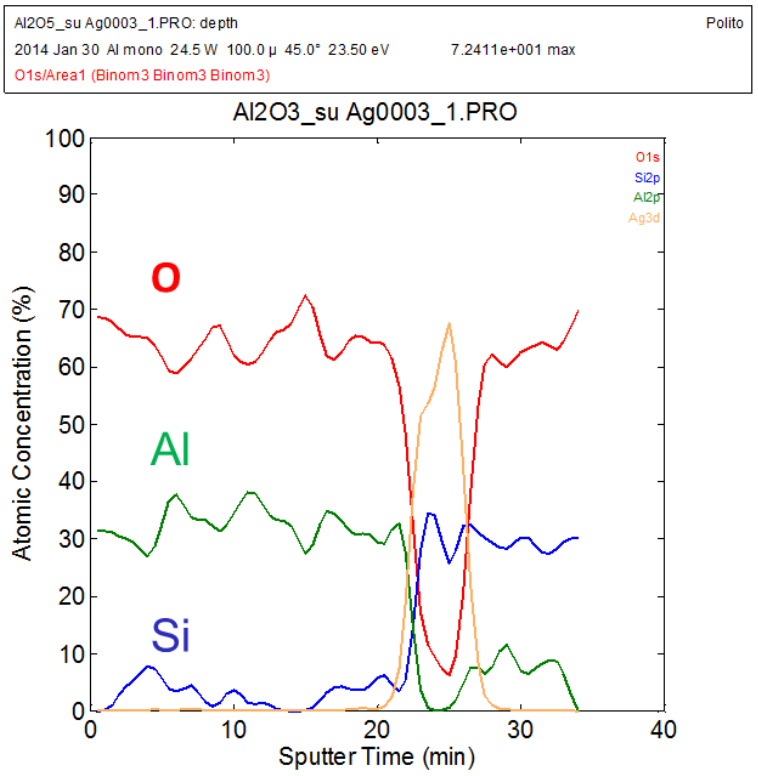

FIGURE 2.17: XPS depth profile of Al_2O_3.

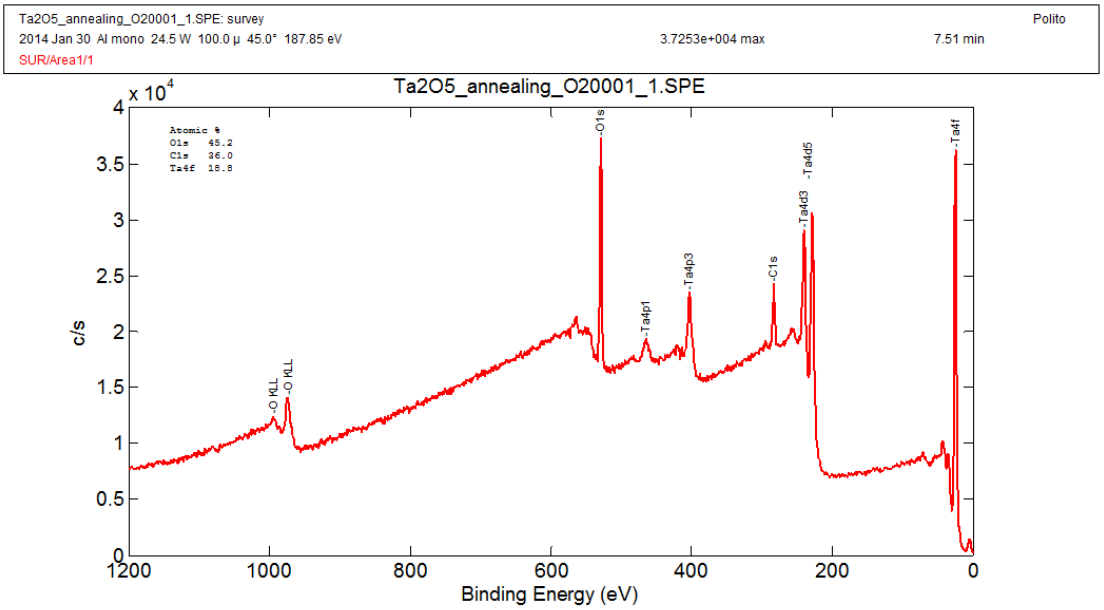

FIGURE 2.18: XPS spectrum of Ta_2O_5 oxidized in O_2 atmosphere.

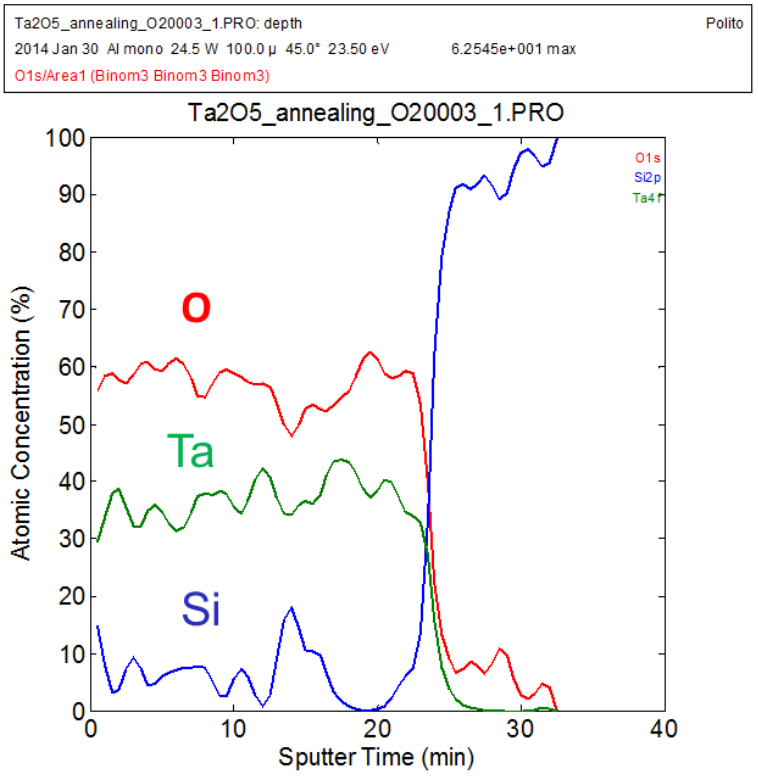

FIGURE 2.19: XPS depth profile of Ta_2O_5 oxidized in O_2 atmosphere.

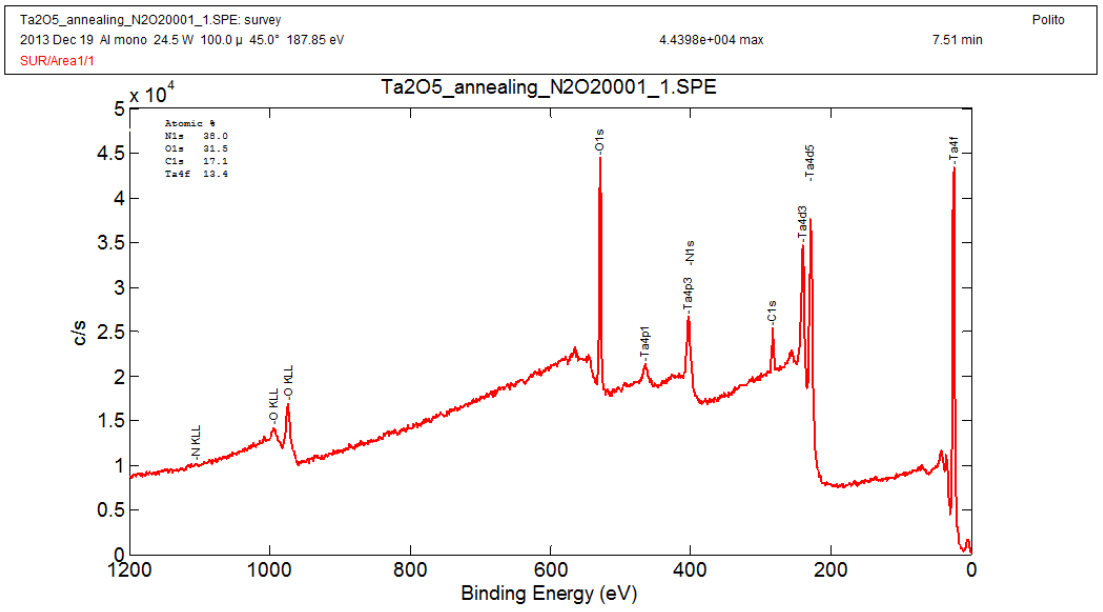

FIGURE 2.20: XPS spectrum of Ta_2O_5 oxidized in O_2/N_2 atmosphere.

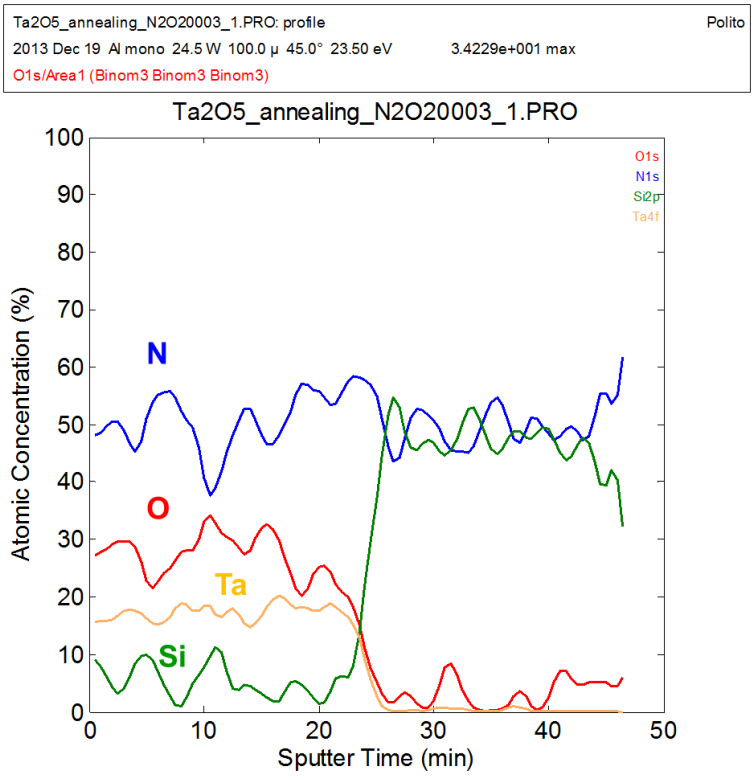

FIGURE 2.21: XPS depth profile of Ta_2O_5 oxidized in O_2/N_2 atmosphere.

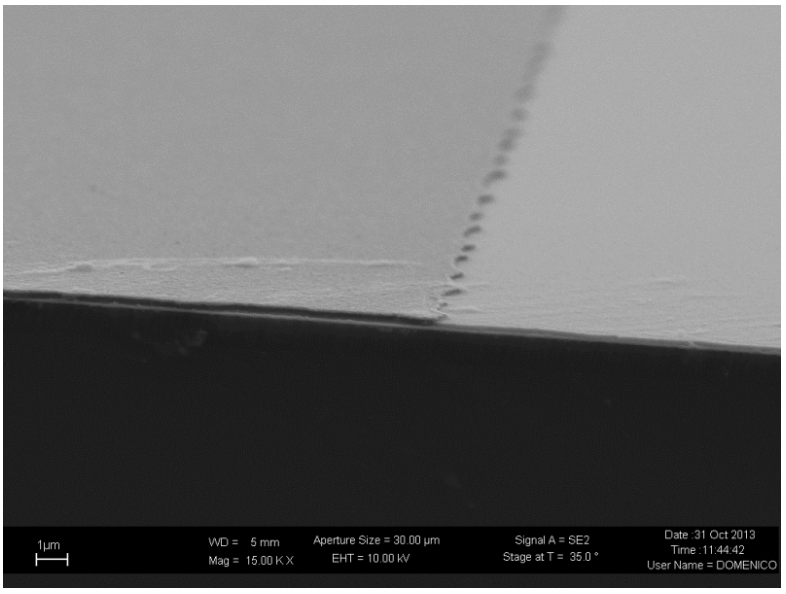

FIGURE 2.22: SEM image of silver electrode over tantalum oxide: the edge is not perfectly smooth for underetching of metal under the photoresist mask.

of the contact metal to match with the HOMO of the organic semiconductor in the case of a p-type OTFT, and with the LUMO in the case of an n-type OTFT. This implies a high work function metal for p-type OTFT and a low work function metal for n-type OTFT [4].

In our work, since the choice of semiconductor and relative deposition process was an open task, the requirements for the metal were more process-oriented. In fact the metal of choice, besides being a good condutor, had to be quite stable in atmospheric environment and easily patterned by wet etching, with the additional requirement for the etchant to be not aggressive on the underlying layer (alumina or tantalum oxide). In the case of tantalum oxide gate, being very stable under chemical attack, a large range of metal could be used. In the case of alumina only gold (Au), silver (Ag), copper (Cu) and few others were fulfilling the requirements. After evaluation, for the purpose of providing preliminary characterization of the structure, we chose silver.

Patterning of silver was obtained by wet etching using a $NH_4OH : H_2O_2 : H_2O$ solution in 1:1:10 volumetric proportion. This etching is quite fast and underetch may occur (see Figure 2.22) but the resulting reduction in the dimension of the pattern was negligible for our purposes. In fact silver oxidize in contact with hydrogen peroxide, and silver oxide is made soluble in water by ammonia with the reaction:

$$Ag_2O + 4NH_4OH \rightarrow 2[Ag(NH_3)_2]OH + 3H_2O \tag{2.1}$$

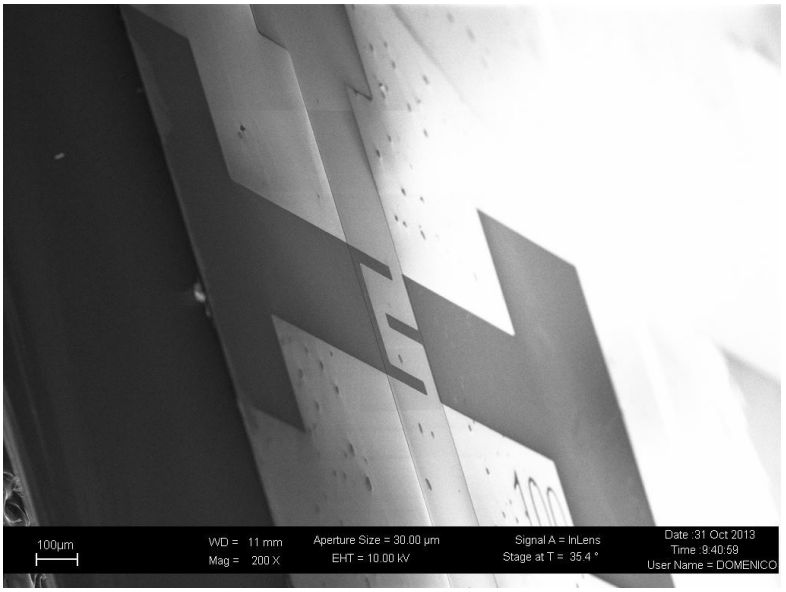

FIGURE 2.23: SEM image of the completed structure: source and drain contacts deposited on gate and gate insulator are visible.

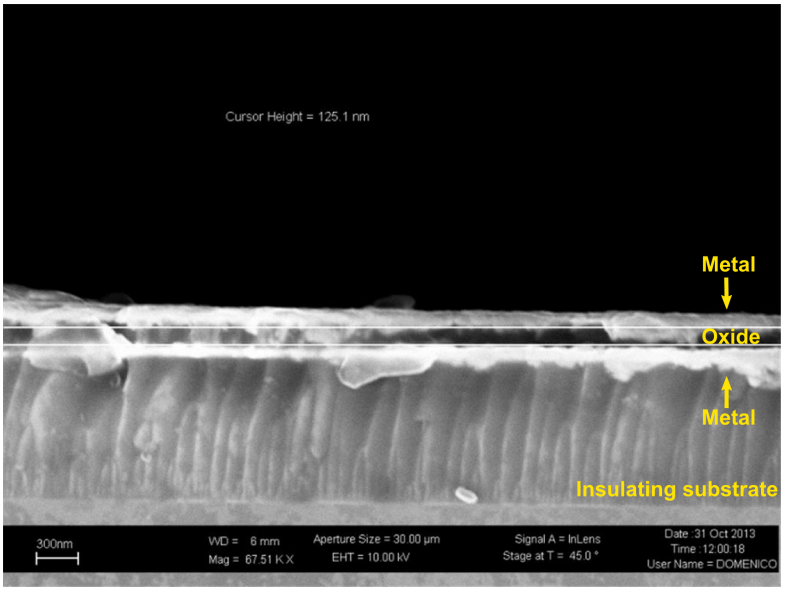

FIGURE 2.24: Cross section of the metal - oxide - metal structure: the oxide layer is clearly distinguishable.

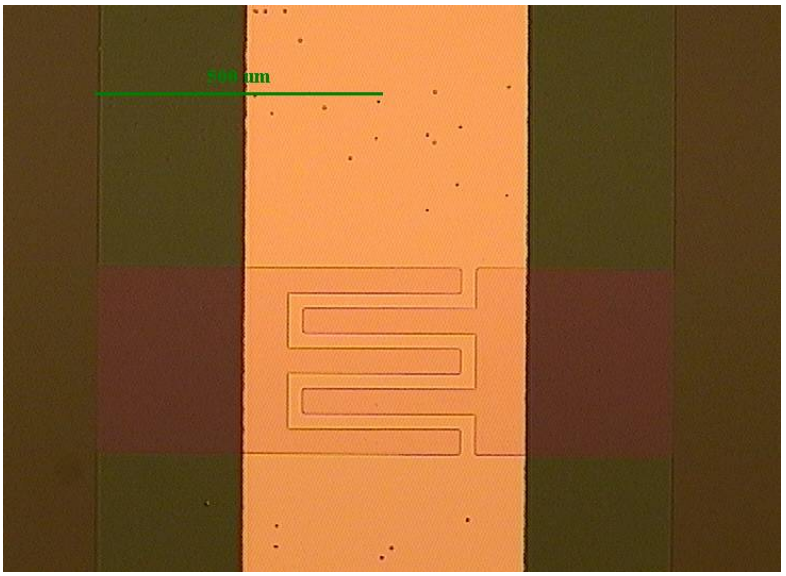

FIGURE 2.25: Optical microscope image of alumina thin film over a metallic electrode thinned by basic developer exposure (TMAH) on selected areas.

Patterning of metal contacts can be performed also via lift-off, but, if the resist developer is composed of *Tetramethylammonium hydroxide* (TMAH) or other basic solutions (KOH, NaOH), the evaporated alumina thin film can be damaged resulting in bad insulating properties (see Figure 2.25). To overcome this problem we patterned silver via wet etching as said before. Another solution if the metal of choice etching is not compatible with the process could be using organic solvent based photoresit developer.

2.4.3 Etching of the insulator

Last step of the fabrication process before the organic semiconductor deposition is the etching of the insulating layer to form a via for the gate metal contact. Before this step the insulator also works as protective layer for the gate metal during thermal oxidation or annealing of the insulator. To pattern alumina we used a wet etching: a Hydrofluoric acid (at 39.5% wt) and DI water solution (in a 1:10 ratio).

Wet etching of tantalum oxide is quite difficult to perform, so we use a Deep Reactive Ion Etching: The main parameters of the etching were: SF_6 with flow rate at 60 sccm CCP power at 12 W, ICP power at 1000 W. Temperature was set at -20° C, with baking Helium at 10 sccm, and chamber pressure was set at 15 mtorr. Samples were previously masked with Microchemicals AZ 9260 photoresist. No particular care on the etch rate was taken because the underlying metal layer (the gate pad) acted as stop etch.

2.5 Organic layer: porphyrins

Porphyrins are widespread compounds in nature, where they play essential functions for life, like Heme group of hemoglobin and chlorophyll; because of the richness of their properties, they have assumed a peculiar role in different fields of disciplines, ranging from medicine to material science [30].

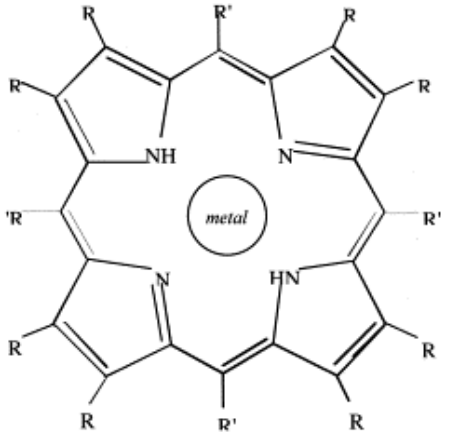

FIGURE 2.26: Basic structure of a porphyrin. The central metal can host many of the metal of the periodic table, while at the R, R' position lateral groups can be linked.

A great number of features makes porphyrins eligible as good "sensing material" able to detect the volatile organic compounds present in the environment or chemical compounds in aqueous solutions. Porphyrins in fact are rather stable compounds and their properties can be finely tuned by simple modifications of their basic molecular structure (see Figure 2.26).

The coordinated metal, the peripheral substituents, the conformations of the macrocyclic skeleton influence the coordination and the related sensing properties of these compounds [31]. Almost all metals present in the Periodic Table have been coordinated to the porphyrins [32]; furthermore the organic chemistry of these compounds is well developed, and a wide range of different substituents can be introduced at their peripheral positions [33]. Porphyrins are also insoluble in water, thus are suitable for wet chemical sensing investigation in acqueus environment. All together these characteristics increase the versatility of these molecules and different transducers have been proposed for porphyrin-based chemical sensors [34], all showing outstanding properties of these materials in terms of stability, chemical sensitivity and reproducibility.

2.5.1 Semiconductivity of porphyrins

Charge transport in organic semiconductors is dependent on $\pi-$bonding orbitals and quantum mechanical wave-function overlap. In disordered organic semiconductors, there is limited $\pi-$bonding overlapping between molecules and conduction of charge carriers (electrons or holes) is described by quantum mechanical tunneling [35]. Charge transport depends on the ability of the charge carriers to pass from one molecule to another [36]. Molecules consisting of several benzene rings merged along one bond are called *polycyclic aromates*.

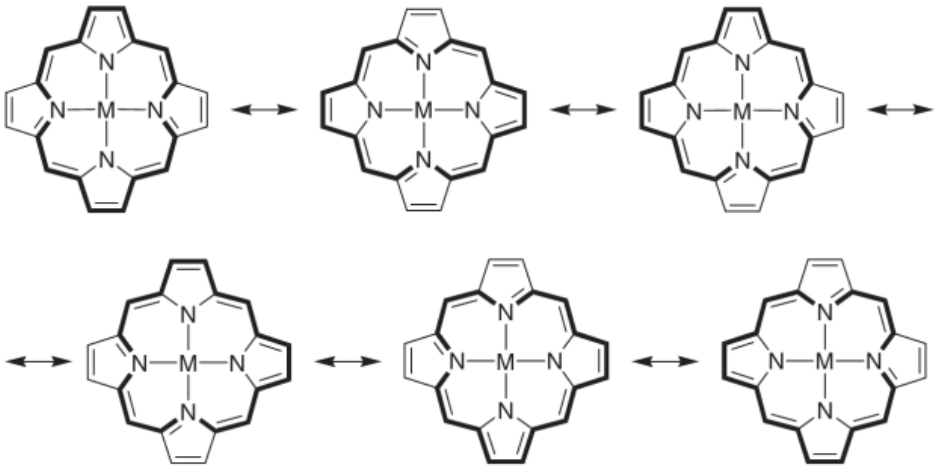

FIGURE 2.27: Electronic delocalization in the metalloporphyrin aromatic system [37, 38].

For these molecules the place of the double and single bonds is not uniquely determined, but has two distinct configurations with exactly the same energy. In these cases, resonance of the two forms causes a dislocation of the electrons; it is no longer possible to identify the place of the single and double bonds. A charge injected into a π molecular orbital can relatively easily migrate along the chain and, for limited conjugation lengths, macroscopic conduction is then made possible by further overlap of molecular orbits with neighboring molecules, causing so-called Davydov splitting of the molecular levels [26].

Porphyrins are a group of *heterocyclic macrocycle organic compounds*, composed of four modified pyrrole subunits interconnected at their carbon atoms. The porphyrin macrocycle has 26 (delocalized) π electrons in total, therefore by Huckel's rule it is aromatic, possessing $4n + 2$ π electrons ($n = 4$, for the shortest cyclic path). Thus porphyrin macrocycles are highly conjugated systems and consequently they typically have very intense absorption bands in the visible region. In *heterocyclic molecules* one or more

carbon atoms are replaced by an atom of other species, like *nitrogen* or *sulfur*. Because of their chemical valence, they possess more electron than carbon. In six-rings the additional electrons do not contribute to the $\pi-$system, but may be used for forming bonds to other atoms. In five-rings they help stabilizing the conjugation [39].

In case of metalloporphyrins the metal coordination modifies the π electrons' delocalization [38], thus in principle changing the electronic behavior of the molecules.

2.5.2 Vacuum deposition

Porphyrins may be deposited by spin-coating, drop casting and other solution-processed deposition techniques, up to deposition able to produce self organized thin films or single molecular crystals for molecular electronics application [40].

Both the morphology and molecular arrangement in organic semiconducting layers play significant roles in the performance of OFETs. In order to achieve a more efficient charge transport, ideally the organic molecules should pack along the current direction in the conducting channel. There is no doubt that, due to their perfect molecular arrangements, free of grain boundaries, and minimized charge traps, single crystal transistors should display higher performances than those of thin films. Hence, well-ordered, continuous films, especially crystalline films, are being seriously investigated for high performance OFET applications [41].

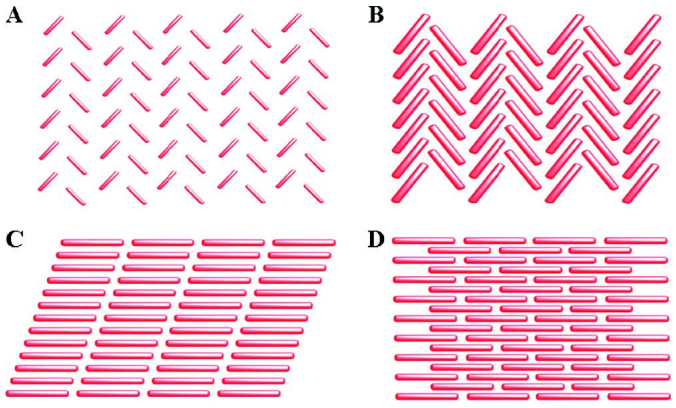

FIGURE 2.28: Molecular packing motifs in crystals. (A) Herringbone packing (face-to-edge) without $\pi - \pi$ overlap (face-to-face) between adjacent molecules (example: pentacene); (B) herringbone packing with $\pi - \pi$ overlap between adjacent molecules (example: rubrene); (C) lamellar motif, 1-D $\pi-$stacking (example: hexyl substituted naphthalene diimide); (D) lamellar motif, 2-D $\pi-$stacking. From [41].

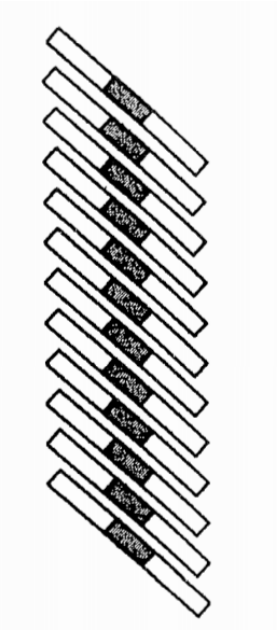

(A) Schematic representation of the tilted columnar stacking [33].

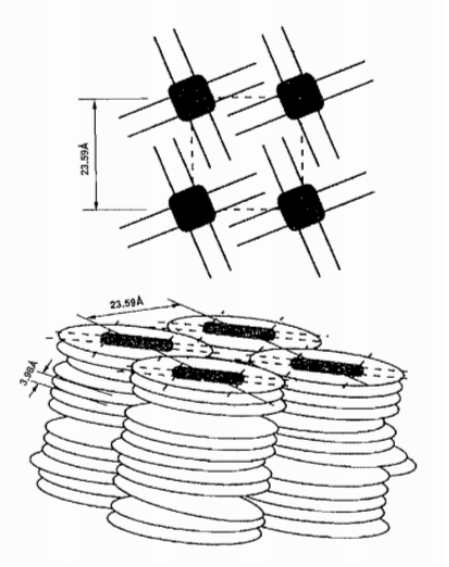

(B) Schematic representation of the columnar arrangement of discotic zinc n-decil ether octa-substitued porphyrin stacks [42].

FIGURE 2.29

Our approach took under examination the evaporation of porphyrins from a Organic Spintronics Knudsen cell in a Edwards thermal evaporator equipped with a turbomolecular pump. We chose evaporation in order to investigate a fast and cost effective deposition process oriented in a medium-large production (evaporation in principle allows the production of hundreds samples in the same time). With this approach, the following eventual implementation of the device as sensor would be easy given the large availability of samples in comparison to other solution deposition techniques, which allow low rate of samples fabrication.

Due to the difficulty in choosing a single porphyrin in a device oriented approach we preferred, in this preliminary work, to perform a screening of different porphyrins trying to highlight their behaviour under typical restrictions of fabrication processes. Following this approach we will show preliminary characterization and results over 5 different porphyrins (Figure 2.30).

As we highlighted molecular crystallization plays a fundamental role in the device performance, but a lot of deposition parameter and conditions have and effect on it. In particular crystallization in porphyrin thin films is influenced (as can be expected) by substrate temperature during deposition [43, 44], vacuum condition and eventual gas

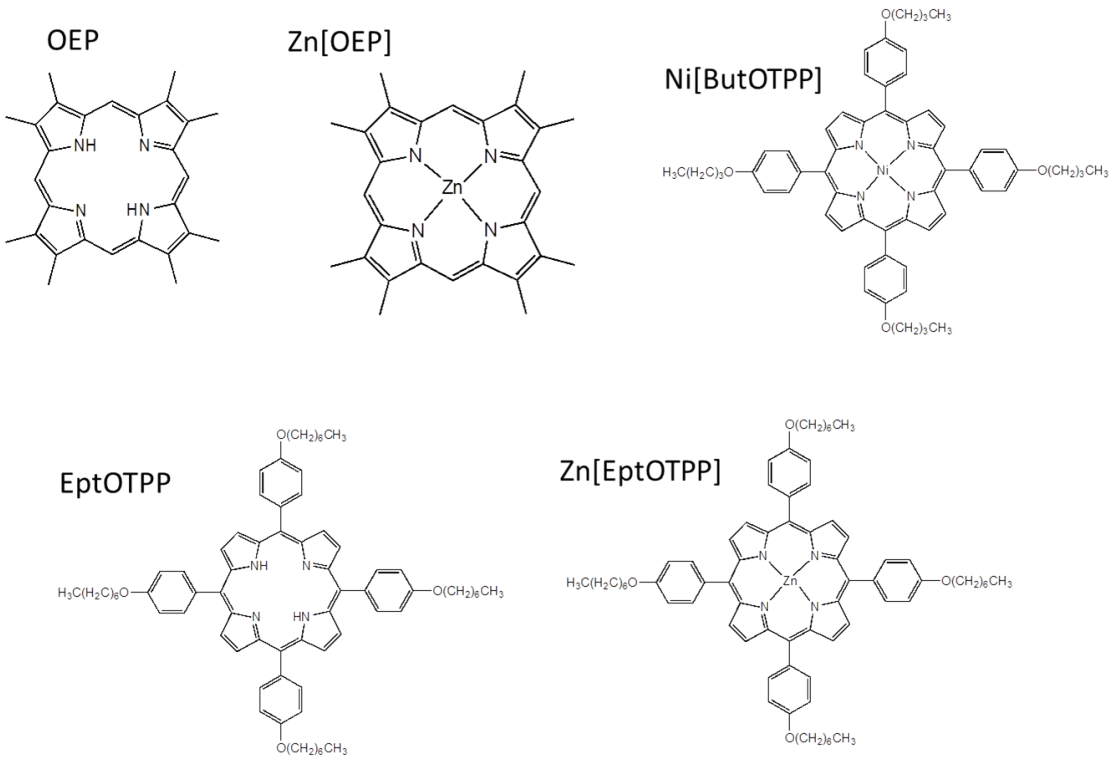

FIGURE 2.30: Structure of the porphyrins under investigation.

presence in the chamber [45]. Furthermore semiconductive properties are also non-linearly dependent on the thickness of the film [46].

We chose to evaporate porphyrins at room temperature in high vacuum with a chamber pressure of 10^{-6} torr. The evaporation temperature was found by observing thickness variations by means of a quartz thickness sensor (inside the chamber). The process, due to the lack of data on porphyrin evaporation, didn't allow us to monitor real thickness of the thin film during evaporation, and the thickness monitor was observed to detect evaporation and check a relative rate of evaporation. The porphyrins, evaporated in powder form, were supplied by Prof. Roberto Paolesse, Department of Chemical Science and Technology, University of Rome Tor Vergata. OEP and Zn[OEP] starting evaporation temperature was found at 275° C and was set at 280° C to obtain a suitable deposition rate, while Ni[ButOTPP], Zn[EptOTPP] and EptOTPP starting evaporation temperature was 375° C and was set at 380° C. From first observation thin film resulted uniform and preserved the typical color of the porphyrin powder, thus evaporation preserved the integrity of the porphyrins' chromophores. Low weight porphyrins (OEP and Zn[OEP]) adhesion was worst than in the case of higher weight porphyrins, and residual material in the quartz boat was still in powder form suggesting a sublimation, while higher weight porphyrins residual was melted thus suggesting an evaporation from liquid phase.

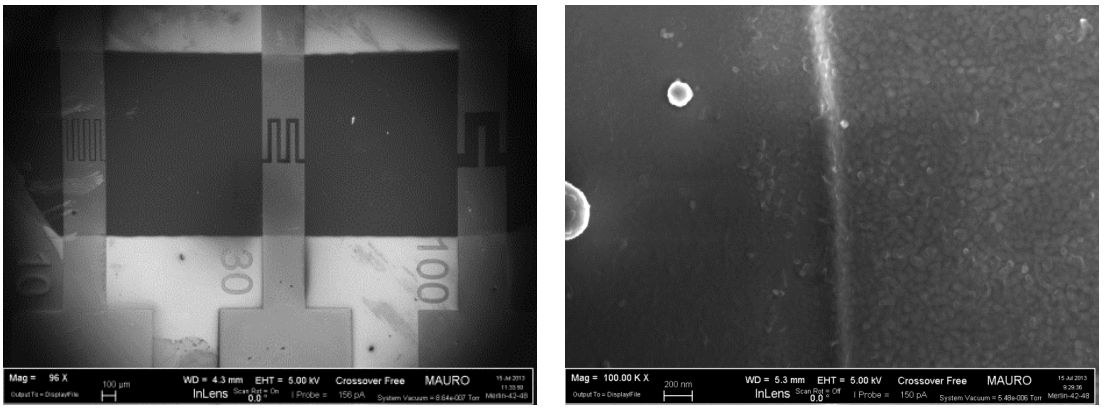

(A) (B)

FIGURE 2.31: SEM images at different magnification of Octa-Ethyl Porphyrin (OEP) layer on source and drain electrodes.

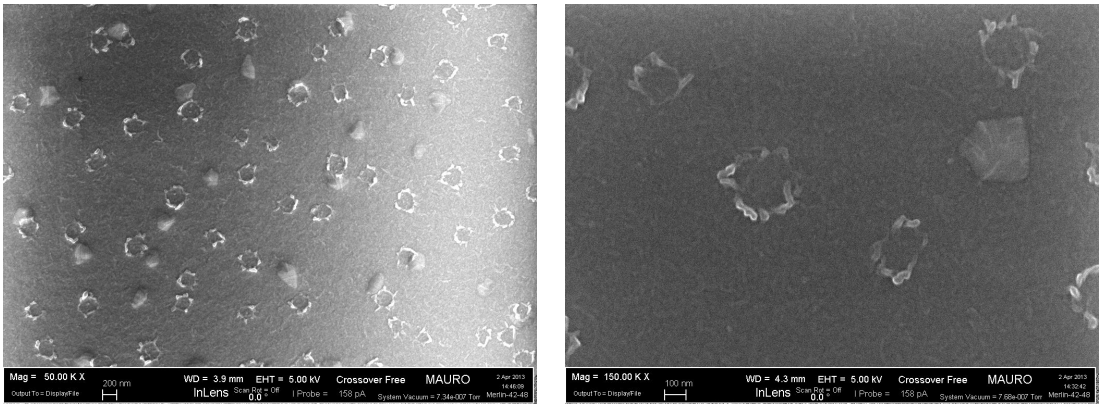

(A) (B)

FIGURE 2.32: SEM images at different magnification of Octa-Ethyl Porphyrin (OEP) layer morphology.

2.5.3 Morphological characterization

SEM characterization of porphyrin show compact thin film formation. In Figure 2.31 is visible the patterning with shadow mask on the previously patterned electrodes and the uniform covering of a step.

As evinced from Figures 2.32 and 2.33 the morphology is slightly different for different porphyrins.The typical porphyrin molecular stacking of Figure 2.29 seems to form the basic unity of the thin film. The stacks of molecules are far from forming an ordered array but tend to fill the available space deforming themselves. Some additional structures with high aspect ratio (long around 100 nm and lage 10 nm) emerge from the background.

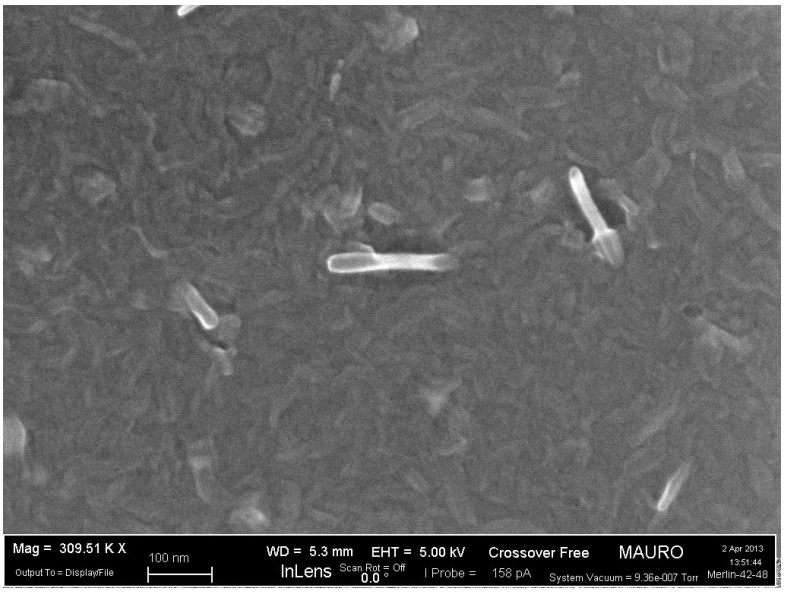

FIGURE 2.33: SEM image Zinc Octa-Ethyl Porphyrin (Zn[OEP]) layer morphology.

To investigate eventual crystal orientation on the porphyrin thin films we analyzed the samples with X-Ray Diffraction (XRD). The instrument used in this analysis is a PANalytical X'Pert 5000 X-ray diffractometer.

XRD is a powerful and commonly available technique for identifying the presence of crystalline phases. XRD patterns typically represent a spatial average over several mm^2 of area and few μm in depth. X-rays with λ between 0.5 and 2Å are impinged upon a sample. The diffracted X-rays are measured and 2θ, the angle between the X-ray source and detector (Figure 2.34). The diffraction can then be described by Bragg's law ($\lambda = 2d \sin\theta$), where d is the spacing between atomic or molecular planes within the sample. The relative intensity of a diffraction peak from a given set of planes can be determined by using the symmetry of the lattice and to calculate a structure factor.

Due to the difficulty to derive crystal structure from peaks position usually diffraction patterns are compared with patterns corresponding to well-known geometries. Also it is possible to simulate a diffraction pattern for a given crystal structure. In our case we can notice the presence of sharp diffraction peaks which indicate that the deposited layer has a well-ordered crystal structure. The substrate has been also analyzed in order to exclude his characteristic peaks. Unfortunately it is difficult to determine information on crystal structure because numerical calculation are needed to carry on the analysis [47].

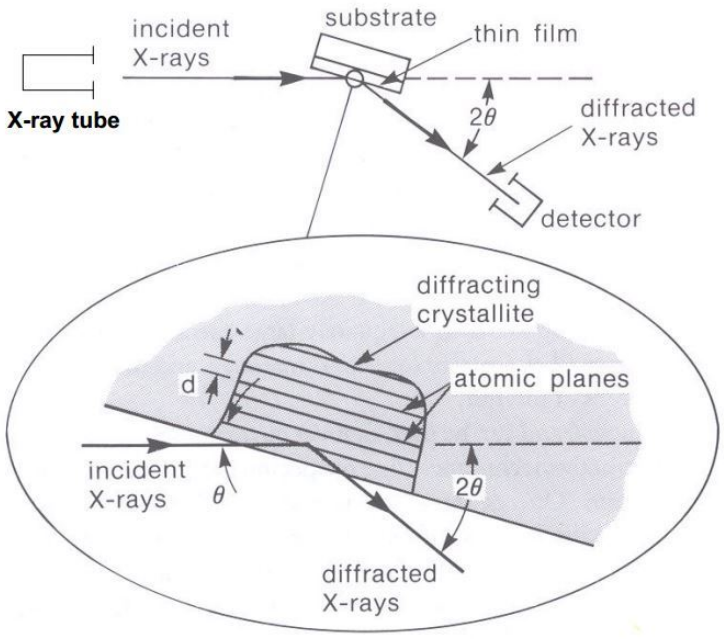

FIGURE 2.34: XRD working principle.

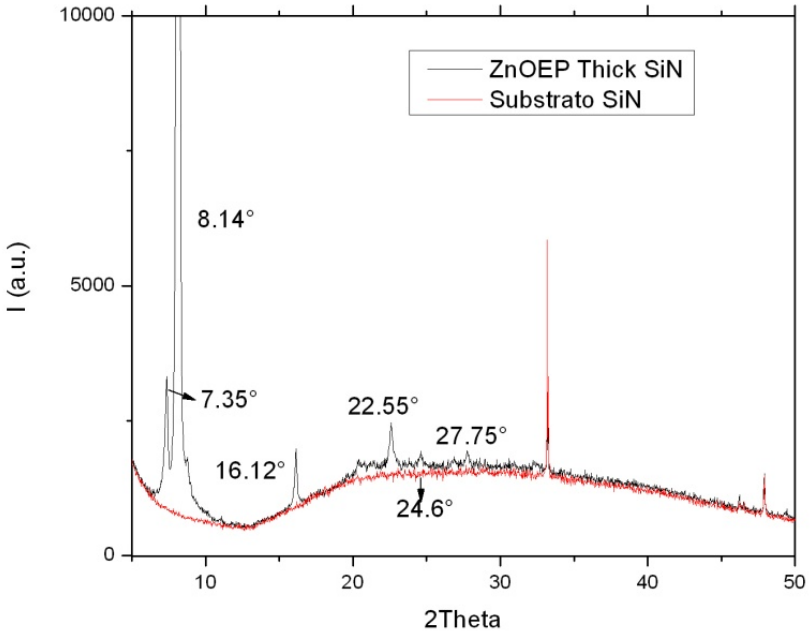

FIGURE 2.35: XRD spectrum of Zinc Octa-Ethyl Porphyrin (ZnOEP) thin film.

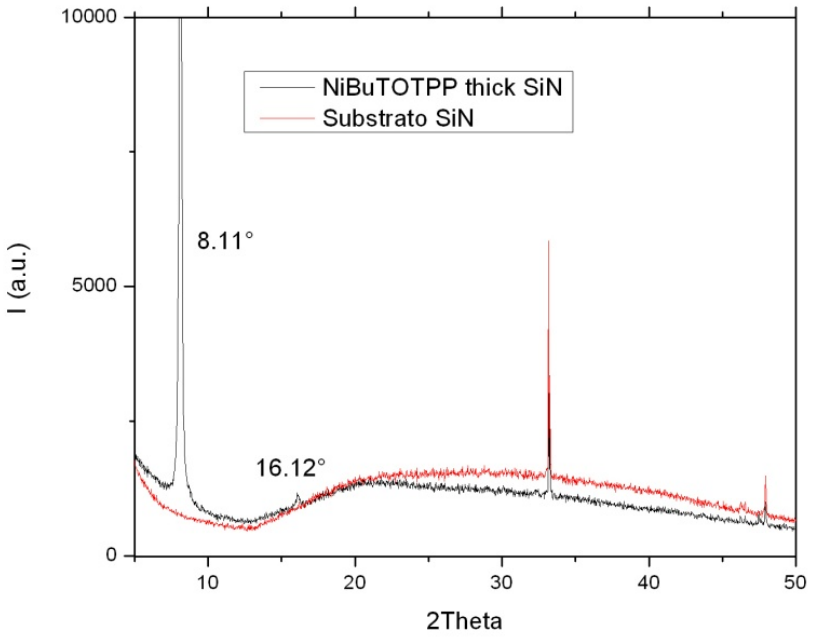

FIGURE 2.36: XRD spectrum of Nichel Tetraphenylporphyrin (Ni[ButOTPP]) thin film.

2.5.4 Electrical characterization

We analyzed our devices in order to investigate conductivity and field effect dependence of porphyrin thin films. The measurement set-up is shown in Figure 2.37. We used a aixPES of aixACCT Systems for the IV curve and a GW Instek GPS-4303 Laboratory DC power supply to apply the gate voltage.

The first consideration in that two porphyrins with the same structure but one with the coordinated metal and the other without, have completely different electronic behaviour: the porphyrins with metac behave as semiconductors while porphyrins without metal are insulators and no appreciable field effect was observed. In Figures 2.38 and 2.39 IV curves of OEP and Zn[OEP] are shown for comparison. We observed this different behaviour also for EptOTPP and Zn[EptOTPP].

We can also notice from Figure 2.39 the nonlinear shape of the curve which is due to the presence of a traps-based conduction mechanism also called **Poole–Frenkel effect** (see Appendix A). Notice also the appearance of this effect in Figures 2.40 and 2.41, which refer to samples only differing in channel length: when the channel length of the device increases more traps affect the conductivity.

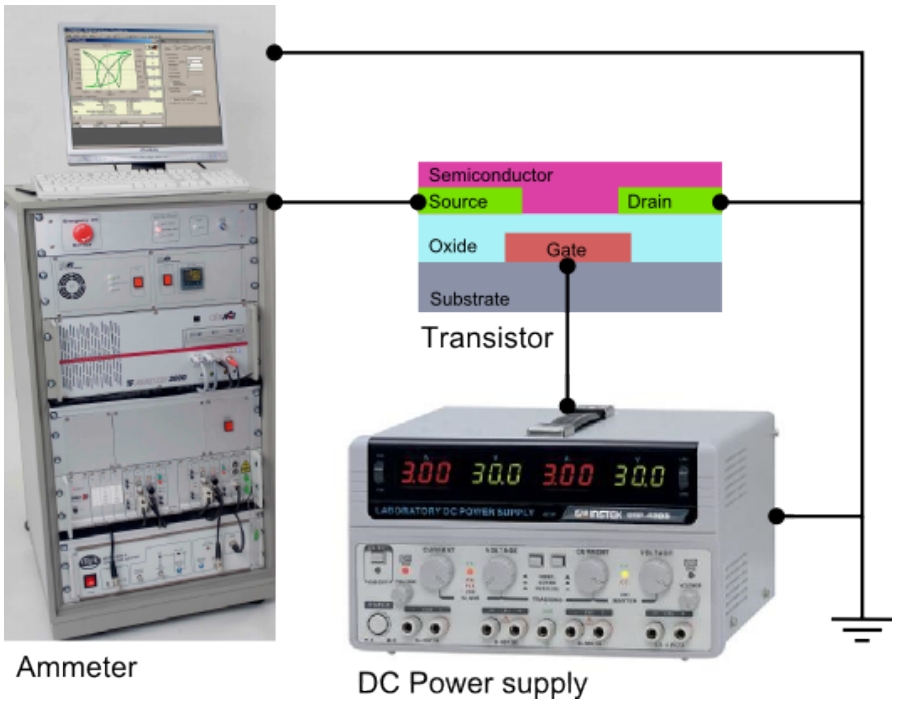

FIGURE 2.37: Electrical characterization measurement setup.

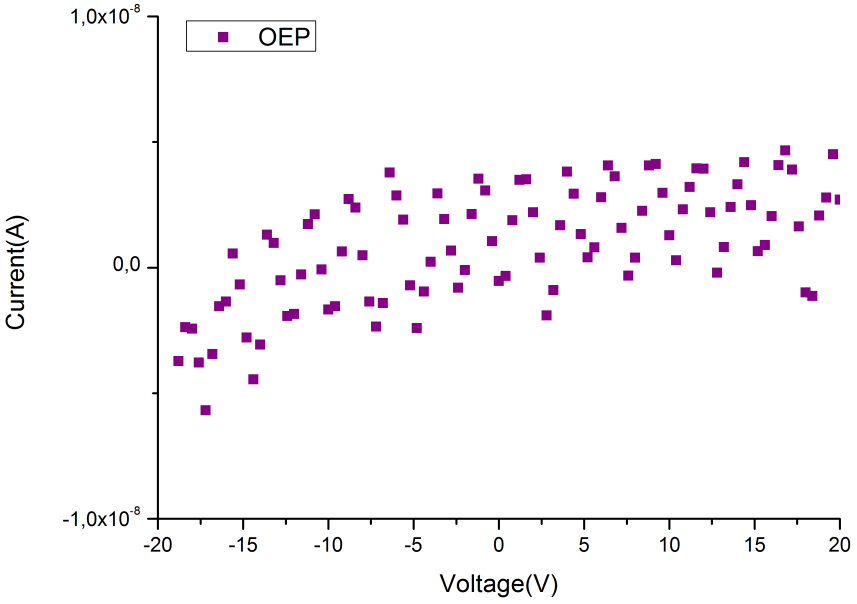

FIGURE 2.38: OEPIV IV curve.

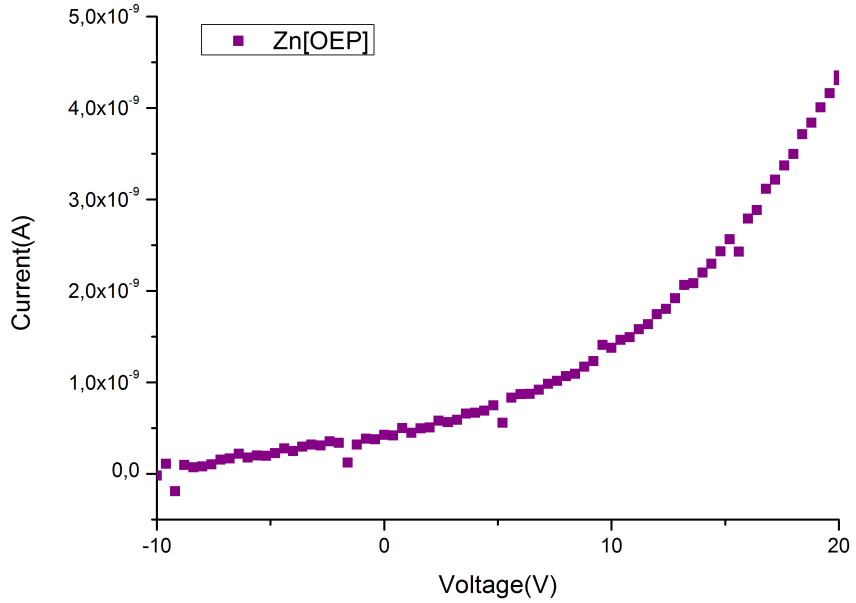

FIGURE 2.39: Zn[OEP] IV curve.

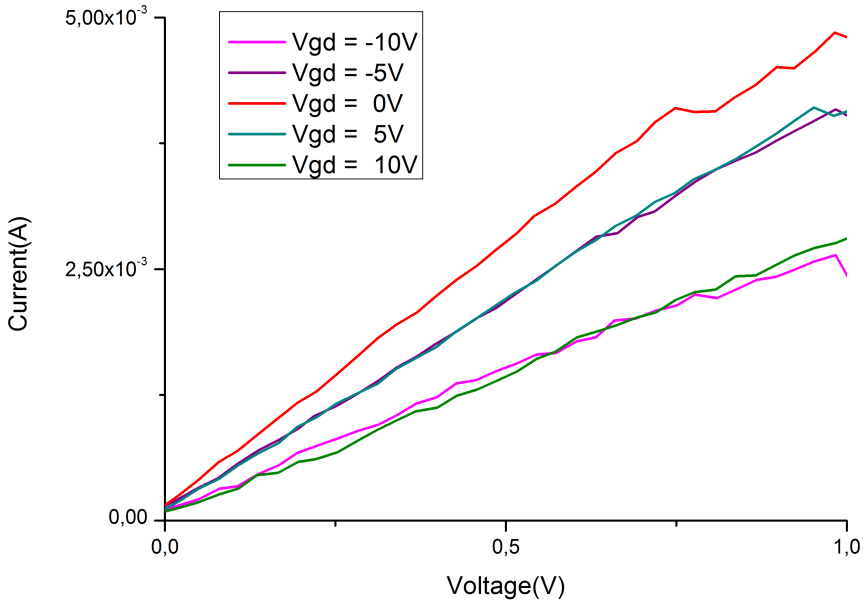

FIGURE 2.40: IV curve at different gate voltages of a Zn[EptOTPP] OTFT with channel 30 μm and Al_2O_3 gate oxide.

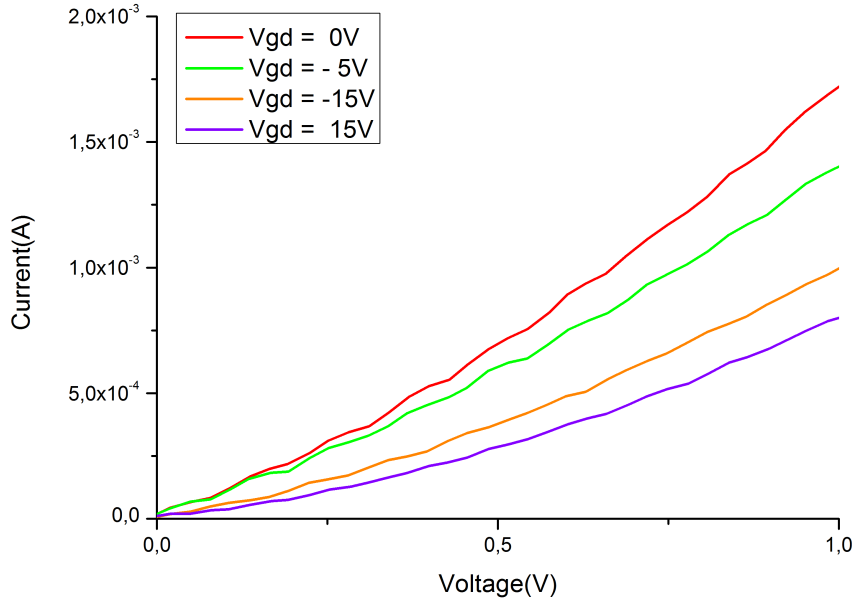

FIGURE 2.41: IV curve at different gate voltages of a Zn[EptOTPP] OTFT with channel 100 μm and Al_2O_3 gate oxide.

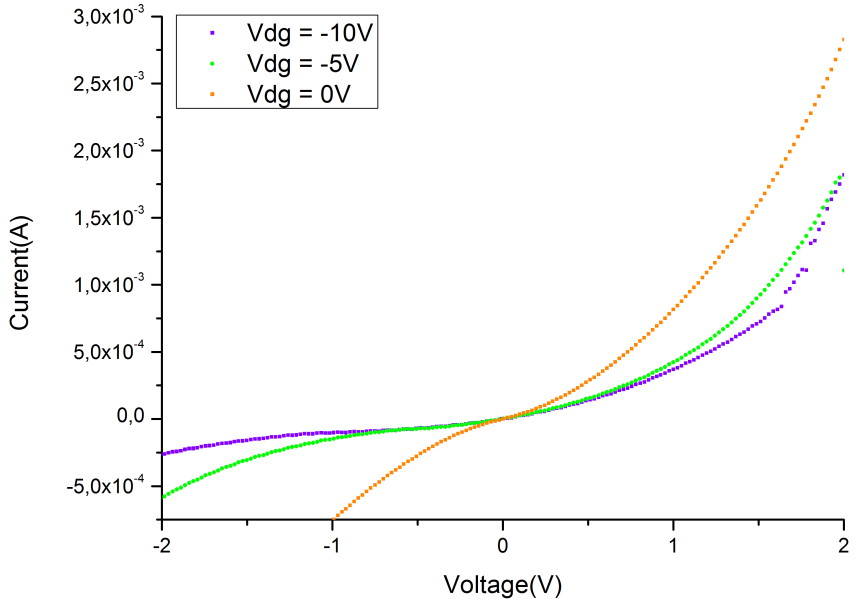

FIGURE 2.42: IV curve at different gate voltages of a Ni[ButOTPP] OTFT with channel 30 μm and Ta_2O_5 gate oxide.

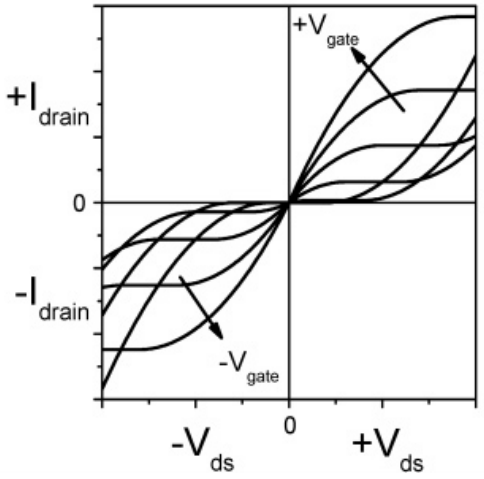

FIGURE 2.43: Calculated output characteristics of a field-effect transistor in the ambipolar regime with two separate channels of holes and electrons for positive (first quadrant) and for negative (third quadrant) Vg and Vds, respectively [49].

Figures 2.40, 2.41 and 2.42 refer to different samples all displaying the same field effect beaviour. The conductivity of the channel is lowered both for positive and negative voltage. This may suggest an **ambipolar operation** (both hole and electrons play a role in conductivity) [48] where, in the voltage ranges we were able to apply in our experimental setup, is possible to observe only a depletion operating mode. Unluckily this characterization is not enough to provide a full explanation of the observed effect. Similar results are present in literature for *copper phthalocyanine* (CuPc) and *fluorinated copper phthalocyanine* (FCuPc) based transistor (reported in [49]) where below a threshold gate voltage of 40 V the curves are similar to the reported in our work but above the threshold gate voltage the behaviour changes.

It is interesting to notice the almost perfect correspondence between the curves obtained with positive and negative gated device in Figure 2.40. From a scientific perspective, the ability to realize ambipolar transistors, which accumulate and conduct both holes and electrons, enables new ways to improve the understanding of the physics of these organic devices. In an ideal ambipolar transistor with just one semiconducting layer, the ambipolar regime is characterized by a hole and an electron accumulation layer next to the respective electrode that meet at some point within the transistor channel. There, oppositely charged carriers recombine. In electroluminescent materials, this leads to light emission from within the channel. The length of each channel and thus the meeting point and position of the recombination zone depend on the applied gate and source-drain voltage and mobility ratio. The potential of the transistor channel in the ambipolar regime can roughly be imagined as that of a saturated hole and electron channel in series, resulting in an s-shaped transition region (Figure 2.43) [50].

2.6 Organic layer: squarain dyes

In this section we will show preliminar result in the utilization of squarains as active layer of a OTFT device.

2.6.1 Squarain dyes

Squaraines are such a class of dyes which are well-known for their strong absorption and emission in the long-wavelength region accompanied by a remarkable (photo)stability under ambient conditions [51, 52]. They were successfully used as gas sensors [53], in bioimaging probes [54], for photodynamic therapy, in nonlinear optics [55], and many further applications. In particular, squaraine dyes were applied as highly potent p-type semiconductor materials in xerographic photoconductors [56] and organic solar cells [57]. However, their applicability in OTFT devices has yet been explored rather sporadically. Squaraine dyes OTFTs were designed for near-infrared light-emitting ambipolar organic field-effect transistors [58], nanowire transistors [59], and NIR detectors [60]. OTFTs were obtained for the first two cases by spin coating, while in the latter well-aligned and single crystalline squaraine nanowires were used as the active layer of transistor devices. Others approach for thin film fabrication are using solution-shearing techniques and vacuum evaporation [61].

2.6.2 Experimental results: morphology and electrical characterization

Our first test has been drop casting of squareins solutions in dichloromethane (DCM) on previously patterned substrates and thus characterize the OTFT. Squaraines under test were synthesized by the Chemical Deparment of the Torino University; their chemical structure is shown in Figure 2.45. For simplicity we will refer to them as **squarain A** and **squarain B**. Drop casted samples, after 20 minute from the deposition, were annealed at 120° for 4 minutes. SEM characterizations (Figure 2.46) of both squaraines show a disordered discontinuous structure slightly different for different molecules.

The device was then characterized with the measurement set-up shown in Figure 2.37. The very low conductivity of the samples led to reach very high source-drain voltages for the characterization. Result are shown in Figure 2.47 an lead to suppose an ambipolar behaviour. From our point of view we preferred investigate other deposition techniques in order to reach a higher conductivity (better crystallization) of the molecular thin film.

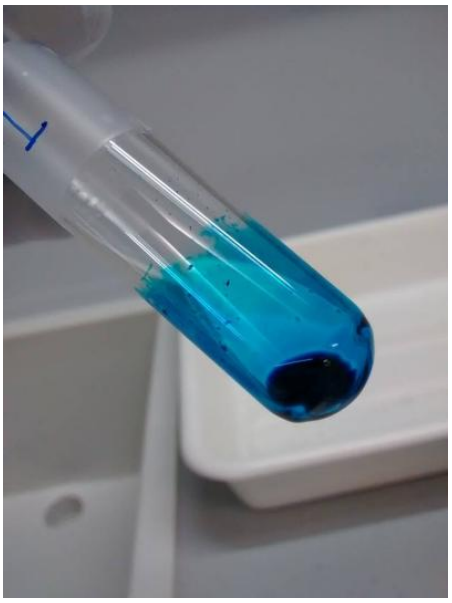

FIGURE 2.44: Squaraine dye A in a test tube.

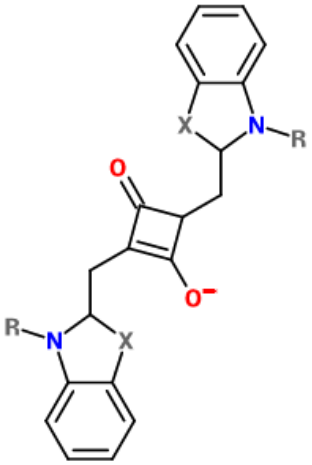

(A) Squaraine dye **A** with $X = C(CH_3)_2$ and $R = C_{12}H_{25}$

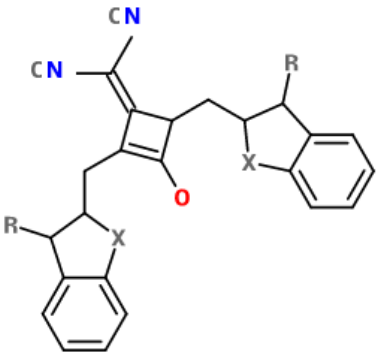

(B) Squaraine dye **B** with $X = S$ and $R = C_{16}H_{33}$

FIGURE 2.45: Chemical structure of the chosen squaraines.

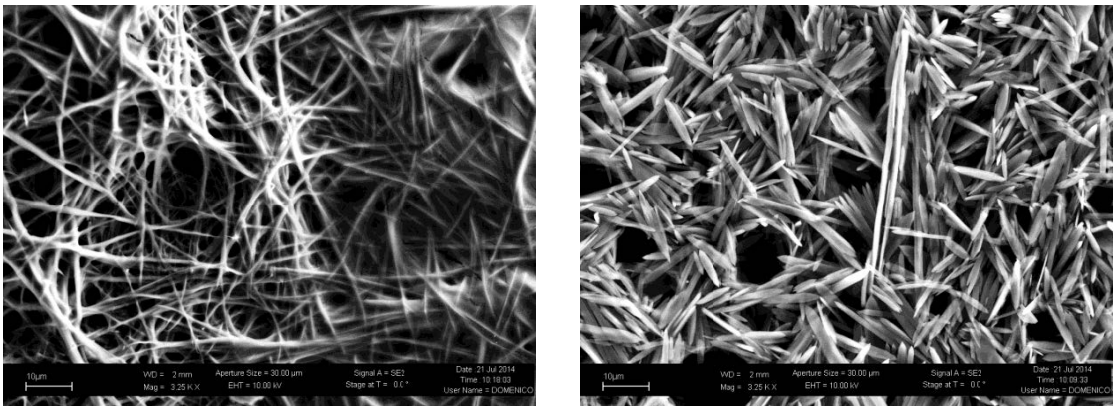

(A) Squarain A (B) Squarain B

FIGURE 2.46: SEM images of squaraines morphology.

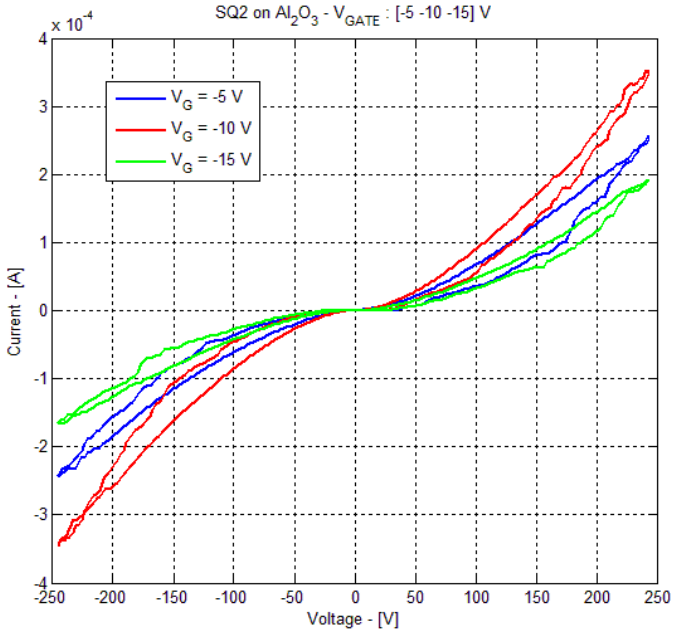

FIGURE 2.47: Drop-casted **squaraine A** I-V curves.

The second test was oriented to find suitable condition for thermal evaporation of squarains on previously patterned substrates. Since thermal evaporation process of these particular squaraines could damage the molecules, a heat decomposition mass curve was needed. For this reason we performed a Thermal Gravimetric Analysis (TGA). TGA is a method of thermal analysis in which changes in physical and chemical properties of materials are measured as a function of increasing temperature (with constant heating rate). TGA can provide information about physical phenomena, such as second order phase transitions, including vaporization, sublimation, absorption, adsorption, and

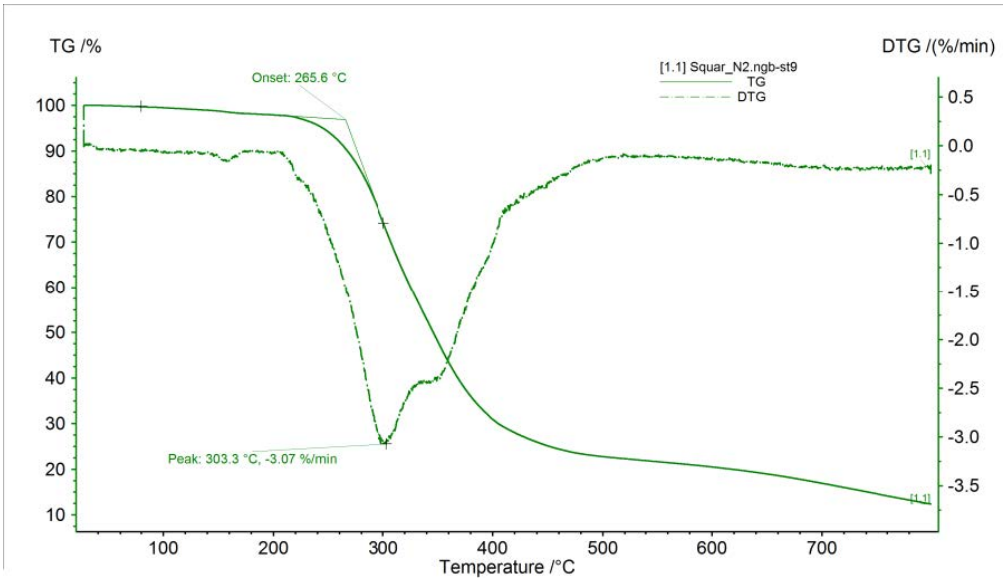

FIGURE 2.48: TGA on squaraine A.

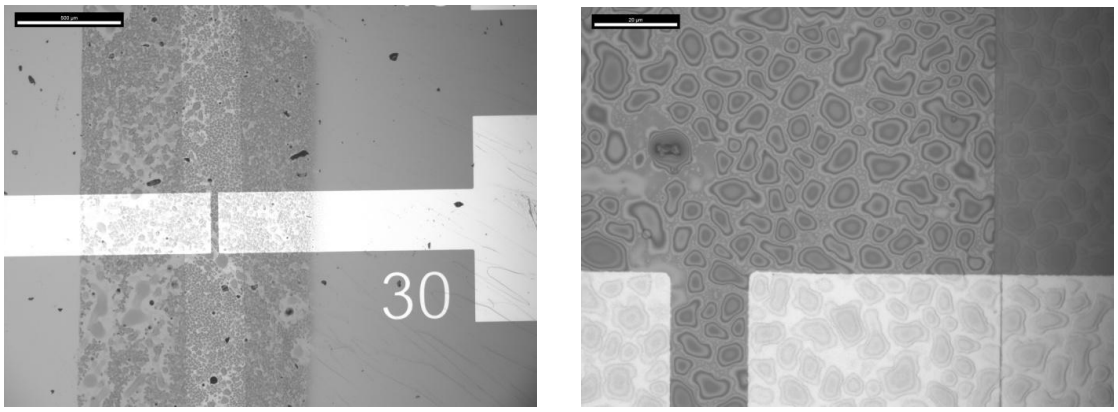

(A) (B)

FIGURE 2.49: Optical microscope images at different magnification of evaporated squaraine A thin film morphology on patterned electrodes.

desorption [62]. The differential curve (DTG) in Figure 2.48 shows a peak at 303° C representing material degradation so evaporation temperature was set at 280° C. We evaporated the squaraine from a quartz boat of a Knudsen cell in a Edwards thermal evaporator in high vacuum (10^{-6} torr) on room temperature substrate.

Optical microscope images of evaporated thin film patterned with shadow mask shows a non-uniform structure. It is clearly visible from Figure 2.49 the presence of domains with varying thickness with a hills and valleys profile in the range of 5-10 μm.

Also evaporated thin films show very low conductivity (Figure 2.50) which is probably

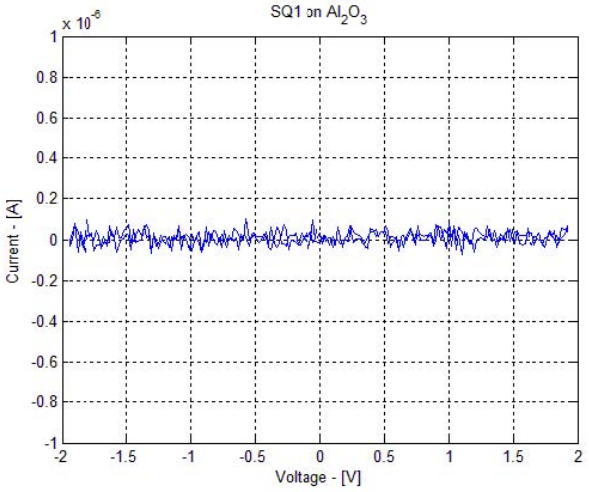

FIGURE 2.50: Evaporated **squaraine A** I-V curves.

caused by the lack of uniformity and not sufficient crystal formation. Further investigation could be focused on changing deposition parameters, such as substrate temperature and pressure in chamber, in order to improve crystallinity, and, as in the case of porphyrins, perform XRD characterization for each fabrication parameter variation.

2.7 Organic layer: PEDOT:PSS

We carried on investigations on PEDOT:PSS as active layer of the device in order to easily test the inorganic part of the process fabrication of OTFTs. In particular we were interested in the ability of the device to show a field effect and avoid the presence of leakage currents and other fabrication defects. Commercial PEDOT:PSS was used for his easy implementation and stable characteristics. Results of this screening are included here only to highlight the OTFT capabilities. See [63] for more details on PEDOT:PSS.

Poly(3,4-ethylenedioxythiophene), or PEDOT [64], is an electro-chemically stable conjugated polymer initially developed to give a soluble conducting polymer that lacked the presence of undesired couplings within the polymer backbone. Prepared using standard oxidative chemical or electrochemical polymerization methods, PEDOT was initially found to be an insoluble polymer, yet exhibited some very interesting properties. In addition to a very high conductivity (ca. 300 S/cm), PEDOT was found to be almost transparent in thin films and showed a very high stability in the oxidized state [65]. The solubility problem was subsequently circumvented by using a water-soluble polyelectrolyte, *poly(styrene sulfonic acid)* (PSS), as the charge-balancing dopant during polymerization to yield PEDOT:PSS. This combination resulted in a water-soluble polyelectrolyte system with good film forming properties, high conductivity (ca. 10 S/cm),

high visible light transmissivity, and excellent stability [66]. Films of PEDOT:PSS can be heated in air at 100 ° C for over 1000 h with only a minimal change in conductivity. Although initially used as an antistatic coating in photographic films from AGFA, several new applications have been implemented over the past few years (e.g., electrode material in capacitors, material for through-hole plating of printed circuit boards) [67].

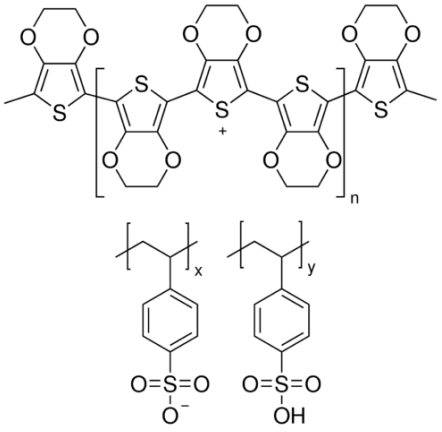

FIGURE 2.51: Chemical structure of the PEDOT:PSS blend.

In OTFTs, the active layer is composed of an undoped semiconductor that forms a conductive channel at the interface with the dielectric when an electrical field is applied. It was therefore unexpected to observe a field effect in devices comprising an intrinsic conducting polymer like PEDOT:PSS as the active layer [68].

The change of resistance of the conducting channel on variations of the external field was different from semiconductor-based OTFTs: the current change on the applied electrical field was slow, in the order of minutes. Additionally the field effect disappears completely when the temperature is decreased from room temperature by only 10° C [69]. This led to the assumption that ion diffusion motion within the PEDOT:PSS channel is responsible for the observed I_{DS} modulation. It has been also observed a pronounced dependence of the field effect on the humidity level [70]: in dry atmosphere almost no change of I_{DS} on the gate voltage was found. An electrochemical mechanism was proposed to explain the electric field dependence including the dedoping of PEDOT in the presence of water.

A different explanation was proposed by Hsu et al.[71]. Dedoping of PEDOT was ruled out as the total number of injected ions from out of the gate into the PEDOT:PSS channel was too low to explain the observed current decrease. Instead a model was favored assuming a change of percolation paths caused by rendered ion positions. A small fraction removal of mediated hopping states near the Fermi level on charge transport

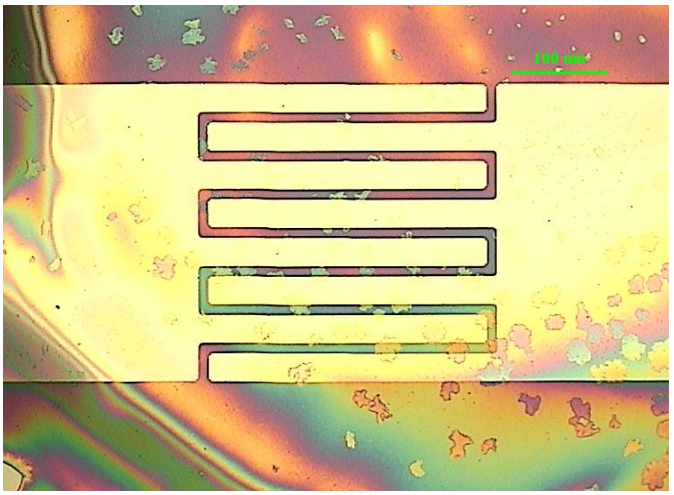

FIGURE 2.52: OFET with PEDOT:PSS active layer: drop casted PEDOT:PSS - H_2O solution on chip surface.

paths causes carriers to hop over longer distance to conduct current and therefore I_{DS} is reduced.

Technological exploitation of PEDOT:PSS as active layer for stand-alone transistors is not easy due to the slow dynamics, but could be investigated as chemical sensor. In fact the physical properties of conducting polymers strongly depend on their doping levels. Fortunately, the doping levels of conducting polymers can be easily changed by chemical reactions with many analytes at room temperature, and this provides a simple technique to detect the analytes [72]. Most of the conducting polymers are doped/undoped by redox reactions; therefore, their doping level can be altered by transferring electrons from or to the analytes. Electron transferring can cause the changes in resistance and work function of the sensing material. The backbones of common conducting polymers are built up with aromatic rings, which are easy to attach various grafts through electrophilic substitutions. By introducing different substituents, or copolymerizing with different monomers, it is facile to adjust both the chemical and physical properties of conducting polymers; these adjustments are useful for promoting selectivity of sensors, and convenient in fabricating sensor arrays.

2.7.1 Experimental results: fabrication process and electrical characterization

We started with Sigma-Aldrich Poly(3,4-ethylenedioxythiophene)-poly(styrenesulfonate) blend 1.3 wt % in H_2O with PEDOT content at 0.5 wt. % and PSS content at 0.8 wt. %. In order to obtain a suitable polymer concentration for drop casting method, the commercial solution was further diluited at 5% in DI water. A drop of this solution was

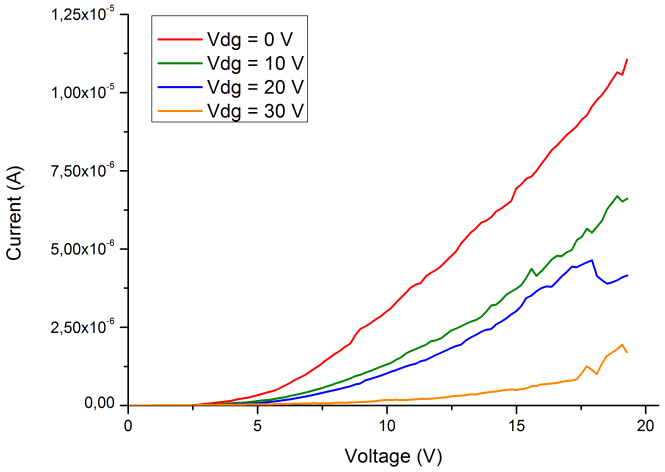

FIGURE 2.53: I-V curves of a OTFT with PEDOT:PSS active layer and 10 μm channel length: different gate voltages show different conductivity.

then casted on patterned silver electrodes of the one-mask substrate (see Section 2.3.1) made of Si n++ as gate and silicon oxide dielectric. The solution was then baked for 10 min at 100° C resulting in a continuous, transparent-bluish thin film (Figure 2.52).

As expected, the application of a field to the PEDOT:PSS channel of the OTFT has reduced the conductivity. The behaviour of this class of devices is not easy to characterize because of the long lasting dynamics, as highlighted above. The curves in Figure 2.53 are obtained by waiting 5 minutes after the application of different fields.

As shown, OTFT architecture is a useful and robust tool to exploit also properties of polymer semiconductors. Further investigation could be oriented in find suitable condition to test the device as sensor in a controlled enviroment, fully characterize the time constant of the I-V curve after field application and possibly exploit it as parameter.

Chapter 3

Microfludic platform for diffusion test: a microgravity experiment

3.1 Controlled release drug delivery systems

Conventional dosage forms, such as oral delivery and injection, are the predominant routes for drug administration. However, these types of dosages are not easily able to control the rate of drug delivery or the target area of the drug and are often associated with an immediate or rapid drug release. Consequently, the initial concentration of the drug in the body peaks above the level of toxicity and then gradually diminishes over time to an ineffective level. The pharmacodynamics and efficacy of treatments have indeed been demonstrated to be related to the frequency, time and duration of drug administration [73]. In recent years, increasingly sophisticated and potent drugs have been developed by the biotech industry. For many of these new protein-based and DNA-based compounds, the therapeutic concentration range is often small, toxicity is observed for concentration spikes, or the therapeutic concentration range varies with time, which renders traditional methods of drug delivery ineffective [74]. An immense amount of interest has been increasingly placed on controlled release drug delivery systems to maintain the therapeutic efficacy of these drugs. There are a number of mechanisms that can provide such controlled release of drugs, including transdermal patches, implants, bioadhesive systems, and microencapsulation [75, 76].

3.2 Principles of micro and nanofluidics

Nanofluidics is intrinsically associated with nanoscale phenomena which are primarily caused by the confinement of the fluid at the molecular scale. At this level, the integral

balance of different forces creates a complex system which significantly affects the transport of fluids with respect to the macroscale. While at the macroscopic level volume properties and inertial forces play a dominant role over the fluid transport, as the size of the system decreases, fluid-surfaces interaction becomes more and more important. When the system shrinks to the nanometer scale (frequently assumed to be below 300 nm), the fluidics is dominated by viscous forces. Under these conditions, the Reynolds number (Re) is typically less than 10^2 and the convective flow is laminar [77] with mixing accomplished only through diffusion. In general, the transport of molecules at the nanoscale is dominated by their interaction with the boundaries.

The transport of solutes and solvent through nanochannels or nanopores depends on three factors. First, the presence of **external forces**, such as an electrical potential gradient or a pressure gradient: these forces are needed to drive transport along the nanochannel. Second, the presence of various **colloidal forces**, which lead to a variation in the solute concentration across the nanochannel. Third, the presence of **friction forces** between the wall and the solvent, and also between the wall and the solute molecules. The solute and solvent transport fluxes can be deduced from knowledge of these three forces.

As almost all wall materials (in particular dielectric materials) carry **surface charge**, there is often an electrostatic force that repels ions with the same charge as the wall (**co-ions**) and attracts ions with the opposite charge (**counter-ions**). However, all the counter-ions do not end up against the wall: instead, the homogenizing action of the thermal (Brownian) motion results in an **electrical double layer** (EDL) adjacent to the wall, with an increased concentration of counter-ions and a decreased concentration of co-ions (Figure 3.1).

The EDL consists of a Stern layer and a diffuse layer, which are occupied by immobile counterions and mobile ions, respectively. By using the basic Stern model, some studies have shown that the immobile Stern layer plays a crucial role in the ion transport phenomena in nanochannels [78]. Its thickness depends on the ionic strength of the solution. The differential surface charge is monotonically screened departing from a surface and can drop to zero in the bulk of the fluid. The electric surface potential measured at the boundary between the Stern and diffusive layers is called **zeta-potential (or ζ-potential)**.

In point of fact, many surfaces in nanochannel systems are charged due to the chemical nature of their materials, their fabrication process, or the functional modification of their surfaces. **Crystalline silicon** is one of the most common substrates used in nanofluidics. Silicon develops an amorphous silica layer $(SiO_2)_n$ under ambient conditions [79]. A wet environment hydrophilizes the silica surface to different extents by introducing silanol

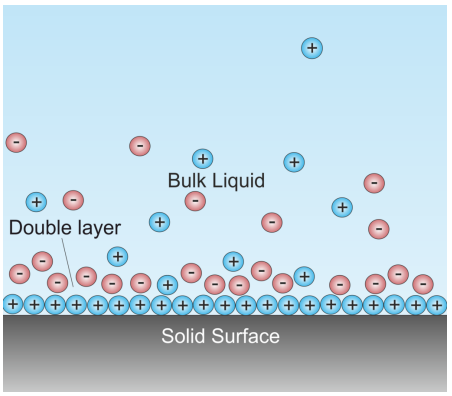

FIGURE 3.1: Schematic of double layer in a liquid at contact with a negatively-charged solid.

groups, which get ionized in water based buffers by experiencing deprotonation:

$$Si - OH \rightarrow Si - O^{-} + H^{+}.$$

Therefore, **the charge density on a silica surface is a function of the environment, including pH or salt concentration**, and can range from -1 to -10 μC/cm^2 [80].

As nanochannel size decreases, the EDLs formed on opposite surfaces start to overlap. This causes the occurrence of electrostatic phenomena which affect the transport of charged molecules (Figure 3.2). Among these, the electrostatic exclusion of molecules is one of the most important [81]: when the EDL overlaps in a nanochannel, ions presenting the same charge as the surface are electrostatically excluded from the passage, while counter-ions can freely diffuse cross the nanochannels. Several studies investigated this phenomena due to its potential application in ion separation and filtration [82].

It is possible to control solute transport in nanochannels by modulating the electrostatic interactions between the solute molecules and the walls (similar to the methods used to control solvent transport). One example of this approach applied to **controlling the flow of ionic solutes include changing the pH to control transport through a membrane** [84] and changing the electrolyte strength to gain control over the transport properties of a specifically engineered nanochannel [85].

Another important phenomena influencing molecular transport at the nanoscale is **electroosmosis**. Electroosmosis represents the motion of a fluid along the charged surface of a channel driven by an applied electrical field. More specifically, the electrical field drags counter ions in the EDL together with associated water molecules, causing a net electroosmotic flow along the nanochannel.

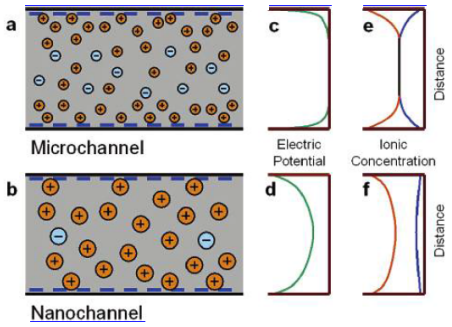

FIGURE 3.2: Surface charge effects in microchannels and nanochannels. **a.** In a microchannel, the Debye length is typically much smaller than the channel dimensions and most of the solution in the channel is neutral. **b.** In a nanochannel, the solution is charged when the Debye length is larger than the channel dimensions. **c.** The electric potential in the microchannel decays rapidly to its bulk value in a distance of the order of the Debye length. **d.** The electric potential even at the center of the nanochannel is influenced by the surface charge and is not equal to the bulk potential. **e.** The concentration of cations (orange) and anions (blue) in the microchannel is equal to the bulk concentration. **f.** In a nanochannel, the counterion concentration (orange) is much higher than the coion concentration (blue). From [83].

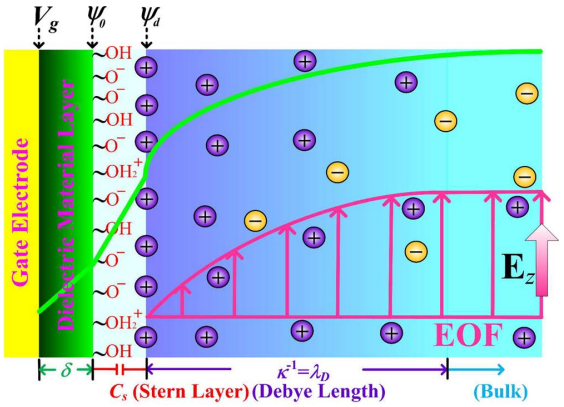

FIGURE 3.3: Schematic representation of the modulation of the zeta potential ψ_d and electroosmotic flow (EOF) by a field effect transistor. Four major regions under consideration are identified: the dielectric material layer of thickness δ, the immobile Stern layer with surface capacitance C_s, the diffuse layer of Debye length λ_D, and the bulk solution. V_g is the gate potential imposed on the gate electrode, and ψ_0 is the surface potential stemming from the association and dissociation reactions of functional groups on the nanochannel wall. The green line illustrates the variation of the electric potential. From [78].

Another promising and versatile technique involves the use of electrodes on the exterior of a nanochannel with thin walls (made of native silica) to **actively vary the electrostatic potential** at the wall to control the electrokinetic transport of charged species [83].

These class of devices are called **nanofluidic transistor** based on a metal-oxide-solution system 3.4. These devices are similar to field-effect transistors: a gate voltage modulates the concentration of ions and molecules in a channel and controls the ionic conductance. Unlike the FET, where the only function of the gate voltage is to control electrical conductance, the nanofluidic transistor could be used to tune the ionic environment as well as to control the transport and concentrations of ions or particular charged biomolecular species. Since biomolecules are typically multivalent, gating control may be expected to be more effective for controlling biomolecules than for monovalent ions.

3.3 A microscopic simulation of nanoscopic dynamics

Nanochannels design for a controlled drug release is not an easy task: classical mathematical models for diffusion do not work properly and it is necessary to improve the direct understanding of the underlying physics by direct observation. By improving the knowledge on the physics and chemistry of diffusion in nanochannels, it is possible to develop a model that will make much easier to design delivery devices for any drug, and speed up the development of these technologies.

The drugs of interest are usually tiny (1-6 nm) and too small to be seen or tracked with microscopes. Usually fluorescence and electrical measurements are applied [83] but the dynamics inside a channel can only be predicted and simulated. Much larger particles (around 1 μm) instead can be seen and tracked.

Two aspects play a major role in how particles move and diffuse through channels:

- the relative size of particles and the channel
- electric charge interactions between the particles and channel.

We used functionalized (charged) micrometric fluorescent polystyrene particles to mimic ions, furthermore we designed and fabricated a MEMS-like structure consisting of microchannels to mimic nanochannels. By scaling up the system we expect to be able to mimic the complex dynamics of diffusion described above by using only concentration gradient and pH as driving forces. A fluorescent microscope will be used to characterize the system, tracking the motion and speed of particles considering the influence of charge gradients in affecting the their movement.

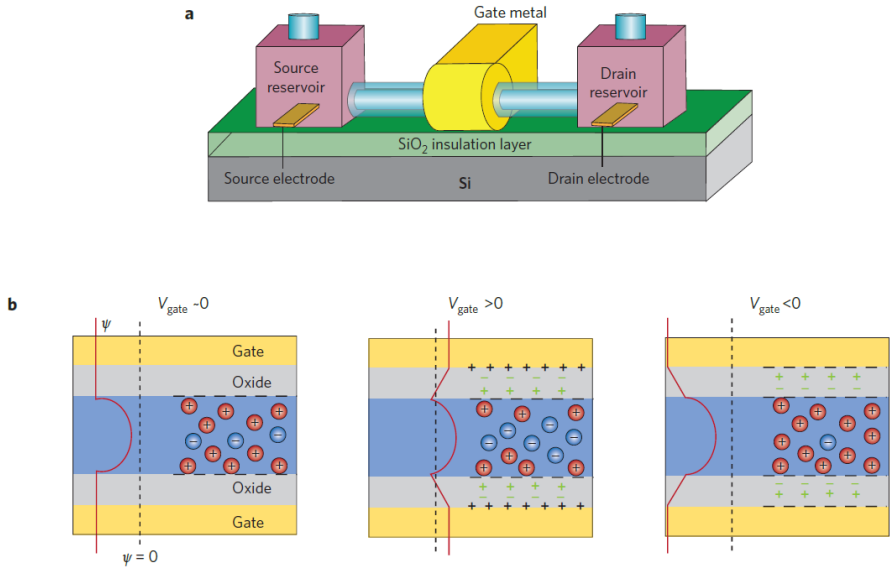

FIGURE 3.4: The nanofluidic transistor. **a.** Schematic of a nanofluidic field-effect transistor. In a conventional field-effect transistor, the current flowing through the channel between the source and drain electrodes is driven by the voltage applied across these electrodes, and it can be controlled by applying a voltage to the gate electrode. The voltage on the gate electrode essentially modulates the type (that is, electrons or holes) and number of charge carriers in the semiconductor channel below it. In a nanofluidic transistor the flow through a nanochannel can be driven by pressure, an applied electric field or a concentration difference. By applying a bias voltage between the gate electrode and the solution, the wall potential can be changed, modulating the counter-ionic charge in the solution. **b.** When the gate voltage is zero, the electrostatic potential ψ (red line) does not vary with position in the oxide, but it decays exponentially to a minimum in the centre of the channel (shown in blue; ψ is positive to the left of the line showing $\psi = 0$). In this example the walls have a negative surface charge (black symbols) and the electrical double layers at each wall almost meet in the centre of the channel, so the channel is mostly occupied by counter-ions (which are positive in this system). For positive gate voltage the electrostatic potential at the wall becomes less negative, effectively decreasing the transport rate of the positive ions (or even strongly increasing the transport rate negative ions for a high gate voltage). This results in a positive wall because the applied voltage polarizes the oxide layer, which can be represented by a positive surface charge (green symbols) on one side and a negative surface charge on the other, with ψ decaying linearly within the oxide layer. For negative gate voltage the electrostatic potential at the wall becomes more negative, increasing both the number and transport rate of positive ions. From [86].

Scaling-up the system means also take under consideration mass-dependent forces: since molecular mass in nanochannels doesn't feel gravity as a micrometric particle, the results of the experiment could be slighty different from reality. Gravity in fact represents a constant interfering force during slow diffusive dynamics and could affect other important forces. For this reason, if preliminary characterization with the designed experimental set-up will be promising, the experiment will be carried on also on the International Space Station U.S. National Laboratory. Methodist Hospital Research Institute at Houston, BioServe Space Technologies at the University of Colorado at Boulder and NASA Glenn Research Center in Cleveland, Ohio, will be also involved in this study.

3.4 MEMS technology and nanofluidics

Once shown the ideas upon nanofluidics is based we will provide here a description of a MEMS-based process relating the fabrication of a nanochannel in silicon membrane. This description is provided here to give the idea of a nanofluidic device whose working principle is under investigation by our scaled-up chip.

A large percentage of the literature revolves around two primary techniques.

The first is the use of an embedded and patterned sacrificial layer which is embedded into a second material which will constitute the walls of the nanochannel [87, 88].

The second primary technique, and perhaps the most attractive for the production of nanochannel drug delivery implants, is to create a nanoscale trench in the substrate surface and then use one of the previously described bonding techniques to cap the trench with a second substrate and form the channel [89].

We report here an example of the first family of devices.
The original method pioneered by Chu et al. [87] consists of two basic steps: (1) surface micromachining of nanochannels in a thin film on the top of a silicon wafer, and (2) forming the nanopore membrane by etching away the bulk of the silicon wafer underneath the thin-film structure. The overall fabrication process is shown schematically in Figure 3.5.

The fabrication sequence begins by lithographically patterning and etching trenches into the silicon surface (Figure 3.5 A). After stripping the resist and cleaning the substrate, a sacrificial oxide is grown across the wafer surface (Figure 3.5 B). Next polysilicon is deposited onto the oxide covered trenches to a thickness exceeding that of the trench depth (Figure 3.5 C). The surface is then planarized using a plasma etch process such that the excess thickness of the polysilicon and the layer of oxide on the top of the trench

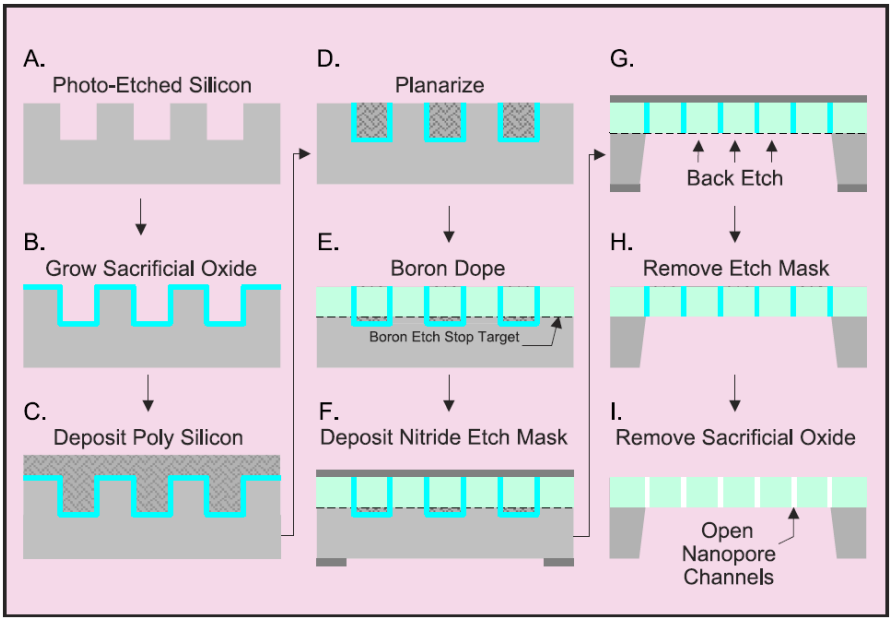

FIGURE 3.5: Schematic of key steps in silicon nanopore membrane fabrication process [88].

is removed (Figure 3.5 D). This planarization is followed by boron doping of the crystal lattice of the bulk silicon and polysilicon (Figure 3.5 E). The boron doping has the effect of dramatically reducing the etch rate of this region of the silicon and polysilicon substrate in KOH. Silicon nitride is then deposited on both sides to act as a masking layer (Figure 3.5 F) during KOH etching of the back side bulk silicon to release the membrane (Figure 3.5 G). The boron doped silicon and polysilicon act as an etch stop due to the differential etch rate. The silicon nitride etch mask is then removed (Figure 3.5 H) followed by removal of the sacrificial oxide (Figure 3.5 I), both of which can be etched in hydrofluoric acid with almost no silicon or polysilicon removal, to complete the process. Experimental results of drug diffusion through this device are shown in Figure 3.6. The solid line has been obtained by simply combining the first Fick's law with the mass conservation principle and multiplying the mass flux times the total nominal pore area.

To achieve a further insight in the mechanisms involved in nanochannel diffusion, the experimental phenomena can be described in mathematical terms, thus yielding a dynamic model. Such a model is outlined in Appendix B.

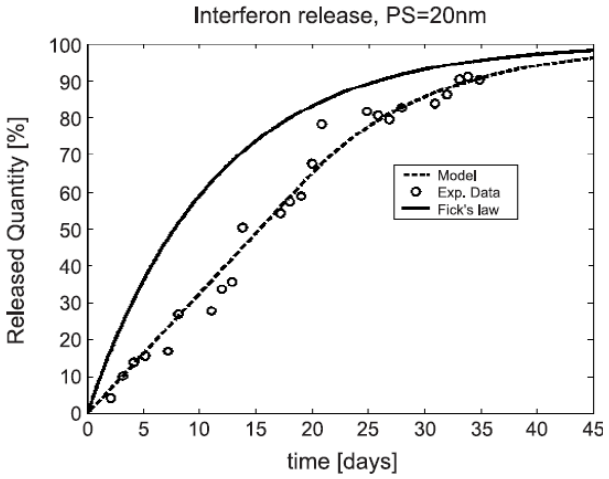

FIGURE 3.6: In vitro interferon diffusion through nanopore membrane (20 nm pore size) under sink conditions: experimental data, Fick's law prediction, and model-based simulation [88].

3.5 A scaled-up nanofluidic model

3.5.1 Chip design

We designed and fabricated the experimental setup for monitoring the diffusion of micrometric fluorescent polystyrene particles as follows.
We realized a **micromachined silicon chip**, with etched patterns on the surface to be bonded to a pyrex glass. The patterns consisted of two chambers (*source* and *sink reservoirs*) connected with an array of **microchannels** of different width and depth with rectangular cross section. The inlets and outlets were placed on the bottom side of the silicon chip, because previously fabricated chip with inlets and outlets on the side manifest a cross contamination due to the capillary action of water around the chip along the silicon/pyrex interface.

A CAD project of the chip is shown in Figure 3.7 while the process flow is represented in Figure 3.10. The process involved three lithographic steps (three masks) and front-back alignment of the geometries.
The photomasks patterns were generated with the software PhoeniX CleWin and transferred onto a high-quality chrome - soda lime mask (ML&C GmbH, Germany).

- Mask 1: **inlets and outlets**. Low resolution geometries (100 μm)
- Mask 2: **microchannels**. High resolution geometries (1 μm)
- Mask 3: **source and sink reservoirs**. Low resolution geometries (100 μm)

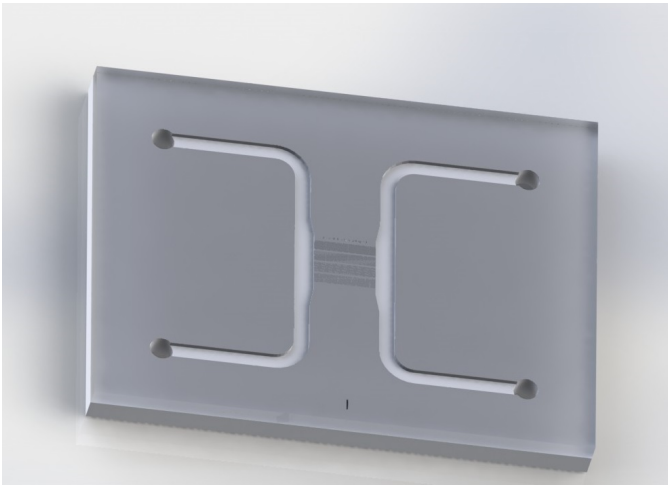

FIGURE 3.7: 3D CAD representation of the drug delivery test platform

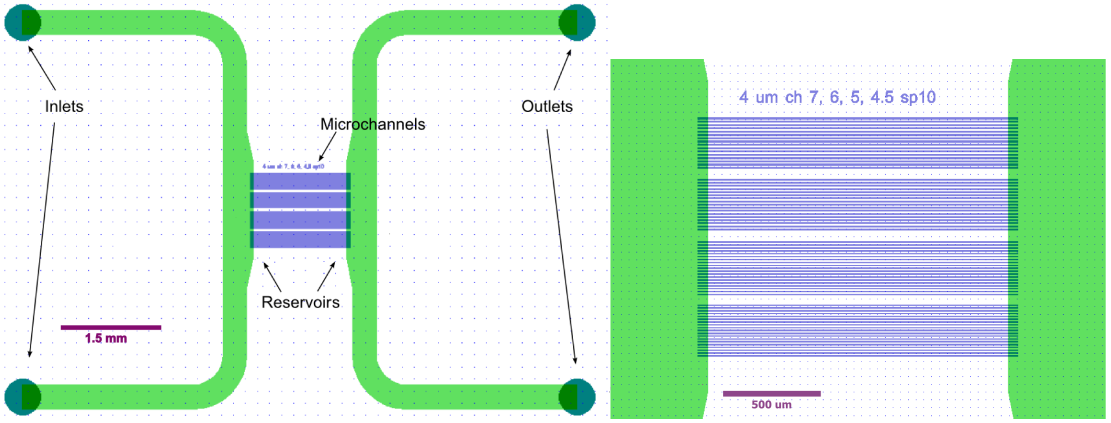

(A) (B)

FIGURE 3.8: CAD chip design and microchannels detail.

The three photolithographic steps are represented in Figure 3.18 with different colors. The entire chip width is 1 cm, the source and sink reservoirs are 500 μm wide and the inlets and oulets have 600 μm diameter.
The microchannels range from 2 to 10 μm width with 10 μm interdistance and are 1.5 mm long for one class of samples and 5 mm long for another class of samples (see the full reproduction of the mask in Figure 3.9).

3.5.2 Fabrication process

The scheme of the fabrication process is represented in Figure 3.10. The first step is the **inlets and oulets fabrication**. We performed a DRIE implementing the Bosch process (see Chapter 1.7). The depth of excavation in this step was 500 μm (the wafer

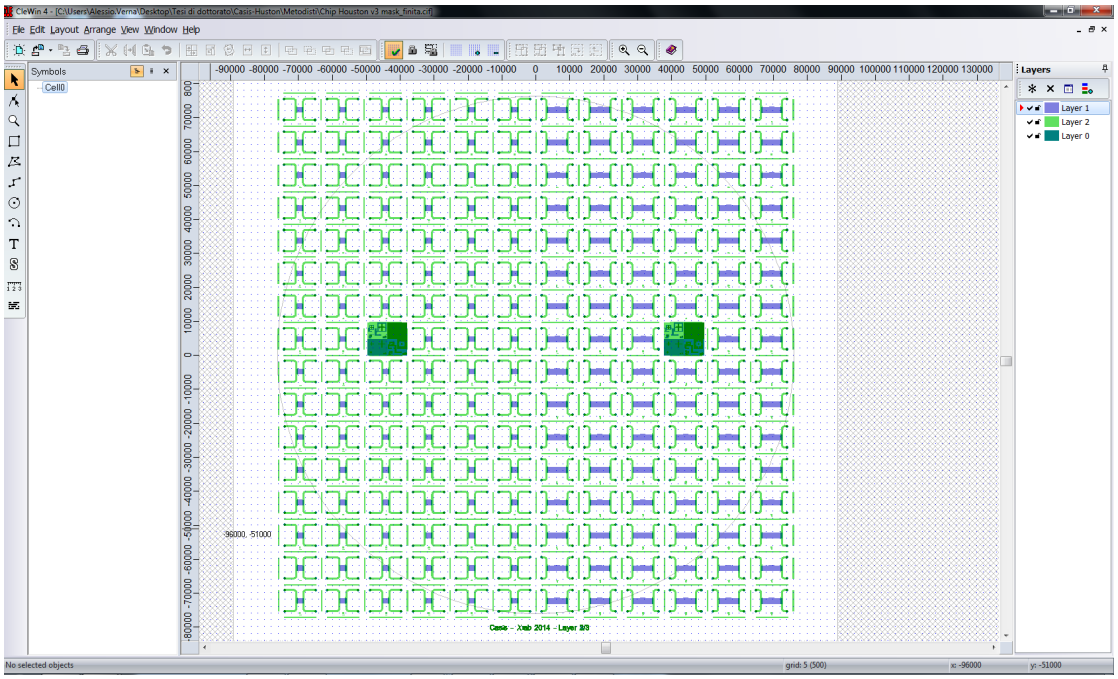

FIGURE 3.9: CAD for masks realization. Entire mask pattern is shown.

was 625 μm thick); to obtain such a deep etching a suitable mask was needed. For this purpose we chose to utilize oxidized wafer (with 2 μm of oxide) patterned with a thick photoresist (spin-coated Microchemicals AZ 9260, 7 μm thick).

Before resist application, double side polished wafers were dehydratated at 150° for 5 min, cooled with a jet of N_2 gas and spin-coated with HMDS. After exposure and development the oxide on the patterned side of the wafer was etched in BOE 7:1 for 25 min (with etch rate of 80 nm/min); the opposite side was protected from etchant with dicing tape.

DRIE parameters were previously calibrated in order to obtain a suitable selectivity in respect to the chosen masks and perform a successful process.
As we discussed before the CCP (plate) power is employed to vary the substrate potential, whilst the ICP (coil) power is the higher power and is used to generate the plasma. ICP power, CCP power, gas flow rate, chamber pressure and etch/deposition time are the controlling parameters and can affect the resulting profile, the etch rate and the selectivity.

Bosch process parameters:

- Etch step: SF_6 with flow rate at 100 sccm, CCP power at 11 W, ICP power at 1500 W. Step duration: 7 seconds.

- Deposition step: C_4F_8 with flow rate at 50 sccm, CCP power at 10 W, ICP power at 1500 W. Step duration: 4 seconds.

For both step temperature was set at 20°, with baking Helium at 10 sccm, and chamber pressure was set at 20 mtorr. Obtained etch rate was 5 μm/min. After DRIE a piraña cleaning was performed. Then the oxide on the opposite side of the wafer was removed, again with BOE.

For the next photolithographic step involving **microchannels fabrication** few consideration are necessary.
Photoresist is a good masking material for the DRIE of silicon, if only shallow features are required and the etching is performed at room temperature. The low temperatures involved in the cryogenic DRIE process set new requirements for masking materials because common photoresist are subjected to cracking. Usually hard masks are used, but the necessity of further deposition/etching steps can affect the resolution. Thus a special photoresist was used: Microchemicals AZ 701 MiR, which is a thermally stable (softening point $> 130°$ C), high resolution photoresist optimized for dry etching of sub-μm structures.
Before photoresist spin coating, wafer were again dehydratated and spin-coated with HMDS. Exposition of photoresist for this step needed a special equipment, the front-back alignment feature of the mask aligner. After the photolithographic step, microchannels were created with Cryo process:

- SF_6 with flow rate at 60 sccm, O_2 with flow rate at 6 sccm, CCP power at 5 W, ICP power at 900 W. Temperature was set at -120° C, with baking Helium at 10 sccm, and chamber pressure was set at 10 mtorr. Obtained etch rate was 3.5 μm/min.

We fabricated two set of samples: one with channels 15 μm deep and another with channels 30 μm deep.

For the next step, after a piraña cleaning, the wafers were then spin-coated with Microchemicals AZ 9260 photoresist for the **source and sink reservoirs patterning**. After exposure and development, wafers were then etched again using the Bosch process with the same parameters used before. The needed etching depth for this step was around 125 μm, after that the geometries on the top side meet the holes in the back side of the wafer and the circuit results complete. This step is particularly difficult because when a hole is formed the backing Helium passes through them in the chamber with detrimental effects: the process temperature rises (because the refrigerant capability depends on

FIGURE 3.10: Process flow of drug delivery test platform: **a.** Patterning the inlets and outlets on the back side of the oxideized wafer with thick photoresist. **b.** Wet etching of silicon oxide in BOE solution. **c.** DRIE dry etching of silicon with Bosch process. **d.** Patterning of microchannels with thin photoresist on the front side. **e.** DRIE dry etching of silicon with Cryo process. **f.** Patterning the source and sink reservoirs with thick photoresist. **g.** Anodic bonding.

Helium presence under the wafer) and the plasma changes chemistry with resulting photoresist degradation and lost of selectivity. To overcome this difficulty we kept observing the Helium pressure stopping the process when the indicated value started to lower.

To seal the top side escavated geometries, fabricated wafers have been then permanently bonded with borosilicate glass (Pyrex) using anodic bonding. This step has been performed by *Rockwood Wafer Reclaim-* France. The Pyrex wafer was 500 μm thick and has been bonded at 350° C and 500 V.

3.5.3 Improvements from previous versions of the chip

A previous version of the chip was fabricated with one side process, with inlets and outlets on the side. This setup gave problems because the colloidal particles tend to migrate from one side of the chip to the opposite by capillary action, and the apertures were difficult to seal. The etching was done with KOH on 100 silicon thus obtaining a 54.7° angle of the wall of both chambers and channels thus creating a mirror effect during microscope characterization. Furthermore, in the second layout of the chip, reservoirs

were designed longer to prevent evaporation of solvent during the slow diffusion dynamics and to prevent bubble formation during the filling procedure.

3.6 Experimental

The experimental setup is oriented in characterize diffusion dynamics of **charged fluorescent microspheres** having different surface functionalization in different pH solutions at **constant concentration**.

These microspheres columbic-interact with each other and with the walls of the channels, which are electrically charged too. The electrostatic repulsion between the spheres leads to a boosted diffusion. The electrostatic repulsion between the spheres and the walls of the channel can lead to a **gating effect**: the spheres cannot enter the channels. The electrostatic attraction between the spheres and the walls of the channels can lead to **sticking effect**: the spheres stick to the walls of the channel, preventing other spheres from passing through the channel. The electrical charge of the walls and of the spheres can be modulated acting on the **pH of the solution**: the spheres are, in fact, functionalized with a certain chemical group (either carboxylic, or amminic, or sulphate) which is linked to a different electrical charge (or, better, to a different zeta potential) according to the ionic strength of the solution in which they are submerged.
The pH variation and the concentration gradient hence are the driving forces for microspheres diffusion through microchannels.

3.6.1 Microspheres zeta-potential

As we previously discussed, zeta potential is the potential difference between the dispersion medium and the stationary layer of fluid attached to the dispersed particle. According to general colloid chemistry principles, an electrostatically stabilized dispersion system typically loses stability when the magnitude (i.e. absolute value) of the zeta potential decreases to less than approximately 30 mV [90]. As a result, there will be some region surrounding the condition of zero zeta potential (i.e. **the isoelectric point**, or IEP) for which the system is not stable. Within this unstable region, the particles may agglomerate.

We determined the pH conditions of the isoelectric point using a **zeta potential analyzer**. The used equipment was *HORIBA SZ-100 nanoPartica system*.

Basically a zeta potential measurement works as follows. The sample is located in a transparent cell equipped with two electrodes. A laser is used to provide a light source

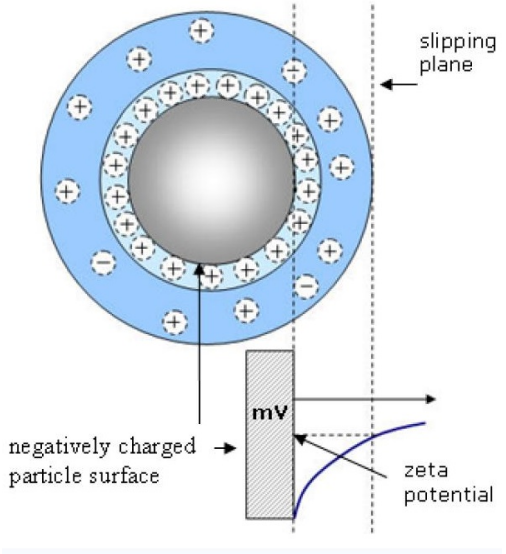

FIGURE 3.11: Zeta-potential of a negatively charged particle. From [91].

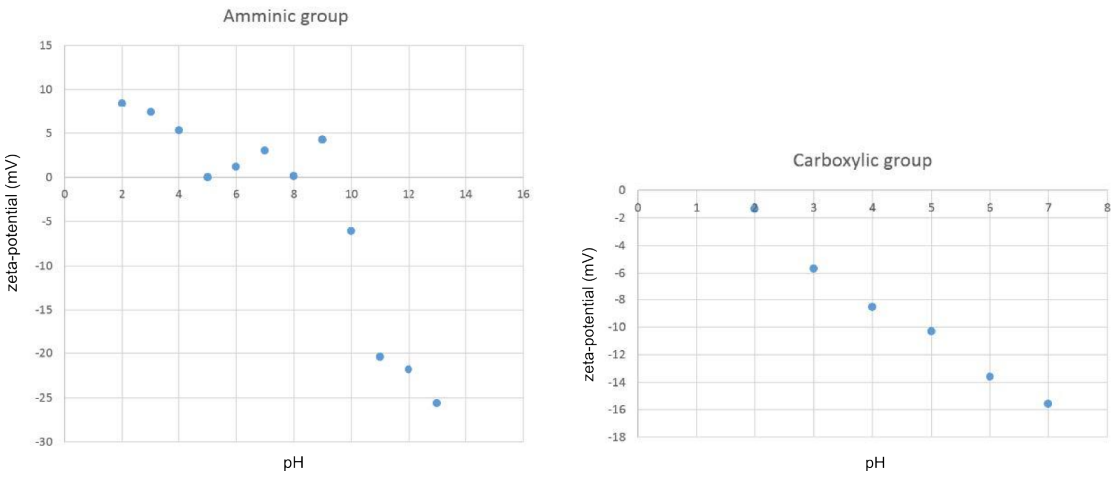

(A) (B)

FIGURE 3.12: Zeta potential vs pH of Amine-Modified and Carboxyl-Modified Microspheres.

both to illuminate the particles within the sample and reference beam. The incident laser beam passes through the centre of the sample cell, and the scattered light at a fixed angle is detected. When an electric field is applied to the cell, any particles moving through the measurement volume will cause the intensity of light detected to fluctuate with a frequency proportional to the particle speed and this information is passed to a digital signal processor and then to a computer.

In Figure 3.12 we show the measurements of the zeta potential vs pH both for the spheres ammino-functionalized and for the spheres carbox-functionalized. The general trend is

quite evident, despite all the uncertainties: zeta potential decreases if the solution gets more basic. The isoelectric point of the ammino-spheres is probably around 6 while the isoelectric point of the carbox-spheres is a probably less than 2.

3.6.2 Experiment setup

The core idea is making use of two different solutions: one containing a **fixed concentration of microspheres** and another devoid of them. Filling procedure comprises three steps. In the first step we loaded the sink reservoir with the solution devoid of spheres, taking particular care that the solution completely fills all the reservoir and the micro channels, but not the source reservoir.
In the second step we filled the source reservoir with the solution rich in spheres, and the final step is sealing the inlets and outlets as fast as possible to prevent evaporation and start the acquisition under microscope. Sealing has been preformed with common insulating tape.

We prepared solutions having different pH (ranging from 1 to 13). We obtained acid solutions by adding HCl and basic solutions by adding NaOH to DI water (having pH 7). The pH variation, in fact, varies the zeta potential of the spheres and hence the magnitude of the electrostatic interaction (among themselves and with the channels' walls). For a certain pH the zeta potential of the spheres vanishes (the isoelectric point) with reciprocal columbic interactions obtaining pure diffusive behaviour. Also the concentration of spheres in the source reservoir influences the diffusion speed: higher concentration of spheres are gives more electrostatic repulsion and a faster motion.

We used a solution with concentration of $8 \cdot 10^{-4}$ spheres/μl in water (or water and HCl, or water and NaOH).

We made use of the following surface-modified polystyrene microspheres supplied by *Life Technologies - Thermo Fisher Scientific*:

- F8823 FluoSpheres Carboxylate-Modified Microspheres, 1.0 μm, negative charged in 7.5 pH solution
- F8765 FluoSpheres Amine-Modified Microspheres, 1.0 μm, positive charged in 7.5 pH solution
- F8859 FluoSpheres Sulfate Microspheres, 4.0 μm, negative charged in 7.5 pH solution

All the microspheres of choice were yellow-green fluorescent (505/515 nm).

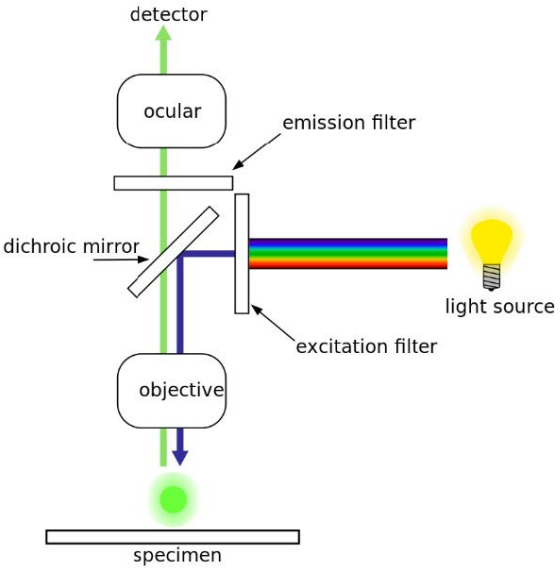

FIGURE 3.13: Operating principle of a fluorescence microscope.

These spheres have a relative density of 1.05. This means that they will tend to sediment on the bottom of the chips, thus affecting the diffusion mechanism and compromising the results. To overcome this problem we increased the density of the solution in which they are submerged. This has been obtained by simply adding a precise amount of **sucrose** in the water. In order to have a density of 1.05 g/ml we used a concentration of sucrose of 12.62% Sucrose has been chosen because its presence does not affect the pH and the ionic strength of the solution.

3.6.3 Fluorescence Microscopy

The spheres were made of polystyrene so they were practically transparent, hence a traditional optical microscope was not suited to observe them. In order to overcome this problem we used a **fluorescence microscope**

A fluorescence microscope is an optical microscope that uses fluorescence and phosphorescence instead of, or in addition to, reflection and absorption to study properties of organic or inorganic substances. The specimen is illuminated with light of a specific wavelength (or wavelengths) which is absorbed by the fluorophores, causing them to emit light of longer wavelengths (i.e., of a different color than the absorbed light). The illumination light is separated from the much weaker emitted fluorescence through the use of a spectral emission filter (see Figure 3.13). Our equipment was a *Zeiss BioScope microscope with Axio Observer*.

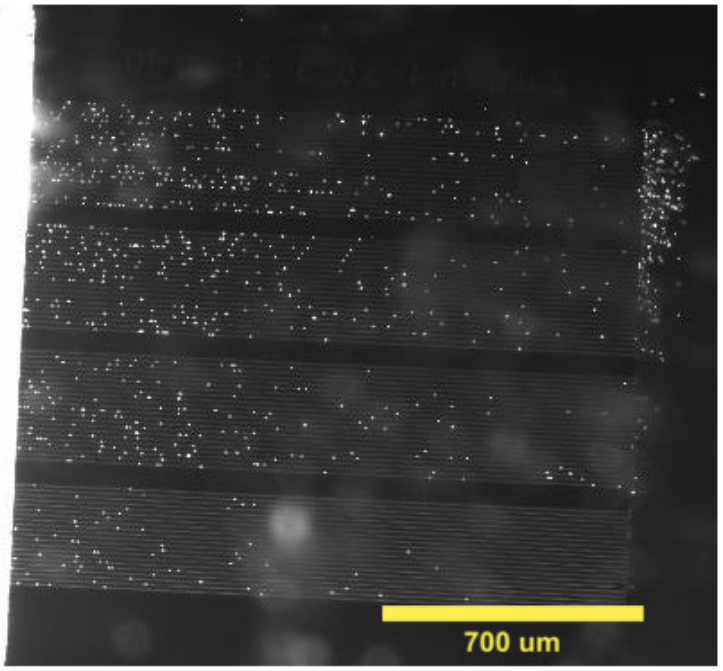

FIGURE 3.14: Diffusion dynamics of ammino-functionalized spheres at pH 5. The fastest spheres are those in the wider channels arrays. Journey times are: 31 minutes for spheres in the 4 μm wide channels, 65 minutes for spheres in the 3.5 μm wide channels, 85 minutes for spheres in the 3 μm wide channels and 4 hours for spheres in the 2.5 μm wide channels. After 15 hours the diffusion is still very active, with net flux towards the sink reservoir.

3.7 Observations Results

The motion of the spheres in the channels is affected by these factors:

- Functionalization (Ammino, Carbox, Sulfate);
- pH of the solution in which they are submerged;
- Size of the channels. We will distinguish *narrow channels* chips, with 2.5, 3, 3.5 and 4 μm wide channels, and *large channels* chips, with 4.5, 5, 6 and 7 μm wide channels.

We summarize here the observations:

For ammino-functionalized spheres in narrow channels:

- Acid (pH 3 and 4): partial gating, slow diffusion;
- Neutral (pH 7): diffusion;

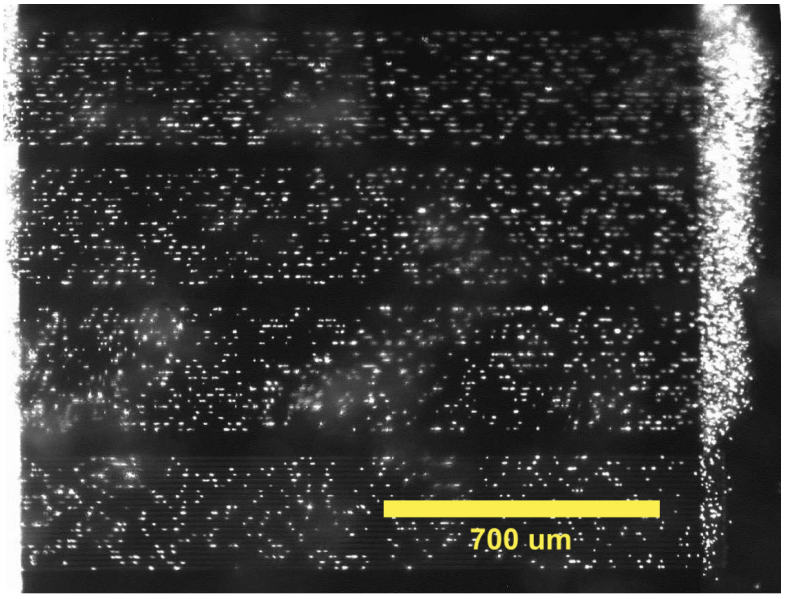

FIGURE 3.15: Diffusion dinamics of ammino-functionalized spheres at pH 11. At the beginning of the observation spheres have already reached the end of the channels and their motion is fast. Channel width are respectively 4, 3.5, 3 and 2.5 μm. The relative diffusion speed is evident from the amount of particles in the sink reservoir.

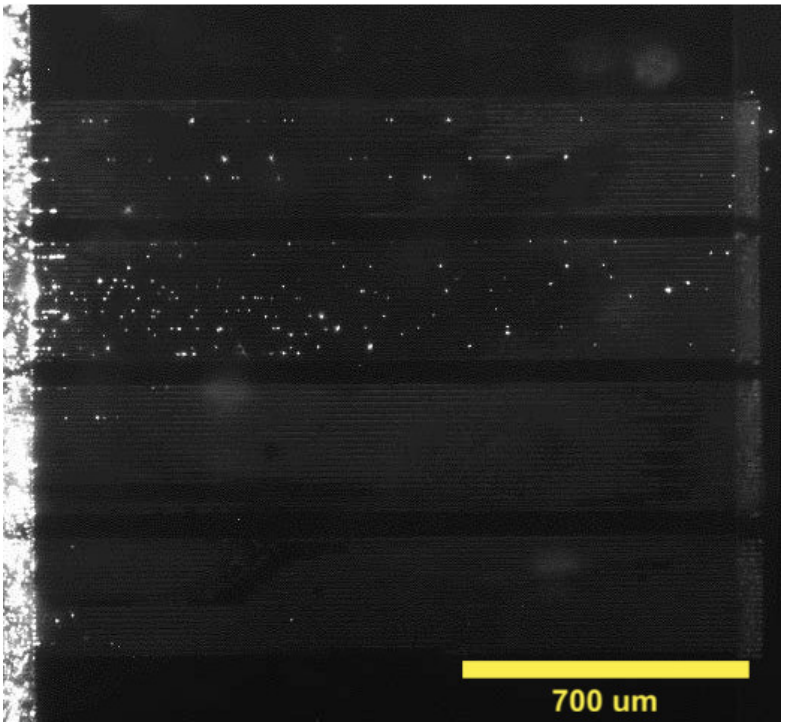

FIGURE 3.16: Diffusion dinamics of ammino-functionalized spheres at pH 13. Gating effect is observed: most of the spheres are kept outside the channels. Few particles succeed in entering the channels at the very beginning probably injected by pressure differences.

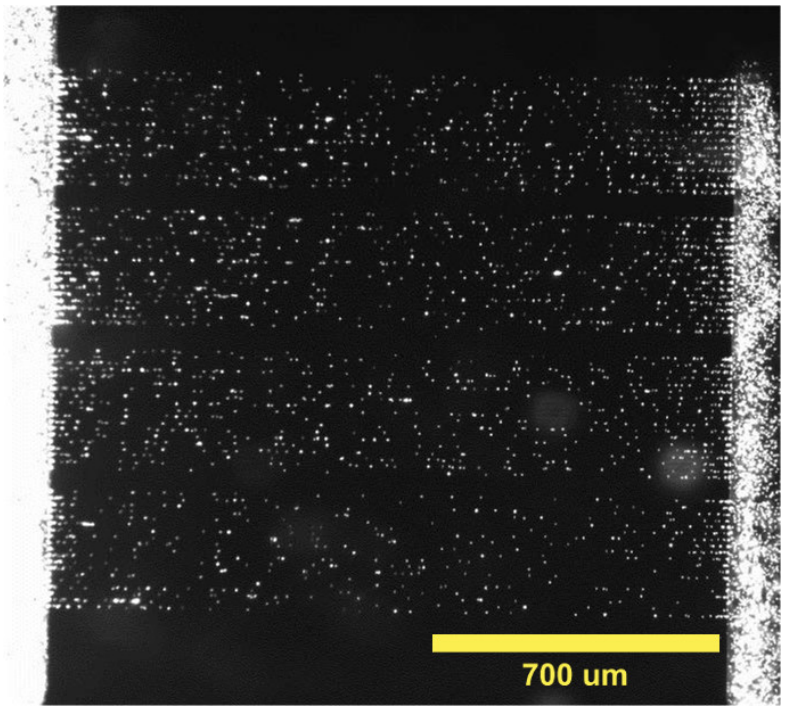

FIGURE 3.17: Diffusion dinamics of carboxylate-functionalized spheres at pH 2. All the channels are filled with stuck particles which prevent other particles from entering the channels.

- Basic (pH 11): fast diffusion;

in large channels:

- Acid (pH 2): sticking;
- Neutral (pH 6): diffusion with gradual sticking;
- Basic (pH 9): fast diffusion; good mobility.

Carboxyl-functionalized spheres in narrow channels:

- Acid: missing data;
- Neutral (pH 7): diffusion;
- Basic (pH 10,12): fast diffusion, bad mobility;

in large channels:

- Acid (pH 2,4 and 6): diffusion with gradual sticking: the more acid, the faster the sticking;

- Neutral (pH 7): diffusion;
- Basic: missing data.

Sulfate-functionalized spheres in narrow channels: not tested (diameter of microsphere exceeds channel dimensions);
in large channels:

- Acid (pH 4): slow diffusion with gradual sticking; bad mobility
- Neutral (pH 7): gating in the narrowest array , slow diffusion in the others;
- Basic (pH 9): mobility only in the largest channels.

3.8 Preliminary evaluation of gate and gate oxide implementation for nanofluidic transistor application

What we describe here is just a short report of feasibility involving the eventual integration of a process presented in the first section, involving the growth of Ta_2O_5 over a metallic electrode, for a nanofluidic transistor application.

In nanofluidic transistors the main challenge is to obtain a insulating layer over a electrode preventing leakage currents. One of the cause of bad insulating properties of common oxides (SiO_2, Al_2O_3) is the possibility of corrosion due to the action ionic species inside biological solution. Ta_2O_5 is a good candidate for gate oxide in these application, being also uses as anticorrosive coating in pH sensors [92].

To investigate the corrosion resistence of Ta_2O_5 we fabricated a sample as discussed in the previous chapter by thermal oxidation of tantalum: we used a platinum electrode on a silicon/silicon nitride wafer covered by Ta_2O_5. For mimic a biologic environment we used a 0.1 M *phosphate buffered saline* (PBS) solution. PBS is a buffer solution commonly used in biological research. It is a water-based salt solution containing sodium phosphate, sodium chloride and, in some formulations, potassium chloride and potassium phosphate.

Some samples have been kept in a stirred PBS solution for 48 hrs at 40° C and others at 80° C . Parafilm has been used to prevent evaporation during the experiment. We then compared the samples with the different treatments by SEM analysis.

By comparing SEM pictures (Figure 3.18) we can notice no evident modification of the surface, just we can see some impurities probably due to some salt precipitation during the experiment.

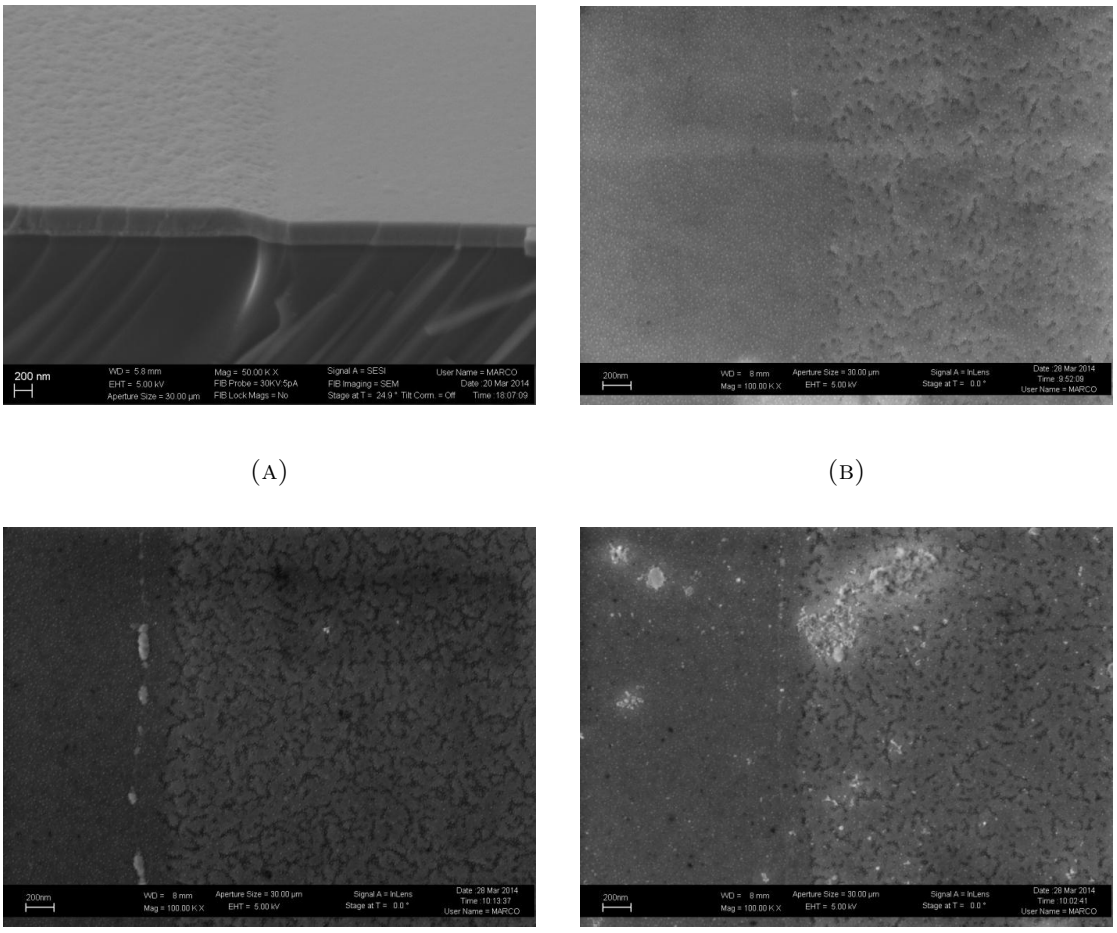

(A) (B)

(C) (D)

FIGURE 3.18: SEM characterization of Ta_2O_5 layer on metal before and after immersion in PBS. **A.** Tilted and **B.** frontal view of not immersed sample. Roughness is more accentuated where the oxide is grown on metal electrode. **C.** Surface of the samples after 48 hrs immersion in PBS at 40° C and **D.** at 80° C.

By this characterization we can conclude that Ta_2O_5 is a good candidate for nanofluidic transistor gate oxide application. Further characterization will involve the application of a voltage to the underlying electrode in order to evaluate field effect induced corrosion. The applied field, in fact, modifies the concentration of the ions at the surface, thus in principle enhancing the corrosion.

Chapter 4

Conclusive Remarks

In the first part of this work we analyzed different possibilities for the fabrication of sensors based on Organic Thin Film Transistors (OTFTs). Our approach has been process-oriented in order to give a report of feasibility with low-cost fabrication. Our consideration started from the basic step of these devices fabrication until electric characterization. The main challenge has been to provide OTFTs with addressable metallic gate electrode in order to better investigate the process integration on these devices. In this work, being a pioneering activity, the organic semiconductors sensing capabilities are not yet been investigated, but we provided a qualitative description of the semiconductors processability and their compatibility with classical MEMS oriented processes. One part of the following work could be finding suitable means to activate the semiconductor surface in order to investigate target biological sensing, on the other hand another possible future implementation could be based on the microfluidic integration of this device by fabricating a suitable case with a channel leading to the active part of the transistor.

In the second part we presented an application for controlled drug release systems. The technology involved in this part is usually related to control the diffusion dynamics of ionic species through nanochannels. We discussed here the design, fabrication and characterization of a chip for a scaled-up microscopic simulation molecular drug dynamics. Charged fluorescent microspheres played the role of drug molecules and micrometric channels were the magnificated reproduction of nanochannels. The microspheres were driven in our simulation by the pH of the solution of choice. The experimental setup was fabricated with similar microfabrication technologies involved in the first part of my work.

A future approach could take in account the implementation of a gate electrode and gate oxide to better control the diffusion of ions in nanochannels (or microspheres in

microchannels in our system). For this purpose we reported a preliminary study on the possible application of part of the technology developed in the first part of the thesis for the fabrication of a nanofluidic transistor.

This work has been oriented towards the technological integration of multiple aspects relating biological microtechnologic devices, both for sensing and drug administration with the future perspective of integrating in the same chip both diagnosis and terapeutic tools.

Appendix A

Thin film transistors (TFTs) basic theory of operation

This part is a theoretic treatment (from [26]) on TFT. The aim of this appendix is to provide a description of the current theory regarding TFT conductive behaviour. We will discuss mainly the effects that were easily observable in the characterization phase of our devices.

A.1 Noncristalline semiconductors

Since most of materials used in TFT are noncrystalline, the treatment of the material by a band model might seem inadequate. However a periodic electric field of the lattice is not essential for the occurrence of typical semiconducting properties and the band model may be applied also in the case in which there is a loss of periodicity of the lattice [93].
Long-range order is not needed to give the material semiconducting properties. The edges of the bands are not well defined though. In other words, noncrystalline (disordered) materials can be treated by semiconductor (band) theory with nondiscrete bands. Together with the noncrystallinity comes a large density of trap states and they severely change the electronic behavior. Trap states are deep localized states that can capture carriers that would otherwise contribute to conduction. It is irrelevant if the trap states originate from the disorder of the material or from impurities. Once captured by a trap, these charges are unavailable for conduction (in other words, the mobility is zero).

In band conduction the charge is highly delocalized and can travel freely. Charges, however, spend most of their time on localized deep states from where they cannot

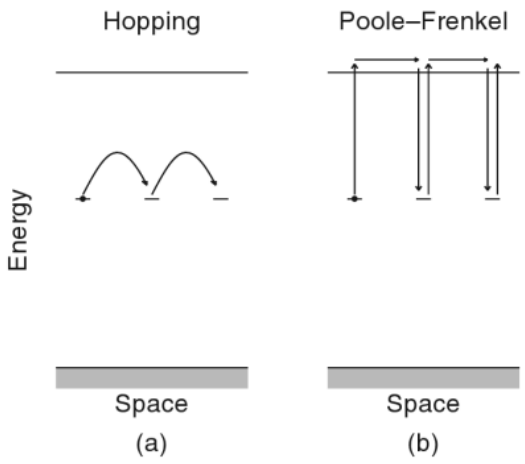

FIGURE A.1: Distinction between hopping conduction (a) and Poole-Frenkel conduction (b). In the former charges occasionally jump ('hop') from trap to trap. In the latter carriers spend most of their time trapped but occasionally are excited to the delocalized (conduction or valence) band from where they can contribute to current.

contribute to current, thus reducing the average mobility. One example of this is Poole-Frenkel conduction, which also includes a field-dependence of mobility.

In contrast, in hopping conduction models only localized states exist or play a role, for instance because the delocalized bands are too far away or the temperature too low to allow for thermal excitation of trapped carriers [94]. The charges spend all of their time on these states. Transport of charge occurs by instantaneous hops between these states. This can also cause a fieid and temperature dependence of the effective mobility.

A.1.1 Chemistry and conduction

Where the basic ingredient of organic materials is the carbon atom, the basic ingredient of organic semiconductors is conjugation. Conjugation is a chain of carbon atoms with alternating single and double bonds, as shown in Figure A.2.

This has two important results, namely the opening of a band gap, a splitting of the energy levels, in the range of semiconductors, and the delocalization of charge in these levels.

The four electrons on each carbon atom in the chain can be considered to reside in sp^2 hybridized orbitals and in a p_z orbital. The three sp^2 electrons are used to form covalent bonds via σ molecular orbitals to neighboring carbon atoms in the chain on either side and to the sidegroup (for instance a simple hydrogen atom). The remaining electron in the p_z orbital is then used in a covalent bond via a π molecular orbital with a neighboring

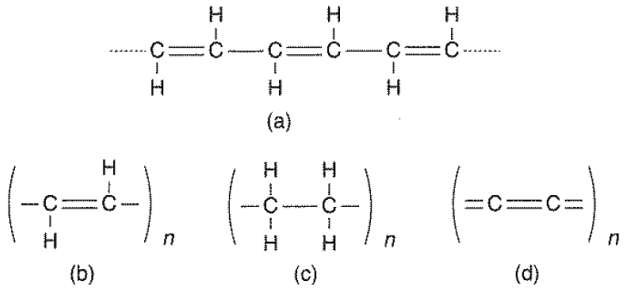

FIGURE A.2: (a) The principle of conjugation in organic electronic materials shown in Lewis structures. Conjugation consists of a chain of carbon atoms with alternating single and double bonds. Note that any of the hydrogen atoms can he replaced by a functional side group, for instance to make the compound soluble. (b) The simplest organic polymeric semiconductor, polyacetylene. (c) The nonconjugated equivalent, polyethylene. The difference in room temperature conductivity between polyethylene and polyacetylene is about seven orders of magnitude. (d) Polyallene with only double bonds also has relatively low conductivity

carbon atom in the chain on one side only. The result is a chain of alternating single (σ only) and double (σ and π) bonds.

Figure A.3 shows the energy diagram of an interaction between two carbon atoms forming a double bond. After filling the levels from low to high it can be recognized that four electrons (two from each carbon atom) are used in bonding, two in σ molecular orbitals, and two in π molecular orbitals. The remaining four electrons are in nonbonding orbitals and are still available for bonding to the rest of the chain and the ligands. The basic feature is the splitting between the π and $\pi*$ molecular orbitals caused by the interaction between the p_z atomic orbitals. interactions between p_z orbitals further away in the chain cause additional, smaller splittings of the levels, as schematically indicated in Figure A.3(b). A highest occupied molecular orbit (HOMO,π) and lowest unoccupied molecular orbital (LUMO, $\pi*$) can be recognized.
The formation of a chain of single and double bonds thus causes an energy structure with a HOMO and a LUMO level, with a splitting ('band gap') in the range of semiconductors.
For polymeric organic electronic materials, the size of the chain of alternating single and double bonds is, in principle, infinite. For oligomeric organic materials, the chain is limited to the molecule.

For limited conjugation lengths, macroscopic conduction is then made possible by further overlap of molecular orbits with neighboring molecules, causing so-called Davydov splitting of the molecular levels. Figure A.4 summarizes the intramolecular interactions causing molecular orbits and inter-molecular interactions further dispersing the

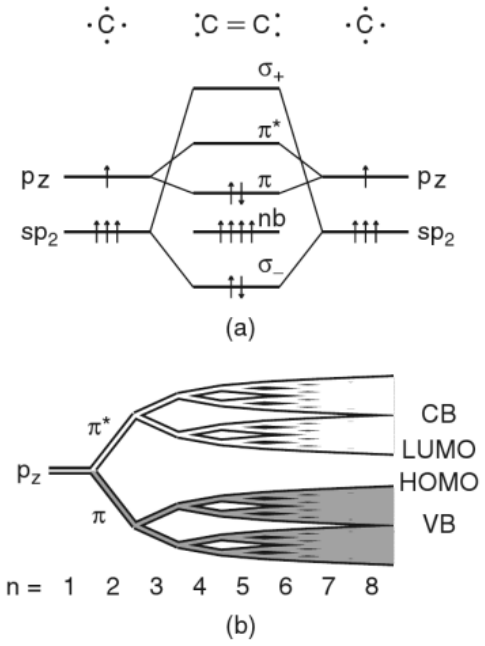

FIGURE A.3: (a) Energy diagram of two interacting carbon atoms. sp_2 and p_z atomic orbitals of the two individual carbon atoms combine to form π, σ and nonbonding molecular orbitals. (b) A hand structure starts emerging with a narrowing hand gap when the conjugation length of alternating single and double bonds is increased. A HOMO and LUMO can he recognized that is part of the valence band (VB) and conduction band (CB), respectively.

energy levels, and delocalizing the electrons. The interactions cause the wavefunctions with maximum same-sign overlap to have lowest energy and those with proximity of opposite-sign parts to have highest energy.

Half of the electronic states are occupied (each p_z orbital contributes one electron and in each electron wavefunction fit two electrons, with opposing spin directions) and in this way a HOMO and LUMO can be identified.

When the splitting between these two levels is relatively small, and a large delocalization of the electrons occurs, a semiconductor results. In this case it is better to use the jargon of semiconductor physics and replace the chemistry words 'HOMO' and 'LUMO' by 'valence band' and 'conduction band', respectively. In this language, we can say that an electron is promoted from the top of the valence band (VB) to the bottom of the conduction band (CB). Both the electron in the CB (LUMO) and the missing electron, or 'hole', in the VB (HOMO) can nearly equally well contribute to current. In practice, most organic semiconductors conduct better via holes because of a higher efficiency of trapping (immobilizing) electrons.

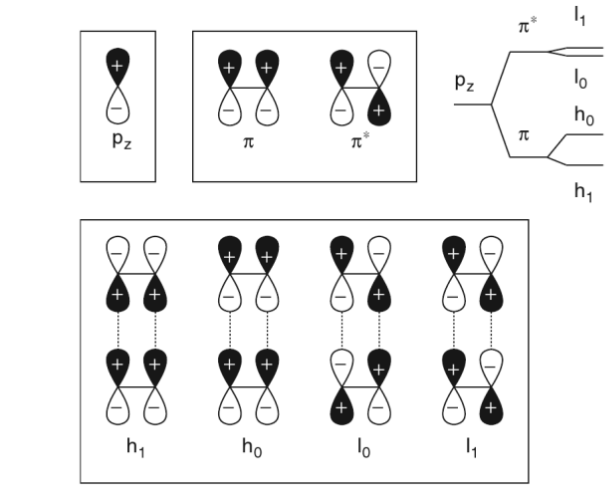

FIGURE A.4: lntramolecular interactions between p_z electrons causing molecular orbits π and $\pi*$. Additional (intermolecular) interactions cause a further spreading of the electronic levels. The interactions make the Wavefunctions with maximum same sign overlap to have the lowest energy, in this case h_1 and the Wavefunction with maximum opposite-sign overlap to have the highest energy, in this case l_1. Half of the levels are occupied and this causes the distinction between HOMO and LUMO (in this case h_0 and l_0, respectively)

A.2 A simple model to describe TFTs

We report here a simple analytical model for thin-film field-effect transistors (TFTs) [95, 96] useful to rapidly identify why a device is behaving in a particular peculiar way. The active layer of the devices is considered purely two-dimensional.

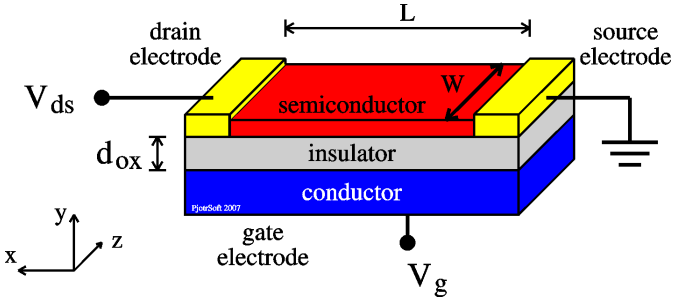

FIGURE A.5: Cross-section of a thin-film FET showing the nomenclature used in this part.

Fig. A.5 shows a cross-section of a thin-film FET with the nomenclature used in this part. The device consists of a conductor called the gate (made of metal or a highly doped semiconductor) an insulating layer (which we will call the oxide layer, as an inheritance from silicon technology) of thickness d_{ox} (resulting in capacitance density $C_{ox} = \epsilon_{ox}/d_{ox}$,

with ϵ_{ox} the permittivity of the insulator material) and a semiconducting layer that accommodates the channel of charged carriers and can thus be called the active layer. The basic working principle of the field effect transistor is that charge density in this layer and thus its conductivity can be modulated by a tension at the gate relative to the semiconductor. The charges are injected and collected by the source and drain electrodes, respectively. Observable external electrical quantities are: I_{ds} the drain–source current, V_{ds} the drain–source voltage and V_g the gate–source voltage. The leakage currents, such as drain-gate or gate-source, are considered zero.

It is standard practice in literature to use textbook inversion - channel metal - oxide - semiconductor field-effect transistor (MOS-FET) theory to describe the behaviour of organic FETs [97]. There are two reasons why this might be inappropriate. First, the real devices are, without fail, thin-film FETs (TFT) and as such do not have a bulk region. The main concern is that a TFT, without a bulk region, cannot accommodate a band bending. Second, organic TFTs are all accumulation-channel FETs. In this situation, in the absence of localized states (donors) to store immobile positive charge, no band-bending can be maintained, even if the active layer is thick. Summarizing, the thick semiconductor in a standard MOS-FET can accommodate band bending and will have band bending in inversion mode. Charges induced by the gate are then not all located close to the interface and a complicated charge-voltage and hence current-voltage relation results. In a thin-film FET, or in general an accumulation-type FET, all induced charge is necessarily close to the insulator and the charge-voltage relation is always simply:

$$\rho(x) = [V(x) - V_g]C_{ox} \tag{A.1}$$

with ρ and V the local charge per area and voltage in the channel, respectively. This charge in a TFT might still be either mobile or immobile, though. This explains why, as has been shown, for organic FETs only the quality of the first monolayer matters. At best, the consecutive layers help to stabilize the integrity of the first layer, in terms of diffusion of impurities and crystallinity.

For a standard MOS-FET, the assumption is made that the induced free charge in the channel is linearly depending on the gate bias. This is because, once the channel has been formed, all the charge induced by the gate is free charge. This in turn is caused by the type of semiconductor used in FETs. For traditional materials as Si or GaAs, the acceptors and donors introduce shallow levels, which are consequently all ionized at all operational temperatures. In organic semiconductors, the acceptor and donor states are very deep and abundant. As a result, even at room temperature, not all levels are

ionized and temperature and bias can change the degree of occupancy. As we will show, the as-measured mobility does not change because of an increased depth of the acceptor level. On the other hand, traps, that differ from acceptors in that they can be neutral or positively charged, have a severe effect on the electrical characteristics of the device.

First we will derive equations for the basic operation of a TFT. Then we will discuss the differences and perturbations to the model, including contact effects and traps. As a starting remark, the units of densities used are all "per area". This includes the charge densities, carrier densities and densities of states.

A.2.1 Basic model

It is easy to show that the equation for currents of a MOS-FET is also applicable to thin-film FETs. In the case of a TFT the thickness of the channel is constant, but the density of charges p inside the channel varies from one electrode ("source", $x = 0$) to the other ("drain", $x = L$). To calculate the currents through the device, we have to understand that, locally, the current $I_x(x)$ at a certain point x in the channel is equal to the local induced charge, $C_{ox}[(V_g - V_t) - V(x)]$, multiplied by the carrier mobility μ (for a definition of mobility see [8]), the field felt by the charges, $dV(x)/dx$, and the channel width W. In other words, we have the following differential equation:

$$I_x(x) = qWp(x)\mu\frac{dV(x)}{dx}, \quad p(x) = \frac{C_{ox}[V(x) - (V_g - V_t)]}{q} \tag{A.2}$$

where V_t is the threshold voltage, the lowest voltage (in absolute value) which affects the conductivity of the channel. The threshold voltage can only deviate from zero in the presence of traps. With boundary conditions $V(0) = 0$, $V(L) = V_{ds}$, and $I_x(x) = I_{ds}$ for all x, the solution is

$$I_{ds} = -\frac{W}{L}C_{ox}\mu[(V_g - V_t)V_{ds} - \frac{1}{2}V_{ds}^2] \tag{A.3}$$

with V_{ds} and V_g both negative. This equation for TFTs is very similar to the equation for MOS-FETs [8]. The only prerequisite is (low) ohmic contacts. The effects of the contacts will be discussed later. The equation is valid up to $V_{ds} = V_g - V_t$. After that, saturation starts in: a region close to the drain is below threshold voltage and is devoid of charges. When the sub-threshold conductivity is (close to) zero this region can be infinitely small and still absorb all of the above-saturation voltage $V_{ds} - (V_g - V_t)$. In this way, the charge and voltage distribution across the device (except for an infinitely

thin zone) is independent of the drain-source voltage and hence the current is constant at $I_{ds} = -(1/2)(W/L)\mu C_{ox}(V_t - V_g)^2$.

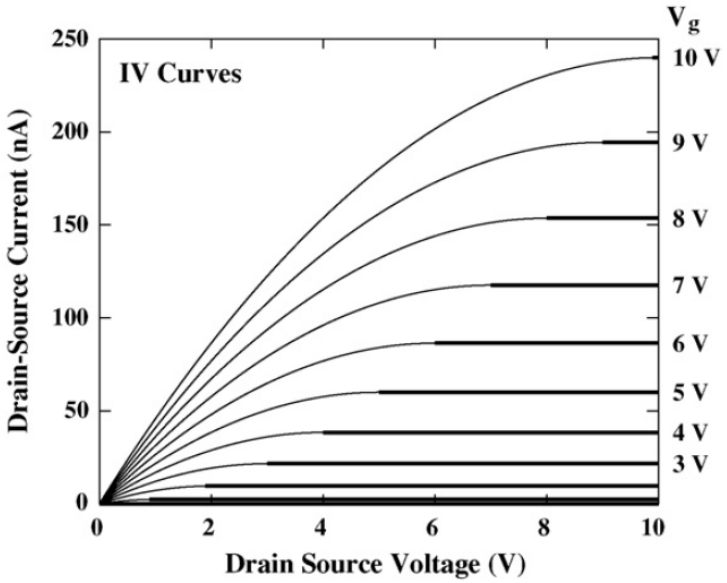

FIGURE A.6: I–V curves (I_{ds} vs. V_{ds}) of an ideal thin-film FET resulting from equation (A.3) (thin lines) . Absolute values for current and voltage. Thick lines indicate the saturation regime.

Fig. A.6 shows the electrical characteristics of an ideal TFT.

For low voltages, the quadratic term in V_{ds} disappears from Eq. (A.3) and this is called the linear region (considering $V_t = 0$):

$$I_{ds} = -\frac{W}{L} C_{ox} \mu V_g V_{ds} \tag{A.4}$$

This allows for the definition of the as measured field-effect mobility as

$$\mu_{FET} = \frac{dI_{ds}}{dV_g} \frac{1}{W/LC_{ox}V_{ds}} \tag{A.5}$$

where the subscript FET is used to distinguish it from mobilities measured by other techniques. For various reasons, for an organic TFT, the as-measured mobility can depend on things such as the temperature and the bias and can substantially deviate from mobilities measured with other techniques [95].

A.2.2 Contact resistence

In organic TFTs, often non-linearities in I–V curves are observed [98]. The argumentation is using the generic term "contact effects" [99]. In an FET there might be two possible contact effects, namely contact resistance [100] and contact Schottky barriers [101].
The first might be caused by the formation of a high resistive area in the vicinity of the drain and source electrodes. This can then impede carrier injection. A standard procedure for extracting this resistance is by measuring the device resistance as a function of channel length and extrapolating to zero [102]. This method requires an easy access to a large number of devices prepared under identical conditions and is rather time consuming. Later we will present a faster way of determining the contact resistance.

On the other hand, when a metal is brought into intimate contact with a semiconductor, usually a depletion layer is formed at the interface [8]. When their respective work functions are different, a Schottky barrier results that limits charge carrier injection. Note that the work function of the semiconductor is here defined as the electron affinity plus the Fermi-level depth, or, in other words, the distance between the vacuum level and the Fermi-level. Now we will demonstrate the effects of both type of contacts on the electrical characteristics.

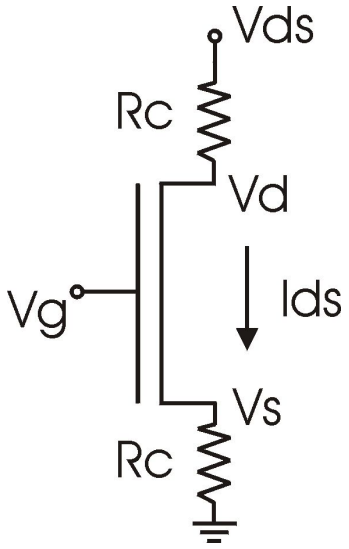

FIGURE A.7: Equivalent circuit of an FET with resistances at the contacts

For strong currents, the contact resistance can become the limiting factor and the current saturates and becomes independent of V_g: we have to imagine that the FET is made up of two contact resistances ($2R_c$) and the channel resistance, connected in series. Initially the current grows linear with V_g (as explained by the text above). The channel resistance is thus proportional to $1/V_g$. For large V_g the channel resistance disappears

and the current settles at $V_{ds}/2R_c$. More exact: when the current is increasing, the contact resistance induces a voltage drop at the source, $V_s = I_{ds}R_c$, the field at the source ($V_{gs} = V_g - V_s$) is reduced and the current drops.

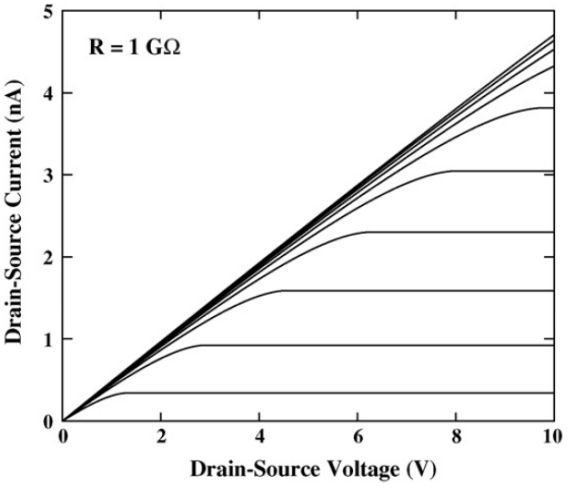

FIGURE A.8: Simulations of I–V curves of FETs with contact resistance R as indicated for different gate bias. Absolute currents and voltages shown.

The interface regions are not necessarily ohmic, as described above. Contacts are normally made of metal and the contact of this metal with a semiconductor might result in a Schottky diode. When a depletion layer is formed between the electrodes and the semiconductor, the current, might be limited by this Schottky barrier. When such Schottky barriers exist, they come in pairs, with a forward biased Schottky diode at the drain and a reverse-biased Schottky diode at the source (or vice verse). In other words, the maximum current through the device is a reverse-biased Schottky barrier current. When the Schottky barriers are the limiting elements, the current thus follows a hyperbolic tangent, $I_{ds} = \tanh(V_{ds})$ and saturates at a voltage of approximately $V_{sat} = kT/q = 26mV$ at room temperature, see the simulation A.10. This is not what is normally observed for TFTs. The conclusion therefore is that Schottky barriers play no role in TFTs [95].

A.2.3 Effects of traps on the electrical characteristics of TFTs

Non-linearities are often observed in I–V curves. They can be described as supra-linear close to the origin, and are often attributed to the effects of the contacts. As we have shown, this in not an adequate physical picture. We will now discuss how an abundant amount of traps can readily explain these anomalous I–V curves.

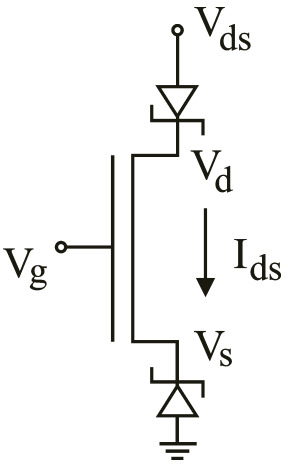

FIGURE A.9: Equivalent circuit of an FET with Schottky barriers at the contacts

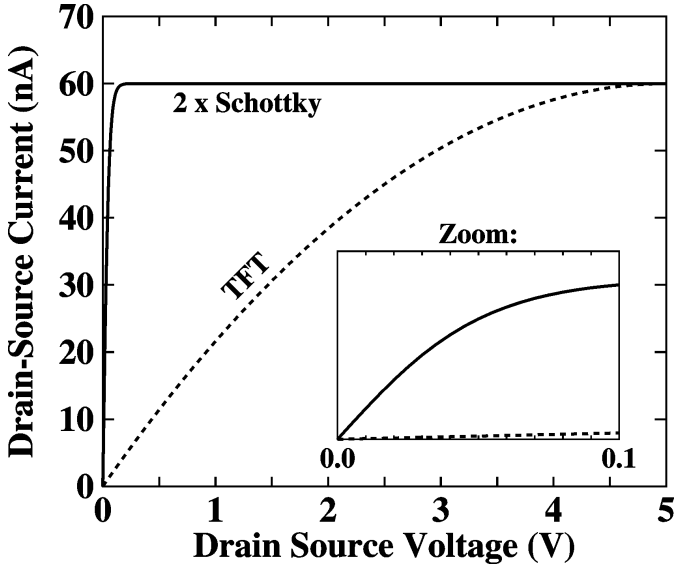

FIGURE A.10: Simulation of an FET with Schottky barriers at the contacts.

A Poole and Frenkel approach shows how the current, and thus the effective mobility ($\mu \propto I_{ds}/V_{ds}$), of a trap-ridden material can depend on the temperature and electrical field [8]:

$$\mu_{PF} = \mu_0 exp\left[-\frac{(E_T - E_V) - q\sqrt{q|E_x|/\pi\epsilon}}{kT}\right], \tag{A.6}$$

with μ_0 the free carrier mobility, $E_T - E_V$ the discrete trap depth, $E_x = dV(x)/dx$ the in-plane electric field, ϵ the permittivity of the material and q the elementary charge. Including a field dependent mobility into the model, the differential equations for TFTs now become

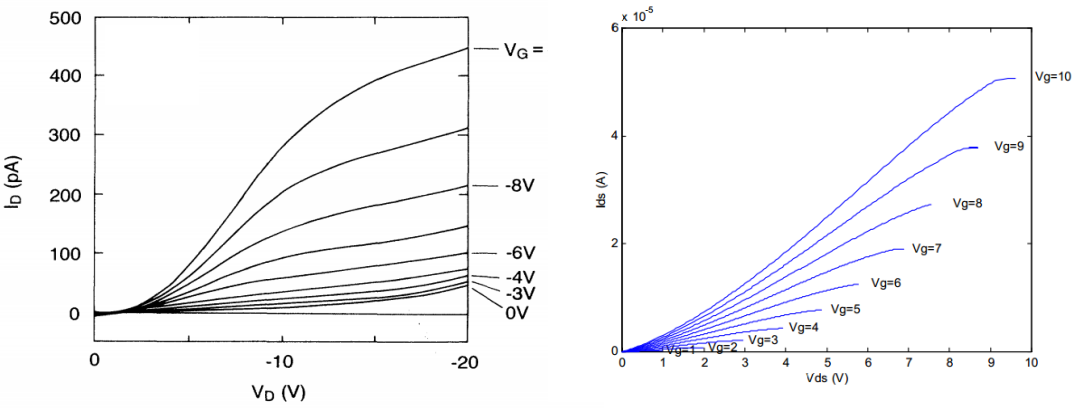

(A) (B)

FIGURE A.11: (A) Experimental from [103] and (B) simulated I–V curves for field-dependent mobility as described by Poole and Frenkel model. For significative field dependence, the curves become pronouncedly concave (supralinear).

$$\begin{aligned} I_x(x) &= Wqp(x)\mu(x)\frac{dV(x)}{dx} \\ p(x) &= \frac{C_{ox}[V_g - V_t - V(x)]}{q} \\ \mu(x) &= \mu_{00}\exp\left(-\frac{a}{kT}\sqrt{q|dV(x)|/dx}\right), \end{aligned} \tag{A.7}$$

where the same boundary conditions apply as before ($V(0) = 0$, $V(L) = V_{ds}$ and $I_x(x) = I_{ds}$) and $\mu_{00} = \mu_0 exp[-(E_T - E_V)/kT]$ depends on the temperature and the trap depth and $a = \sqrt{q^3/\pi\epsilon}$ is a constant that depends only on the permittivity of the material (ϵ). The above equations do not have a simple analytical solution, however, they are not difficult to solve numerically. Fig. A.11a shows experimental data and Fig. A.11b shows simulations of the I–V curves for different temperatures (see [96]).

A.2.4 Insulator Leakage

In many cases, the insulator is less-than-perfect and currents may exist through the insulator to the gate. For high mobility materials, such as silicon in the MOS-FET geometry, even the low-end silicon oxide is good enough and gate currents are negligible compared with channel currents. For most organic materiais and for TFTs of low mobility materials in general, the channel currents are smaller and requirements on the insulator stronger if distortions of the ideal characteristics are unwanted. In a very rudimentary way, is possible simulate this by placing a resistor bridging the drain and the

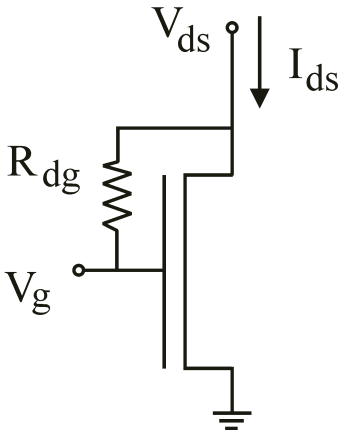

FIGURE A.12: Equivalent circuit of an FET with leakage

source (assuming the current meter is placed at the drain), as shown here on the picture A.13.

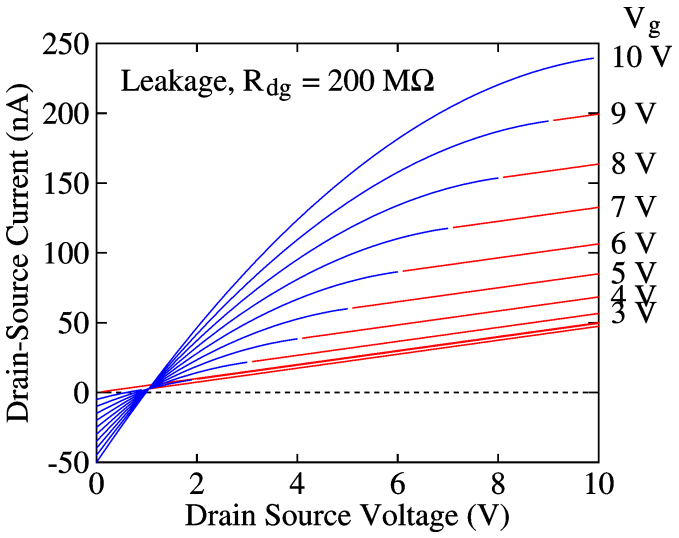

FIGURE A.13: Simulation of I-V curves of an ideal TFT with a resistor bridging the gate and the drain. The thin lines are the linear regime and the thick lines are the saturation regime

A way of eliminating the measured leakage current is to measure with V_{ds} always equal to V_g, in what is callled 'locus curves' since they follow the locus points of FigureA.6. This reduces the power of electrical measurements as an analytical tool, though. Moreover, it reduces the device effectively to a simple nonlinear two terminal component, like a diode.

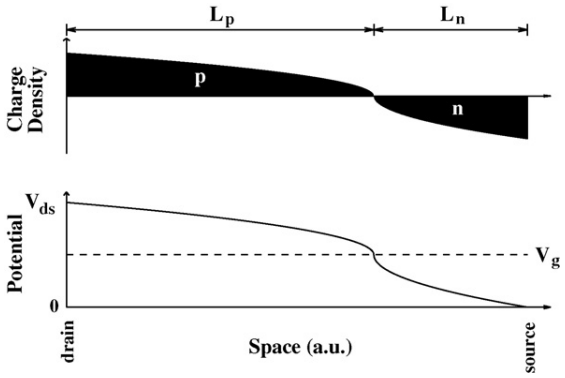

FIGURE A.14: Charge distribution and potential in an ambipolar TFT when the gate bias is in between the drain and the source bias. For this conditions, the device is in a dual-injection regime, with a zone of positive and zone of negative charge.

A.3 Ambipolar devices

We will now extend the idea and show what happens when electrons have a mobility comparable to that of holes. When ignoring the sub-threshold ("minority carrier") concentrations, the basic equations are replaced by

$$V(x) > V_g : \tag{A.8}$$

$$p(x) = \frac{C_{ox}[V(x) - V_g]}{q} \tag{A.9}$$

$$n(x) = 0 \tag{A.10}$$

$$V(x) < V_g : \tag{A.11}$$

$$p(x) = 0 \tag{A.12}$$

$$n(x) = \frac{C_{ox}[V_g - V(x)]}{q} \tag{A.13}$$

and

$$I_x(x) = qW\left[p(x)\mu_p + n(x)\mu_n\right]\frac{dV(x)}{dx} \tag{A.14}$$

with μ_p and μ_n the effect field-effect mobility of holes and electrons, respectively. In the general case, the solution is not just treating the device separately as p-channel

and n-channel devices and then summing the currents, because both types of charge and current can exist at the same time in different parts of the device (with carrier recombination at the transition point in space). When the gate bias is outside the range 0 - V_{ds} it has only one type of charge throughout the device and it can be treated as a p-channel or n-channel device. Care has to be taken when V_{ds} and V_g are not of the same sign. It can be shown, by using device symmetry operations and potential offset invariance, that this, effectively, is equal to subtracting the drain bias from the gate bias and inverting the drain-source potential. A more complicated case exists when the gate bias is in the range between the drain and source potential. In this case, there exists a region of length L_n with free electrons and a region of length L_p with free holes, see Figure A.14 . At the junction point, the potential is equal to the gate-bias. When we assume that at this junction the electron– hole recombination is not the limiting factor, we can treat each region as an FET in saturation. Then, demanding equal current in both regions (example for $V_{ds} > 0$):

$$\frac{1}{2}\frac{W}{L_p}C_{ox}\mu_p(V_{ds} - V_g)^2 = \frac{1}{2}\frac{W}{L_n}C_{ox}\mu_n(V_g)^2 \tag{A.15}$$

and knowing that the total length is equal to the channel length:

$$L_p + L_n = L \tag{A.16}$$

will yield (for $V_{ds} > 0$):

$$I_{ds} = \frac{1}{2}\frac{W}{L}C_{ox}\left[\mu_n V_g^2 + \mu_p(V_{ds} - V_g)^2\right] \tag{A.17}$$

In the same way can be found for $V_{ds} < 0$

$$I_{ds} = \frac{1}{2}\frac{W}{L}C_{ox}\left[\mu_n(V_{ds} - V_g)^2 + \mu_p V_g^2\right] \tag{A.18}$$

Figure A.15 shows transfer curves of ambipolar devices. The thick parts of the curves indicate this dual-injection regime. The minimum of a particular transfer curve can be found by taking the derivative of Eqs. A.17 orA.18 and putting to zero:

$$V_g^{min}{}_{(V_{ds}<0)} = \frac{\mu_p}{\mu_p + \mu_n}V_{ds} \tag{A.19}$$

$$V_g^{min}{}_{(V_{ds}>0)} = \frac{\mu_n}{\mu_p + \mu_n}V_{ds} \tag{A.20}$$

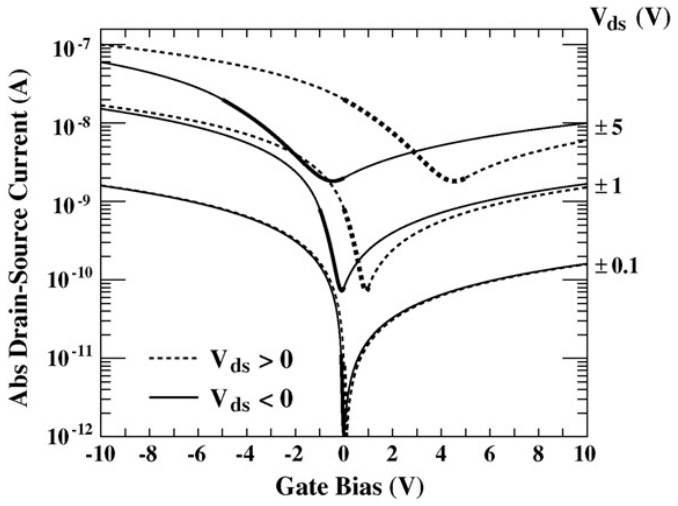

FIGURE A.15: Transfer functions for ambipolar devices for drain-source biases as indicated. The thick parts of the curves indicate the dual injection regime as shown in Fig. A.14. The solid curves are for negative drain-source biases whereas the dashed curves are for positive V_{ds}.

$$I_{ds} = \frac{1}{2}\frac{W}{L}C_{ox}\frac{\mu_p\mu_n}{\mu_p + \mu_n}V_{ds}^2 \tag{A.21}$$

The ratio of the positions of the minima in positive and negative bias thus directly yields the ratio of electron and hole mobility and can serve as a rapid evaluation tool of the material properties. Since normal saturation does not exist anymore (no infinitely thin zone can support a finite voltage drop), the effect on the I–V curves is pronounced, see FigureA.16. Note the absence of saturation for $V_{ds} > V_g$. After initially settling on a plateau, as for normal saturation, the current continues to increase rapidly.

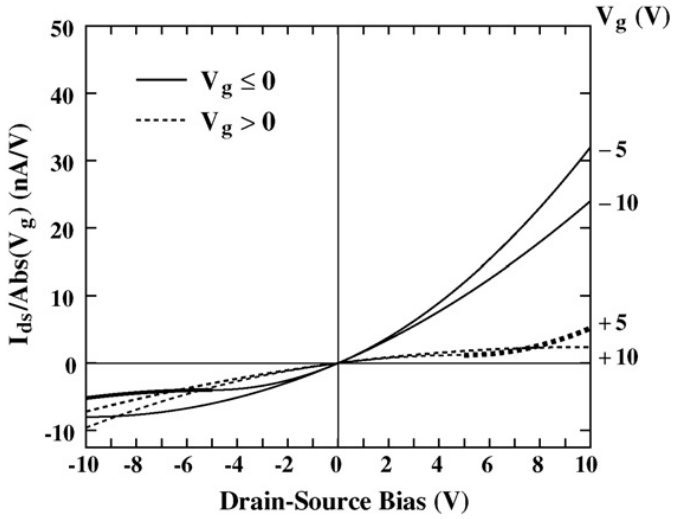

FIGURE A.16: I–V curves in linear scale for ambipolar devices for gate biases as indicated. The thick parts of the curves indicate the dual injection regime as shown in Fig. A.14. The curves have been scaled by the gate bias for visibility.

Appendix B

Theoretical background of diffusion kinetics in nanochannels

The basic principle of diffusion, as a mixing process with solutes free to undergo **Brownian motion** in three dimensions, in case of nanochannels or pores does not apply, since in at least one dimension solute movement within the nanopore is physically constrained by the channel walls.

Classical diffusion theory establishes that the movement of solute molecules in a non-homogeneous solution can be predicted, from a macroscopic point of view, by **Fick laws**. The basic principle is that the flux vector is proportional to the concentration gradient. Fick laws have been successfully applied to predict the diffusion kinetics of molecules through thin semipermeable membranes. Nevertheless, experiments have shown that, as the size of the membrane pores approaches the molecular hydrodynamic radius, unexpected effects, which cause substantial deviations from kinetics predicted by Fick laws, can occur [88].

One could impose a **single file dynamics (SFD)** diffusion, which implies N ($N \to \infty$) identical Brownian hard spheres in a quasi-one-dimensional channel of length L ($L \to \infty$), such that the spheres do not jump one on top of the other, and the average particle's density is approximately fixed. But, in the case of SFD, the molecular flux is overestimated by Fick law: the kinetics of SFD and Fickian diffusion are different because the molecules in SFD cannot pass each other in nanopores, regardless of the influence of the concentration gradient [104].

However, unlike SFD case, the ordering of solute particles imposed by the nanopore geometry is not as strict as true cylindrical pores, but particles could conceivably pass each other laterally. Furthermore, the wall drag effect has been evidenced using plastic

micro-sphere moving into microchannels, which could be significantly different from the case of low weight molecules diffusing in nanochannels [105].

B.1 Classical diffusion model

When there is a chemical potential gradient in a single-phase fluid mixture, which implies that a concentration gradient is present in the solution, each species will diffuse in the direction of decreasing concentration. The mathematical formula which describes this phenomenon is known as Fick law. It represents a linear relationship between the mass (or molar) flux J_A (with respect to the mass average velocity), and the concentration gradient, ∇c_A; for a binary mixture, Fick first law is given by [106]:

$$J_A = -D_{AB}\nabla c_A \tag{B.1}$$

where D_{AB} is the diffusion coefficient of a solute A in a solvent B. In order to have a good insight of the process, we first apply the classical theory to our specific case-study, but still neglecting the effect of the membrane. Then we will introduce the mathematical description of the membrane effect, so that we can compare this case with the free-diffusion case. The binary mixture consists of a solvent, e.g. phosphate buffer saline (PBS), and a given solute, which is initially concentrated in a well defined region of the reservoir volume. In order to obtain a suitable model, we require the following hypotheses to hold:

- the experimental volume, which contains the drug A, can be divided into two compartments of volume V_1 (the reservoir) and V_2 (the sink), with the respective initial mass concentrations $c^0_{A1} = c_{A1}(0)$ and $c^0_{A2} = c_{A2}(0)$ ($c^0_{A1} > c^0_{A2}$);
- the concentration is homogeneous in each compartment and the concentration variation is spatially defined in a thin boundary region of depth L;
- given a Cartesian reference system (O, x, y, z), the concentration gradient,∇c_A, has null components along the y and z axes. Therefore the mass flux turns out to be a scalar variable directed along the x axis and denoted by J_A.

Our aim is to calculate the mass flux of drug through a generic surface, of area S, which we assume to be perpendicular to the diffusion path. By a first order approximation [107] we obtain:

$$J_A(t) = (c^0_{A1} - c^0_{A2})\frac{D_{AB}}{L}e^{-\lambda_A t} \tag{B.2}$$

where:

$$\lambda_A = \frac{D_{AB}S}{V_1 L}\left(1 + \frac{V_1}{V_2}\right) \tag{B.3}$$

Therefore in the free diffusion case the release profile is exponential. At this point we can also calculate the amount of drug A, $Q_A(t)$, which passes from V_1 to V_2 over an arbitrary time interval $[0, t]$, by integrating the mass flux times the area, S, thus obtaining:

$$Q_A(t) = \int_S J_A(t)dt = (c^0_{A1} - c^0_{A2})\frac{V_1 V_2}{V_1 + V_2}(1 - e^{-\lambda_A t}) \tag{B.4}$$

B.2 Constrained diffusion model

Now let us derive the constrained diffusion model. Experimental results show that the release profile remains linear for a certain period, and then it switches to the Fickian exponential trend [88]. This observation suggests that the classical theory can be still suitable provided that we can devise a more general model capable of explaining the linear release in the first part of the experiment, and recovering the Fickian diffusion kinetics when the concentration drops below a certain threshold. Such model shall also shed some light on the physical mechanisms underlying the non-Fickian behavior observed in the diffusion experiments. First, consider that classical diffusion theory is based on Einstein relation, which expresses the diffusion coefficient of spherical Brownian particles in a solution as:

$$D_{AB} = \frac{kT}{6\pi r\eta} \tag{B.5}$$

where k is the Boltzmann constant, T the temperature, r the radius of the solute particles, and η the viscosity coefficient of the liquid.

In order to derive a more general model, one needs to take into account the fact that the mixture does not satisfy the hypothesis of ideal gas law. When the state of Brownian particles in the Einstein argument deviates from the ideal gas law, it assumes the form of the van der Waals equation:

$$\left(p + \frac{a}{\gamma^2}\right)(\gamma - b) = RT \tag{B.6}$$

where p is the pressure, R is the universal gas constant, and $\gamma = V/n$ is the molar volume, V being the total volume and n the number of moles. It is well known that the constants a and b have a physical interpretation: The term a/γ^2 represents the additional positive pressure caused by the presence of other solute particles, as a consequence of

the long-range attractive forces; the constant b, instead, represents the volume occupied by the gas molecules, so that the term $(\gamma - b)$ represents the effective "free volume". In the following, we will exploit [108] who derives from Eq. B.6 the generalized expression for the diffusion coefficient (compare with Eq. B.5):

$$D^*_{AB} = \frac{kT}{6\pi r\eta}\left[\frac{1}{(1-b_0\nu)^2} - \frac{2a_0}{kT}\nu\right] \tag{B.7}$$

where $\nu = \nu(t,x)$ is the average number of Brownian particles at position x at time t, $a_0 = a/N_0^2$, $b_0 = b/N_0$, and N_0 is Avogadro number. Note that the generalized coefficient D^*_{AB} recovers the Einstein coefficient D_{AB} when $a = b = 0$. It is important to note that, according to Eq. B.7, the diffusion coefficient is an increasing function of b, and a decreasing function of a. This is intuitively what we could expect, because the value of a is determined by long-range attractive forces, which oppose to particles dispersion, whilst the value of b is related to the short range repulsive forces, which foster particles dispersion. The generalized expression B.7 also allows deriving the effect of temperature and pressure variations on the diffusion coefficient: a temperature increase corresponds to a larger diffusion coefficient; conversely, a pressure increase has the opposite effect. The expression B.7 yields the following relation:

$$\frac{\partial\nu}{\partial t} = \left(\frac{kT}{6\pi r\eta}\frac{2b_0}{(1-b_0\nu)^3} - \frac{2a_0}{6\pi r\eta}\right)\left(\frac{\partial\nu}{\partial x}\right)^2 + \left(\frac{kT}{6\pi r\eta}\frac{1}{(1-b_0\nu)^2} - \frac{2a_0}{6\pi r\eta}\nu\right)\frac{\partial^2\nu}{\partial x}^2 \tag{B.8}$$

which is a generalized diffusion law (it recovers Fick second law of diffusion in the case $a = b = 0$) [106].

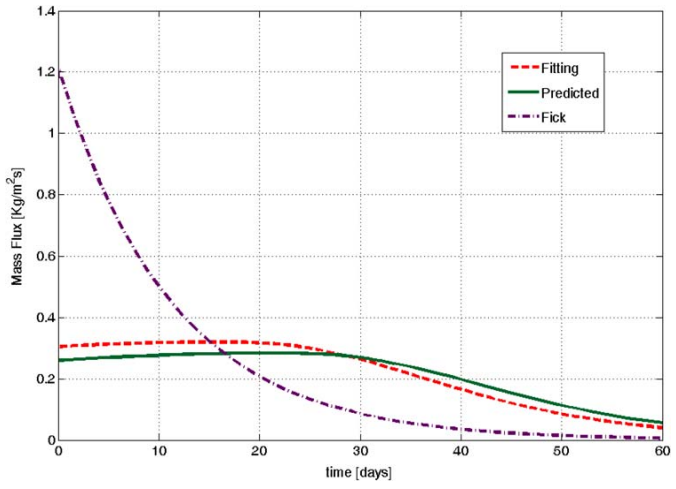

FIGURE B.1: Lysozyme mass flux through a 13 nm pore height membrane: Fick law prediction, model based simulation with parameters derived by fitting, model based simulation with parameters derived by molecular dynamics simulation. [109]

Figure B.1 shows result of comparison between a finite-element model and experimental

data [109]. Understanding the mechanism of diffusion through nanochannels is important not only from a theoretical perspective, but also in view of the potential applications of nanopore silicon membranes. The release rate has been shown to be constant for a long period, under suitable choice of the experimental parameters (initial concentration, channel height and size of solutes); this property can be exploited in clinical medicine for prolonged and constant administration of drugs.

Bibliography

[1] W. Menz, J. Mohr, and O. Paul. *Microsystem Technology*. Wiley-VCH Verlag GmbH, 2007.

[2] KSKS Sree Harsha. *Principles of vapor deposition of thin films*. Elsevier, 2005.

[3] Gilles Horowitz. Organic thin film transistors: From theory to real devices. *Journal of materials research*, 19(07):1946–1962, 2004.

[4] Flora Li, Arokia Nathan, Yiliang Wu, and Beng S Ong. *Organic Thin Film Transistor Integration: A Hybrid Approach*. John Wiley & Sons, 2013.

[5] Sami Franssila. *Introduction to microfabrication*. 2004.

[6] Clemens Rensch, Stefan Hell, Manfred Schickfus, and Siegfried Hunklinger. Laser scanner for direct writing lithography. *Applied optics*, 28(17):3754–3758, 1989.

[7] Etienne Menard, Matthew A Meitl, Yugang Sun, Jang-Ung Park, Daniel Jay-Lee Shir, Yun-Suk Nam, Seokwoo Jeon, and John A Rogers. Micro-and nanopatterning techniques for organic electronic and optoelectronic systems. *Chemical reviews*, 107 (4):1117–1160, 2007.

[8] Simon M Sze and Kwok K Ng. *Physics of semiconductor devices*. John Wiley & Sons, 2006.

[9] Wayne M Moreau. *Semiconductor lithography*. Springer, 1988.

[10] Arturo A Ayón, R Braff, Chuang-Chia Lin, Herb H Sawin, and Martin A Schmidt. Characterization of a time multiplexed inductively coupled plasma etcher. *Journal of the Electrochemical Society*, 146(1):339–349, 1999.

[11] Brian Matthews and Jack W Judy. Design and fabrication of a micromachined planar patch-clamp substrate with integrated microfluidics for single-cell measurements. *Microelectromechanical Systems, Journal of*, 15(1):214–222, 2006.

[12] Nadim Maluf and Kirt Williams. *Introduction to microelectromechanical systems engineering*. Artech House, 2004.

[13] R Dussart, M Boufnichel, G Marcos, P Lefaucheux, A Basillais, R Benoit, T Tillocher, X Mellhaoui, H Estrade-Szwarckopf, and P Ranson. Passivation mechanisms in cryogenic sf_6/o_2 etching process. *Journal of Micromechanics and Microengineering*, 14(2):190, 2004.

[14] Xavier Mellhaoui, Rémi Dussart, Thomas Tillocher, Philippe Lefaucheux, Pierre Ranson, Mohamed Boufnichel, and Lawrence J Overzet. sio_xf_y passivation layer in silicon cryoetching. *Journal of Applied Physics*, 98(10):104901, 2005.

[15] Lauri Sainiemi et al. *Cryogenic deep reactive ion etching of silicon micro and nanostructures*. PhD thesis, Helsinki University of Technology, 2009.

[16] Meint J de Boer, JGE Gardeniers, Henri V Jansen, Edwin Smulders, M-J Gilde, Gerard Roelofs, Jay N Sasserath, and Miko Elwenspoek. Guidelines for etching silicon MEMS structures using fluorine high-density plasmas at cryogenic temperatures. *Microelectromechanical Systems, Journal of*, 11(4):385–401, 2002.

[17] Jeffrey Mabeck and George Malliaras. Chemical and biological sensors based on organic thin-film transistors. *Analytical and Bioanalytical Chemistry*, 384(2):343–353, January 2006. ISSN 1618-2642.

[18] Maria Magliulo, Antonia Mallardi, Mohammad Yusuf Mulla, Serafina Cotrone, Bianca Rita Pistillo, Pietro Favia, Inger Vikholm-Lundin, Gerardo Palazzo, and Luisa Torsi. Electrolyte-gated organic field-effect transistor sensors based on supported biotinylated phospholipid bilayer. *Advanced Materials*, 25(14):2090–2094, 2013.

[19] Mark E Roberts, Stefan CB Mannsfeld, Núria Queraltó, Colin Reese, Jason Locklin, Wolfgang Knoll, and Zhenan Bao. Water-stable organic transistors and their application in chemical and biological sensors. *Proceedings of the National Academy of Sciences*, 105(34):12134–12139, 2008.

[20] Mihai Irimia-Vladu. "green" electronics: biodegradable and biocompatible materials and devices for sustainable future. *Chemical Society Reviews*, 43(2):588–610, 2014.

[21] Huchen Zhou, Laura Baldini, Jason Hong, Andrew J Wilson, and Andrew D Hamilton. Pattern recognition of proteins based on an array of functionalized porphyrins. *Journal of the American Chemical Society*, 128(7):2421–2425, 2006.

[22] Luca Beverina and Patrizio Salice. Squaraine compounds: tailored design and synthesis towards a variety of material science applications. *European journal of organic chemistry*, 2010(7):1207–1225, 2010.

[23] Franco Dinelli, Mauro Murgia, Pablo Levy, Massimiliano Cavallini, Fabio Biscarini, and Dago M de Leeuw. Spatially correlated charge transport in organic thin film transistors. *Physical Review Letters*, 92(11):116802, 2004.

[24] Maren Daraktchiev, Adrian von Mühlenen, Frank Nüesch, Michel Schaer, Martin Brinkmann, Marie-Noëlle Bussac, and Libero Zuppiroli. Ultrathin organic transistors on oxide surfaces. *New Journal of Physics*, 7(1):133, 2005.

[25] P Stallinga and HL Gomes. Thin-film field-effect transistors: The effects of traps on the bias and temperature dependence of field-effect mobility, including the meyer–neldel rule. *Organic Electronics*, 7(6):592–599, 2006.

[26] Peter Stallinga. *Electrical Characterization of Organic Electronic Materials and Devices*. John Wiley and Sons, Ltd, 2009.

[27] Marcus Halik, Hagen Klauk, Ute Zschieschang, Günter Schmid, Wolfgang Radlik, Sergei Ponomarenko, Stephan Kirchmeyer, and Werner Weber. High-mobility organic thin-film transistors based on α, α'-didecyloligothiophenes. *Journal of Applied Physics*, 93(5):2977–2981, 2003.

[28] Andrei Sazonov, Denis Stryahilev, Arokia Nathan, and Lydia D Bogomolova. Dielectric performance of low temperature silicon nitride films in a-si: H tfts. *Journal of non-crystalline solids*, 299:1360–1364, 2002.

[29] C Chaneliere, JL Autran, RAB Devine, and B Balland. Tantalum pentoxide (ta_2o_5) thin films for advanced dielectric applications. *Materials Science and Engineering: R: Reports*, 22(6):269–322, 1998.

[30] Arnaldo D'Amico, Corrado Di Natale, Roberto Paolesse, Antonella Macagnano, and Alessandro Mantini. Metalloporphyrins as basic material for volatile sensitive sensors. *Sensors and Actuators B: Chemical*, 65(1):209–215, 2000.

[31] J.A.J. Brunink, C. Di Natale, F. Bungaro, F.A.M. Davide, A. D'Amico, R. Paolesse, T. Boschi, M. Faccio, and G. Ferri. The application of metalloporphyrins as coating material for quartz microbalance-based chemical sensors. *Analytica Chimica Acta*, 325(1-2):53–64, 1996. cited By (since 1996)89.

[32] Kevin M Smith and John Edwin Falk. *Porphyrins and metalloporphyrins*.

[33] Karl M Kadish, Kevin M Smith, and Roger Guilard. *The porphyrin handbook*. Elsevier, 1999.

[34] C. Di Natale, A. Macagnano, G. Repole, G. Saggio, A. D'Amico, R. Paolesse, and T. Boschi. The exploitation of metalloporphyrins as chemically interactive material in chemical sensors. *Materials Science and Engineering C*, 5(3-4):209–215, 1998.

[35] Alexei Nabok. *Organic and inorganic nanostructures*, volume 8. Artech House Norwood, 2005.

[36] J Hirsch. Hopping transport in disordered aromatic solids: a re-interpretation of mobility measurements on pkv and tnf. *Journal of Physics C: Solid State Physics*, 12(2):321, 1979.

[37] Raymond Bonnett. *Chemical aspects of photodynamic therapy*. CRC Press, 2000.

[38] Tadeusz Marek Krygowski, Michał K Cyrański, and MAR Matos. *Aromaticity in heterocyclic compounds*. Springer, 2008.

[39] Elke Scheer. *Molecular electronics: an introduction to theory and experiment*, volume 1. World Scientific, 2010.

[40] Matthew Jurow, Amanda E Schuckman, James D Batteas, and Charles Michael Drain. Porphyrins as molecular electronic components of functional devices. *Coordination chemistry reviews*, 254(19):2297–2310, 2010.

[41] Chengliang Wang, Huanli Dong, Wenping Hu, Yunqi Liu, and Daoben Zhu. Semiconducting π-conjugated systems in field-effect transistors: a material odyssey of organic electronics. *Chemical reviews*, 112(4):2208–2267, 2011.

[42] Chong-Yang Liu, Horng-Long Pan, Huajun Tang, Marye Anne Fox, and Allen J Bard. Effect of structural order on the dark current and photocurrent in zinc octakis (. beta.-decoxyethyl) porphyrin thin-layer cells. *The Journal of Physical Chemistry*, 99(19):7632–7636, 1995.

[43] Zhenan Bao, Andrew J Lovinger, and Ananth Dodabalapur. Organic field-effect transistors with high mobility based on copper phthalocyanine. *Applied Physics Letters*, 69(20):3066–3068, 1996.

[44] Marta Mas-Torrent and Concepció Rovira. Role of molecular order and solid-state structure in organic field-effect transistors. *Chemical reviews*, 111(8):4833–4856, 2011.

[45] Yi Li, Shuang Chen, Qi Liu, Leyong Wang, Takao Someya, Jing Ma, Xizhang Wang, and Zheng Hu. Deposition-pressure-induced optimization of molecular packing for high-performance organic thin-film transistors based on copper phthalocyanine. *The Journal of Physical Chemistry C*, 116(6):4287–4292, 2012.

[46] Satoshi Hoshino, Toshihide Kamata, and Kiyoshi Yase. Effect of active layer thickness on device properties of organic thin-film transistors based on *cu*(*ii*) phthalocyanine. *Journal of Applied Physics*, 92(10):6028–6032, 2002.

[47] Y-Y Noh, J-J Kim, Yuji Yoshida, and Kiyoshi Yase. Effect of molecular orientation of epitaxially grown platinum (ii) octaethyl porphyrin films on the performance of field-effect transistors. *Advanced Materials*, 15(9):699–702, 2003.

[48] Th B Singh, S Günes, N Marjanović, NS Sariciftci, and R Menon. Correlation between morphology and ambipolar transport in organic field-effect transistors. *Journal of Applied Physics*, 97(11):114508, 2005.

[49] Jana Zaumseil and Henning Sirringhaus. Electron and ambipolar transport in organic field-effect transistors. *Chemical reviews*, 107(4):1296–1323, 2007.

[50] Lukas Bürgi, Mathieu Turbiez, Reto Pfeiffer, Frank Bienewald, Hans-Jörg Kirner, and Carsten Winnewisser. High-mobility ambipolar near-infrared light-emitting polymer field-effect transistors. *Advanced Materials*, 20(11):2217–2224, 2008.

[51] Dietmar Keil, Horst Hartmann, and Torsten Moschny. Synthesis and characterization of 1, 3-bis-(2-dialkylamino-5-thienyl)-substituted squaraines—a novel class of intensively coloured panchromatic dyes. *Dyes and pigments*, 17(1):19–27, 1991.

[52] Sivaramapanicker Sreejith, Priya Carol, Parayalil Chithra, and Ayyappanpillai Ajayaghosh. Squaraine dyes: a mine of molecular materials. *Journal of Materials Chemistry*, 18(3):264–274, 2008.

[53] Jason R Cox, Peter Müller, and Timothy M Swager. Interrupted energy transfer: highly selective detection of cyclic ketones in the vapor phase. *Journal of the American Chemical Society*, 133(33):12910–12913, 2011.

[54] Shino Ohira, Indranil Rudra, Karin Schmidt, Stephen Barlow, Sung-Jae Chung, Qing Zhang, Jon Matichak, Seth R Marder, and Jean-Luc Brédas. Electronic and vibronic contributions to two-photon absorption in donor–acceptor–donor squaraine chromophores. *Chemistry-A European Journal*, 14(35):11082–11091, 2008.

[55] Vadakkancheril S Jisha, Kalliat T Arun, Mahesh Hariharan, and Danaboyina Ramaiah. Site-selective interactions: squaraine dye- serum albumin complexes with enhanced fluorescence and triplet yields. *The Journal of Physical Chemistry B*, 114(17):5912–5919, 2010.

[56] Kock Yee Law. Squaraine chemistry. design, synthesis and xerographic properties of a highly sensitive unsymmetrical fluorinated squaraine. *Chemistry of materials*, 4(3):605–611, 1992.

[57] Fabio Silvestri, Michael D Irwin, Luca Beverina, Antonio Facchetti, Giorgio A Pagani, and Tobin J Marks. Efficient squaraine-based solution processable bulk-heterojunction solar cells. *Journal of the American Chemical Society*, 130(52): 17640–17641, 2008.

[58] Edsger CP Smits, Sepas Setayesh, Thomas D Anthopoulos, Michael Buechel, Wim Nijssen, Reinder Coehoorn, Paul WM Blom, Bert de Boer, and Dago M de Leeuw. Near-infrared light-emitting ambipolar organic field-effect transistors. *Advanced Materials*, 19(5):734–738, 2007.

[59] Chengyi Zhang, Xiujuan Zhang, Xiaohong Zhang, Xuemei Ou, Wenfeng Zhang, Jiansheng Jie, Jack C Chang, Chun-Sing Lee, and Shuit-Tong Lee. Facile one-step fabrication of ordered organic nanowire films. *Advanced Materials*, 21(41): 4172–4175, 2009.

[60] Maddalena Binda, Tiziano Agostinelli, Mario Caironi, Dario Natali, Marco Sampietro, Luca Beverina, Riccardo Ruffo, and Fabio Silvestri. Fast and air stable near-infrared organic detector based on squaraine dyes. *Organic electronics*, 10 (7):1314–1319, 2009.

[61] Marcel Gsänger, Eva Kirchner, Matthias Stolte, Christian Burschka, Vladimir Stepanenko, Jens Pflaum, and Frank Würthner. High-performance organic thin-film transistors of j-stacked squaraine dyes. *Journal of the American Chemical Society*, 136(6):2351–2362, 2014.

[62] AW Coats and JP Redfern. Thermogravimetric analysis. a review. *Analyst*, 88 (1053):906–924, 1963.

[63] Andreas Elschner, Stephan Kirchmeyer, Wilfried Lovenich, Udo Merker, and Knud Reuter. *PEDOT: principles and applications of an intrinsically conductive polymer*. CRC Press, 2010.

[64] F Jonas and L Schrader. Conductive modifications of polymers with polypyrroles and polythiophenes. *Synthetic Metals*, 41(3):831–836, 1991.

[65] Michael Dietrich, Jürgen Heinze, Gerhard Heywang, and Friedrich Jonas. Electrochemical and spectroscopic characterization of polyalkylenedioxythiophenes. *Journal of Electroanalytical Chemistry*, 369(1):87–92, 1994.

[66] Friedrich Jonas, Werner Krafft, and Bavo Muys. Poly (3, 4-ethylenedioxythiophene): Conductive coatings, technical applications and properties. In *Macromolecular Symposia*, volume 100, pages 169–173. Wiley Online Library, 1995.

[67] L Groenendaal, Friedrich Jonas, Dieter Freitag, Harald Pielartzik, and John R Reynolds. Poly (3, 4-ethylenedioxythiophene) and its derivatives: past, present, and future. *Advanced Materials*, 12(7):481–494, 2000.

[68] Jin Lu, Nicholas J Pinto, and Alan G MacDiarmid. Apparent dependence of conductivity of a conducting polymer on an electric field in a field effect transistor configuration. *Journal of Applied Physics*, 92(10):6033–6038, 2002.

[69] AJ Epstein, F-C Hsu, N-R Chiou, and VN Prigodin. Doped conducting polymer-based field effect devices. *Synthetic metals*, 137(1-3):859–861, 2003.

[70] HS Kang, H-S Kang, JK Lee, JW Lee, J Joo, JM Ko, MS Kim, and JY Lee. Humidity-dependent characteristics of thin film poly (3, 4-ethylenedioxythiophene) field-effect transistor. *Synthetic metals*, 155(1):176–179, 2005.

[71] Fang-Chi Hsu, Vladimir N Prigodin, and Arthur J Epstein. Electric-field-controlled conductance of "metallic" polymers in a transistor structure. *Physical Review B*, 74(23):235219, 2006.

[72] Hua Bai and Gaoquan Shi. Gas sensors based on conducting polymers. *Sensors*, 7(3):267–307, 2007.

[73] Alessandro Grattoni, Haifa Shen, Daniel Fine, Arturas Ziemys, Jaskaran S Gill, Lee Hudson, Sharath Hosali, Randy Goodall, Xuewu Liu, and Mauro Ferrari. Nanochannel technology for constant delivery of chemotherapeutics: beyond metronomic administration. *Pharmaceutical research*, 28(2):292–300, 2011.

[74] Stanley S Davis and Lisbeth Illum. Drug delivery systems for challenging molecules. *Int. J. pharm*, 176(1):1–8, 1998.

[75] DD Breimer. Future challenges for drug delivery. *Journal of Controlled Release*, 62(1):3–6, 1999.

[76] Sarah L Tao and Tejal A Desai. Microfabricated drug delivery systems: from particles to pores. *Advanced drug delivery reviews*, 55(3):315–328, 2003.

[77] Guoqing Hu and Dongqing Li. Multiscale phenomena in microfluidics and nanofluidics. *Chemical Engineering Science*, 62(13):3443–3454, 2007.

[78] Christopher Hughes, Li-Hsien Yeh, and Shizhi Qian. Field effect modulation of surface charge property and electroosmotic flow in a nanochannel: Stern layer effect. *The Journal of Physical Chemistry C*, 117(18):9322–9331, 2013.

[79] RA McKee, FJ Walker, and MF Chisholm. Crystalline oxides on silicon: the first five monolayers. *Physical Review Letters*, 81(14):3014, 1998.

[80] Renata Rapuano and Ana Maria Carmona-Ribeiro. Physical adsorption of bilayer membranes on silica. *Journal of Colloid and Interface Science*, 193(1):104–111, 1997.

[81] Adrien Plecis, Reto B Schoch, and Philippe Renaud. Ionic transport phenomena in nanofluidics: experimental and theoretical study of the exclusion-enrichment effect on a chip. *Nano Letters*, 5(6):1147–1155, 2005.

[82] Xiayan Wang, Jianzheng Kang, Shili Wang, Joann J Lu, and Shaorong Liu. Chromatographic separations in a nanocapillary under pressure-driven conditions. *Journal of Chromatography A*, 1200(2):108–113, 2008.

[83] Rohit Karnik, Rong Fan, Min Yue, Deyu Li, Peidong Yang, and Arun Majumdar. Electrostatic control of ions and molecules in nanofluidic transistors. *Nano letters*, 5(5):943–948, 2005.

[84] Tzu-Chi Kuo, Lisa A Sloan, Jonathan V Sweedler, and Paul W Bohn. Manipulating molecular transport through nanoporous membranes by control of electrokinetic flow: effect of surface charge density and Debye length. *Langmuir*, 17(20): 6298–6303, 2001.

[85] Reto B Schoch, Arnaud Bertsch, and Philippe Renaud. ph-controlled diffusion of proteins with different pi values across a nanochannel on a chip. *Nano letters*, 6 (3):543–547, 2006.

[86] W Sparreboom, A Van Den Berg, and JCT Eijkel. Principles and applications of nanofluidic transport. *Nature Nanotechnology*, 4(11):713–720, 2009.

[87] Wen-Hwa Chu, Ruby Chin, Tony Huen, and Mauro Ferrari. Silicon membrane nanofilters from sacrificial oxide removal. *Microelectromechanical Systems, Journal of*, 8(1):34–42, 1999.

[88] Frank Martin, Robbie Walczak, Anthony Boiarski, Michael Cohen, Teri West, Carlo Cosentino, and Mauro Ferrari. Tailoring width of microfabricated nanochannels to solute size can be used to control diffusion kinetics. *Journal of Controlled Release*, 102(1):123–133, 2005.

[89] J Han and HG Craighead. Separation of long dna molecules in a microfabricated entropic trap array. *Science*, 288(5468):1026–1029, 2000.

[90] R Greenwood and K Kendall. Selection of suitable dispersants for aqueous suspensions of zirconia and titania powders using acoustophoresis. *Journal of the European Ceramic Society*, 19(4):479–488, 1999.

[91] *Isoelectric Point Determination.* HORIBA Instruments, Inc., an195 application note edition.

[92] Shoji Yoshida, Nobuyoshi Hara, and Katsuhisa Sugimoto. Development of a wide range pH sensor based on electrolyte-insulator-semiconductor structure with corrosion-resistant al_2o_3 ta_2o_5 and al_2o_3 zro_2 double-oxide thin films. *Journal of The Electrochemical Society*, 151(3):H53–H58, 2004.

[93] G Caserta, B Rispoli, and A Serra. Space-charge-limited current and band structure in amorphous organic films. *Physica Status Solidi (b)*, 35(1):237–248, 1969.

[94] MP Sarachik and P Dai. Variable-range hopping in Si: B: A temperature-independent prefactor in three dimensions. *Physica Status Solidi (b)*, 230(1): 205–209, 2002.

[95] P Stallinga and HL Gomes. Modeling electrical characteristics of thin-film field-effect transistors: I. trap-free materials. *Synthetic metals*, 156(21):1305–1315, 2006.

[96] P Stallinga and HL Gomes. Modeling electrical characteristics of thin-film field-effect transistors: Ii: Effects of traps and impurities. *Synthetic metals*, 156(21): 1316–1326, 2006.

[97] Gilles Horowitz et al. Organic field-effect transistors. *Advanced Materials*, 10(5): 365–377, 1998.

[98] Graciela B Blanchet, CR Fincher, Michael Lefenfeld, and JA Rogers. Contact resistance in organic thin film transistors. *Applied Physics Letters*, 84(2):296–298, 2004.

[99] RA Street and A Salleo. Contact effects in polymer transistors. *Applied Physics Letters*, 81(15):2887–2889, 2002.

[100] Behrang H Hamadani and Douglas Natelson. Extracting contact effects in organic fets. *Proceedings of the IEEE*, 93(7):1306–1311, 2005.

[101] Raoul Schroeder, Leszek A Majewski, and Martin Grell. Improving organic transistor performance with schottky contacts. *Applied physics letters*, 84(6):1004–1006, 2004.

[102] BH Hamadani and D Natelson. Temperature-dependent contact resistances in high-quality polymer field-effect transistors. *Applied Physics Letters*, 84(3):443–445, 2004.

[103] K. Waragai, H. Akimichi, S. Hotta, H. Kano, and H. Sakaki. Charge transport in thin films of semiconducting oligothiophenes. *Phys. Rev. B*, 52:1786–1792, Jul 1995.

[104] SK Aityan and VI Portnov. Computer simulation of single-file transport. *General physiology and biophysics*, 5(4):351–364, 1986.

[105] Louis A. Clark, George T. Ye, and Randall Q. Snurr. Molecular traffic control in a nanoscale system. *Phys. Rev. Lett.*, 84:2893–2896, Mar 2000.

[106] Estéban Saatdjian. *Transport phenomena: equations and numerical solutions.* Wiley & Sons, New York, 2000.

[107] Carlo Cosentino, Francesco Amato, Robbie Walczak, Anthony Boiarski, and Mauro Ferrari. Dynamic model of biomolecular diffusion through two-dimensional nanochannels. *The Journal of Physical Chemistry B*, 109(15):7358–7364, 2005.

[108] Goran Peskir. On the diffusion coefficient: the einstein relation and beyond. 2003.

[109] Francesco Amato, Carlo Cosentino, Sabrina Pricl, Marco Ferrone, Maurizio Fermeglia, Mark Ming-Cheng Cheng, Robert Walczak, and Mauro Ferrari. Multiscale modeling of protein transport in silicon membrane nanochannels. part 2. from molecular parameters to a predictive continuum diffusion model. *Biomedical microdevices*, 8(4):291–298, 2006.